



**Institute of Solid
State Physics**

Institute of Solid State Physics University of Latvia

Doctoral thesis

**Optical depth profile and phase
transitions investigation of NaNbO_3
and $\text{Pb}(\text{Zr},\text{Ti})\text{O}_3$ thin films**

Author: M.Sc.phys. Ilze Aulika

Supervisor: Dr.phys. Vismants Zauls



**University of
Latvia**

Riga, 2008



Cietvielu fizikas
institūts

Cietvielu fizikas institūts Latvijas Universitātē

Promocijas darbs

Optiskā gradienta un fāzu pāreju
pētījumi NaNbO_3 un $\text{Pb}(\text{Zr},\text{Ti})\text{O}_3$
plānās kārtiņās

Darba autore: M.Sc.phys. Ilze Aulika
Darba vadītājs: Dr.phys. Vismants Zauls



Latvijas
Universitāte

Rīga, 2008

Content

Annotation	
Abstract	5
Anotācija	6
1. Introduction	
1.1 Introduction and general description	7
1.2 Aim of the work	10
1.3 Main results	10
2. Overview on the literature	
2.1 Sodium niobate NaNbO_3	12
2.2 Lead zirconate titanate $\text{Pb}(\text{Zr,Ti})\text{O}_3$	17
3. Reflectometry and ellipsometry	
3.1 Introduction	21
3.2 Reflectometry	22
3.3 Ellipsometry	23
3.3.1 Null-ellipsometry	25
3.3.2 Rotating analyzer ellipsometry	27
3.4 General ellipsometry	28
3.4.1 Dielectric constant extraction from ellipsometric parameters	28
3.4.2 Polarization States of Light	28
3.4.3 Muller matrix formalism	28
3.4.4 Jones matrix formalism	32
3.5 Muller matrix theory with imperfections	34
3.5.1 Definition of matrices	34
3.5.2 Intensity on the detector	34
3.5.3 Sample as depolarizer of the light	35
3.6 Dielectric function	37
3.6.1 Oscillator models for the dielectric function	37
3.7 Effective approximation theory for the mixed media	38
3.8 Optical gradient	39
3.9 Thermo-optics	40
4. Experiment and calculation	
4.1 Experiment	43
4.2 Simulation and fitting of spectroscopic ellipsometric data	46
5. Samples	
5.1 Sodium niobate NaNbO_3	49
5.1.1 Pulsed laser deposition	50
5.2 Lead zirconate titanate $\text{Pb}(\text{Zr,Ti})\text{O}_3$	52
5.2.1 Sol-gel technique	53
6. Results	
6.1 Sodium niobate NaNbO_3	55
6.1.1 XRD	55
6.1.2 Dielectrics	55
6.1.3 Raman spectroscopy	56
6.1.4 AFM	57
6.1.5 Optical properties	58
6.1.6 Thermo-optics	62
6.1.7 Discussion	64
6.2 Lead zirconate titanate $\text{Pb}(\text{Zr,Ti})\text{O}_3$	68

6.2.1 XRD	68
6.2.2 Optical properties	69
6.2.3 Discussion	75
7. Summary	80
8. Conclusion	81
Defended thesis	83
List of scientific publications related to this work	84
List of scientific publications not related to this work	86
Scientific seminars and conferences, where work have been discussed	90
The author's education and scientific experience	91
Acknowledgments	93
References	94

Abstract

Ferroelectrics (FE) thin films have attracted much attention due to their potential applications such as high dielectric constant capacitors, non-volatile memories, infrared sensors and electro-optic devices. Their ferroelectric and dielectric properties have been extensively investigated, while their optical properties have been relatively rarely studied. However, the optical constant, e.g., refractive index and extinction coefficient has great importance for wave guiding and other optical applications. In this report optical reflectometry and ellipsometry techniques will be shown as efficient non-destructive tools for measuring thickness, complex refractive index, interface between bottom electrode and the film, surface roughness, and optical gradient of transparent ferroelectric thin films. Ellipsometry will be shown as an effective tool for the thermo-optical investigations of thin films, too.

The optical properties, depth profile of refractive index, temperature dependence of refractive index and optical band gap energy of sodium niobate NaNbO_3 (NN) thin films made by pulsed laser deposition (PLD) were investigated. Thin films were deposited on various substrates: silicon/strontium ruthenium Si/SrRuO_3 , and silicon/silicon dioxide/titanium/platinum/strontium ruthenium $\text{Si/SiO}_2/\text{Ti/Pt/SrRuO}_3$.

The thickness dependency of optical properties, interface, band gap, surface roughness, and depth profile of refractive index were evaluated for sol-gel lead zirconate titanate $\text{PbZr}_x\text{Ti}_{1-x}\text{O}_3$ ($x = 30, 52, 95\%$) thin and thick films. These films were made using two solvents – AcOH/MeOH and 2-MEO. The layers were crystallized in two different ways – annealing all together or individually. Thin films were grown on $\text{Si/SiO}_2/\text{Ti/Pt}$ substrates. Due to the broad technical applications of sol-gel PZT thin films, the understanding of the chemical composition and physical properties resulting from different processing methods is crucial. The knowledge of the optical gradient within the film, as well as the interface change within the film thickness allows identification and further optimization of the thin film performance.

The increase of refractive index of NN with increase of the thickness was evaluated. The five phase transition temperatures were observed in NN thin films for the first time. The optical gradient investigations of PZT thin films showed that solvents are not responsible for the gradient appearance; the contribution comes from the crystallization process. The linear decrease of n and linear increase of E_g with increase of the Zr/Ti ratio in PZT thin films were detected.

The ellipsometric measurements were performed with variable-angle null-ellipsometer “JTM - 3M” (at He-Ne laser wavelength $\lambda = 632.8$ nm, angles set from 45° to 75°). A miniature “Ocean Optics” CCD spectrometer, model PC 1000, designed as a plug-in PC ISA slot with fiber optics input was used for the reflectivity measurements under normal light incidence geometry in the spectral range of (350 – 750) nm to estimate approximate thin film thickness and optical properties. To evaluate precise optical properties at the wider wavelength range (230 – 1200 nm) and temperature dependence (5 – 850 K), the Woollam spectroscopic ellipsometer was used. Additionally x-ray, Raman spectroscopy, dielectric and atomic force microscope (AFM) studies were done on ferroelectric thin films.

The optimal values for the refractive index n , extinction coefficient k , film thickness d , interface thickness, thickness non-uniformity, optical gradient, and temperature dependence of optical band gap E_g and refractive index were found by the mean square procedure for all model minimization, using the software packages ThinFilmWizard and WVASE32.

Anotācija

Segnetoelektriķu plānās kārtiņas piesaista aizvien lielāku uzmanību sakarā ar plašo pielietojamību kā augstas dielektriskās konstantes kondensatori, atmiņas iekārtas elektronikā, infrasarkanā starojuma sensori, nelineārās un integrālās optikas ierīces. Šinī darbā optiskās reflektometrijas un elipsometrijas metodes tiek parādītas kā efektīvas bezkontakta metodes kompleksā laušanas koeficienta, kārtiņas biezuma, pārejas slāņa no apakšējā elektroda uz kārtiņu, virsmas negluduma, optiskā gradienta noteikšanai caurspīdīgām segnetoelektriskām plānām kārtiņām. Elipsometrija tiks demonstrēta arī kā efektīva metode termooptisko pētījumu veikšanai plānām kārtiņām.

Optiskās īpašības, optiskais gradients, laušanas koeficienta un aizliegtās zonas platuma temperatūras atkarības tika pētītas nātrija niobāta NaNbO_3 (NN) plānām kārtiņām, kas iegūtas ar lāzera ablācijas metodi uz dažādām pamatnēm – silīcija/stroncija rutēnija Si/SrRuO_3 , un silīcija/silīcija dioksīda/titāna/platīna/stroncija rutēnija $\text{Si/SiO}_2/\text{Ti}/\text{Pt}/\text{SrRuO}_3$.

Optisko īpašību, pārejas slāņa, aizliegtās zonas platuma, virsmas negluduma un optiskā gradienta pētījumi tika veikti sol-gela svina cirkonāta titanāta $\text{PbZr}_x\text{Ti}_{1-x}\text{O}_3$ ($x = 30, 52, 95\%$) plānās un biežās kārtiņās. Kārtiņas tika iegūtas, izmantojot divus dažādus ķīmiskos šķīdinātājus - AcOH/MeOH un 2-MEO. Kārtiņu slāņi tika kristalizēti divos veidos – visi slāņi kopā vai katrs slānītis atsevišķi. Kārtiņas tika uzklātas uz $\text{Si/SiO}_2/\text{Ti}/\text{Pt}$ substrātiem. Sakarā ar ļoti plašajiem PZT kārtiņu tehniskajiem pielikumiem, sapratne par to, kā dažādas kārtiņu iegūšanas metodes ietekmē ķīmisko sastāvu un fizikālas īpašības, ir ārkārtīgi svarīga. Zināšanas par optisko gradientu kārtiņās, kā arī pārejas slāņa izmaiņas ar kārtiņas biezumu ļauj identificēt un turpmāk uzlabot plāno kārtiņu iegūšanas metodes un praktisko pielietojumu.

Tika konstatēta NN kārtiņu laušanas koeficienta palielināšanās, palielinoties kārtiņas biezumam. Pirmo reizi tika novērotas piecas fāzu pārejas NN plānām kārtiņām, izmantojot spektrālo elipsometru. PZT kārtiņu optiskā gradienta pētījumi parādīja, ka gradienta veidošanās nosaka nevis ķīmiskais šķīdinātājs, bet gan kristalizēšanas process. Konstatēts, ka palielinoties Zr/Ti attiecībai, laušanas koeficients lineāri samazinās, bet E_g lineāri palielinās.

Elipsometrijas eksperimentos tika izmantots elipsometrs “JTEM - 3M” ar He – Ne (632.8 nm) lāzeru, ar kuru var veikt mērījumus dažādiem krišanas leņķiem ($45^\circ - 85^\circ$). Reflektometrijas mērījumi tika veikti redzamās gaismas spektra daļā (350 - 750) nm ar “Ocean Optics” PC 1000 tipa miniatūrs CCD spektrometrs PC ISA interfeisa kartes izpildījumā ar optiskās šķiedras ievadu. Šie mērījumi tika veikti, lai ātri novērtētu kārtiņas biezumu un aptuvenās optiskās konstantes. Lai precīzi novērtētu optiskās konstantes plašā spektra diapazonā no 230 – 1200 nm un to temperatūras atkarību (5 – 850 K), tika izmantots Woollam spektrālais elipsometrs. Papildus kārtiņu pētījumiem tika izmantots rentgenstaru difrakcijas analīze, dielektriskā spektroskopija, Ramana spektroskopija un atomspēka mikroskops (AFM).

Laušanas koeficienta n , ekstinkcijas koeficienta k , kārtiņu biezuma d , pārejas slāņa biezuma, biezuma nevienmērības, optiskā gradienta optimālo vērtību noteikšanai, kā arī laušanas koeficienta un aizliegtās zonas temperatūras atkarības tika meklētas ar vidējo kvadrātisko procedūru visu modeļu minimizācijai, izmantojot licenzētas datorprogrammas ThinFilmWizard un WVASE32.

1. Introduction

1.1 Introduction and general description

Ferroelectric oxide materials have offered a huge potential for applications since the discovery of ferroelectric perovskites more than 50 years ago. Their switchable electric polarization is very useful for many applications. One example of these applications is memory storage devices. The domain walls separating different variants are of thickness 1 nm, far thinner than in most ferromagnets. This gives an areal device density approaching 100 Tb/cm², a million times higher than in today's dynamic random access memory devices. There are a lot more of ferroelectrics nanoscale applications, but progress has long been hampered by difficulties in materials processing. Recent breakthroughs in the synthesis and crystal growth of complex oxides have brought the field to an entirely new level. Using advanced thin film vapor deposition techniques, such as molecular beam epitaxy (MBE), pulsed laser deposition (PLD), sputtering, and chemical vapor deposition (CVD), the necessary high-quality ferroelectric films can now be grown for new device capabilities.

In the last few years environmentally friendlier lead free materials became a subject of rising interest. There is a great need to develop lead-free materials with excellent piezoelectric properties. Attention is mainly focused on a sodium niobate containing solid solutions, which are promising lead-free piezoelectric material [1].

Sodium niobate NaNbO₃ (NN), currently used for ultrasonic applications, is one of the promising lead-free piezoelectric materials, for potential application in surface acoustic wave, optical wave guiding, and frequency doubling devices [1 - 4], working at the extreme conditions such as high temperatures. NN has notable piezoelectricity [1], large electro-optic coefficient, high-temperature ferroelectricity, moderate dielectric constant and excellent photorefractive properties.

Recently, the use of ferroelectric thin films of PbZr_xTi_{1-x}O₃ (PZT) family of functional materials in microsystems technology has drawn remarkable interest [5]. PZT provide directly an electro-mechanical coupling and are useful for memory, piezoelectric and pyroelectric devices [6]. PZT thin films have advantage over bulk materials: they can be directly deposited on platinised silicon to allow direct integration with electronics. There are many techniques, for example, pulsed laser deposition (PLD) and chemical vapor deposition (CVD) and others, which allows grow of PZT thin films, but very popular method is sol-gel, what offers low-capital costs, large-scale coating capability and the potential for good control of chemical composition and homogeneity.

Ferroelectricity of perovskite oxide thin films, especially PZT thin films, can be exploited in semiconductor devices to achieve non-volatile random access memory (NVRAM) with long endurance and high-speed access, which can overcome the barriers, encountered in current semiconductor memory technologies. In fact, low density embedded ferroelectric memories are being considered for implementation in commercial devices, such as cellular phones and smart cards. The ferroelectricity can be also applied to voltage dependent and thermally sensitive resistors, and humidity and gas sensors.

There are two possible approaches for fabricating ferroelectric memory devices. The first is the ferroelectric RAM (FeRAM), which is intended for applications where dynamic random access memory (DRAM) is used. In this approach each memory cell consists of a ferroelectric capacitor and a transistor (1T/1C structure). The second approach is the one transistor, ferroelectric field effect transistor (FeFET), which is essentially a conventional FET with a gate dielectric replaced by a thin ferroelectric layer

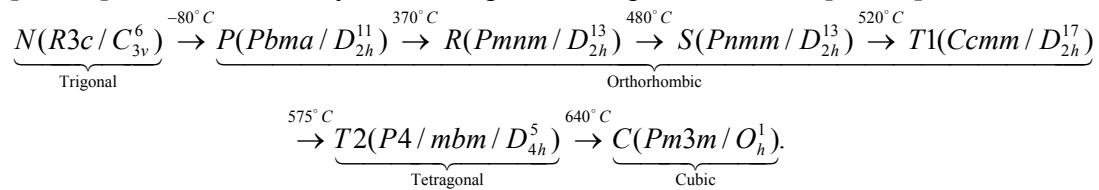
that takes the place of the ferroelectric capacitor. In the latter device the channel conductance is regulated by the polarization state of the ferroelectric that does not require switching of the polarization in order to read the memory cell. This feature is called non-destructive readout.

The very important problem of ferroelectric in microelectronics is the growth temperatures, what exceeds the limits for stability of silicon and underlying barriers. Therefore intense inter-diffusion and oxidation of the silicon wafer occur, resulting in poor transistor performance. PZT is more promising material from this point of view, because high quality PZT layers can be grown by most methods at temperatures of 500–600°C, which makes possible its integration into silicon technology aimed at FeRAMs. In addition, PZT exhibits superior ferroelectric properties such as higher dielectric constants, lower coercive field, and higher Curie temperature as compared to other ferroelectrics. However, PZT suffers from the fatigue problem which proved to be intractable, at least up to now, due to low crystalline quality. Typically, Pt/PZT/PT capacitors lose more than 50% of their polarization within 10^9 – 10^{10} cycles which is not acceptable for IC technology while a fatigue lifetime more than 10^{14} cycles is considered acceptable for commercial applications.

Due to the broad technical applications of sol-gel PZT thin films, for example, actuated micro-mirror for fine-tracking mechanism of high-density optical data storage [7], various sensors, nonvolatile and dynamic random access memories, tunable capacitors for high-frequency microwave applications, electro-optic modulators, applications in optical devices, for instance, rugate filters [8], anti-reflection coatings [9], infrared detectors, and microelectromechanical systems, the understanding of the chemical composition and physical properties resulting from different processing methods is crucial. The variation of chemical composition mirrors in the variation of physical properties such as optical of the film. Thus, the knowledge of the optical gradient within the film, as well as the interface change within the film thickness allows identification and further optimization of the thin film performance.

There are several physical intrigues on these materials:

1. NN has high complexity due to the presence of six phase transitions (PT) in the temperature range of -80 to +650°C changing its phase from high-temperature paraelectric (PE) to antiferrodistortive and then antiferroelectric (AFE) phase at 638 K [10, 11]. The PT with vary in the temperature is presented here [12, 13]



The unit cells of phases *R* and *S* are the largest reported for a low-symmetry phase of any perovskite. There are several reports [9 - 16], where additional PT between *R* and *T1* were found on NN single crystals: Lefkowitz (x-ray, 1966) established unusual PT at 430 - 440°C (detected also by optical observation), 518°C and 526°C; Denoyer (differential thermal analysis (DTA) and x-ray, 1971) – at 523°C; and Glazer (DTA, 1973) – at 530°C while heating and at 512°C while cooling. PT investigations in NN thin films were done just in narrow temperature region, detecting one PT at ~ 370°C [84] at the temperature dependence of dielectric permittivity. Other PT analysis within the broader temperature range from liquid helium till, for example, ~ 550°C of NN thin films were not done, and it is not known, how the reduction of the geometrical sizes of the NN till the thin film of a just 100 – 200 nm small thickness can influence the PT temperatures.

2. The structure and properties of thin film are well known to exhibit a number of deviations from those of bulk ceramics and single crystals. The optical, structural, and electrical properties of ferroelectric film have been found to depend substantially on the preparation method, composition [17], film thickness [18], grain size, and annealing [19]. The origin of the size-dependent ferroelectric properties remains a challenging problem, and a better understanding as to which extent the bulk physical properties can be used for design of thin-layer devices, is actually required. The studies of optical properties of NN thin films, such as refractive index, extinction coefficient thickness and temperature dependence, can give essential information about NN thin film structure, PT and properties, which are practically not know, and possible application in devices. Of the knowledge of the author, there are no reports on optical properties of NN thin films (only some double refraction results on NN single crystals), which give an open field of investigations.

3. Due to the growing interest in graded refractive index films for applications in optical devices, for instance, rugate filters [8], anti-reflection coatings [9], it is important to study optical properties depth profile of thin films. A challenging aspect accordingly to the NN and PZT thin film studies, and, of course, not only these thin films, lies in the development of an appropriate characterization method of the optical gradient. And not only optical gradient is the challenge; the challenge is already to detect optical properties, optical band gap, film thickness, and interface with the high precision due to the difficulties to study so small volume samples. There is report on detected concentration gradient of the chemical element of the sol-gel PZT thin films studied by high resolution transmission electron microscopy (TEM) [20], but it not clears from these studies what causes this inhomogeneity, for example, sol-gel chemical solvent or crystallization process. However, the sample preparation for TEM investigations is tedious and time consuming. Investigations using other methods such as Rutherford back-scattering (RBS) result in the sample modification or even destruction during the analysis. As a non-destructive technique, spectroscopic ellipsometry (SE) has long been recognized as a powerful and very precise method for the characterization of the thin films and its inhomogeneity. SE was already applied to the refractive index depth profile studies of the oxynitride SiO_2N_x films [21 - 24] (additionally the efficiency and precision of the SE was confirmed by chemical etching [24]), lead silicate glass [25], oxidized copper layers [26], polymers [27], semiconductor films of indium tin oxide (ITO) [28, 29], and RF-sputtered self-polarized PZT thin films, approved by discharge optical emission spectroscopy (GD-OES) and pyroelectric profile measurements by the laser intensity-modulation method (LIMM) [30, 31]. SE was also applied to the determination of an ion implantation depth profile of silicon wafers and confirmed by the RBS [32, 33]. Sensitivity of the SE was shown to graded oxygen compositions in $\text{YBa}_2\text{Cu}_3\text{O}_{7-\delta}$ (YBCO) thin films detecting changes in the oxygen concentration to within one unit cell [34].

In this work SE is applied to investigate the PT, optical properties, thickness of the film, interface, optical gradient of the NN and PZT thin films in the wide spectral and temperature range, what allows to detect important information not only from the sample preparation (technical and application) point of view, how deposition technique influence the properties of the films, but also from the physical aspects, involved in this process, what is important in the SE thin films studies.

Investigation of optical properties of perovskite oxides provides important information of not only scientific but also technological nature. In this work ellipsometry and some Raman spectroscopy investigations performed on NN and PZT thin films are presented. Spectroscopic ellipsometry provides dielectric function spectra from near IR to deep UV, and thereby gives information on electronic and phonon band structure. Raman

spectroscopy provides phonon spectra, which give information on crystal structures and soft phonon modes.

1.2 Aim of the work

One of the aims of this thesis is to establish optical properties, depth profile and phase transitions of NN thin films and compare these results with data available for NN bulk materials. NN thin films were deposited on Si/SiO₂/Ti/Pt/SrRuO₃ (Pt/SRO) and Si/SrRuO₃ (Si/SRO) substrates, using PLD technique.

The optical depth profile analyses by SE of sol-gel PZT thin films made by most popular two different solvents (AcOH/MeOH un 2-MEO) and crystallization processes (all layers crystallized together it individually) are second aim of this thesis. The goal of this work is to investigate whether sol-gel PZT thin films have refractive index change into the depth and, if they have, then what is the inhomogeneity possible generator – chemical route or crystallization process.

As the third aim of this thesis, is to estimate refractive index, extinction coefficient, optical band gap, thickness of the interface between bottom electrode and the film, and roughness for PZT thin films with different thicknesses.

And finally the tendency of the refractive index and optical band gap change with the Zr/Ti ratio of the sol-gel PZT thin films will be established, by studying not only PZT 52/48, but also PZT 30/70 and PZT 95/05.

Due to the broad technical applications of sol-gel PZT, and possible applications of NN thin films, the understanding of the chemical composition and physical properties resulting from different processing methods is crucial. Some of the possible reasons what causes variation of the physical properties (such as optical properties) within thickness is the variation of chemical composition with film thickness, or variation of the structure due to the stresses in the film. Thus, the knowledge of the optical gradient within the film allows identification and further optimization of the thin film performance.

Additionally the EDX, AFM, dielectric and Raman spectroscopy, reflectometry and null-ellipsometry experiments were provided on thin films. The author of this work acquired experience on null-ellipsometry and reflectometry during development of the bachelor's work [38b] and master's work [38c]. The basic idea and main results are presented in [38d].

1.3 Main results

The new ellipsometric results are reported here, where temperature dependence of refractive index and optical band gap were measured at the wide temperature (5 – 820 K) to study the phase transitions of NN thin films [35, 36]. The specific anomalies of the refractive index and optical bang gap were detecting by the ellipsometry at the several temperatures. Additionally the Raman spectroscopy [37] measurements are also presented. Depth profile of the real part of refractive index was established [38] for the NN thin films. Increase of refractive index with increase of the film thickness was found.

The spectroscopic ellipsometry studies of sol-gel PZT thin films showed that refractive index increases and band gap energy decrease with decrease of Zr/Ti ratio. Higher values of refractive index and lower values of extinction coefficient were established for the PZT films made by AcOH/MeOH solvent. The thick film samples made by AsOH/MeOH sol and with layers annealed together had no change of the complex refractive index, bad gap energy and thickness of the interface with the film

thickness; the higher value of the thickness and crystallizing all layers together contribute of the homogenous film forming.

Depth profile of the refractive index was established for PZT 52/48 thin films with layers crystallized individually irrespective to the chemical solvent, PZT 52/48 and PZT 30/70 with layers annealed individually at the different temperatures, and composition graded PZT thin film, where first two layers are PZT 30/70, then PZT 52/48 and the last two are PZT 95/05 [38a].

XRD pattern showed that PZT 52/48 films with LCI have additional phases of (100) and (111): the orientation relates to a greater extent to the processing method than to the sol composition. SE investigations also evaluated that the chemical synthesis routes are not responsible for the gradient appearance: it appears from the crystallization process.

2. Overview on the literature

2.1 Sodium niobate NaNbO_3

NaNbO_3 (NN) is a member of the perovskite family (Fig. 2.1) of the alkali niobates with the general form ANbO_3 (A : alkali metal). NN was widely studied in the form of the single crystals, powders and ceramics within the last 55 years. In the middle of the last century investigation were mainly focused on the structural investigation of the NN single crystals. There are large amount of reports on x-ray [12-16, 40-47], dielectrics [40, 48-50], and some results on optics [42, 47, 51, 52 (birefringence)], differential thermal analysis and heat capacity [53-55], and later reports about an infrared reflectivity spectroscopy [56], electron paramagnetic resonance [54], the influence of reduction in valency of Nb ions on the antiferroelectric phase transition in NN [57], x-ray photoelectron spectroscopy [58], inelastic neutron scattering [59, 60] on NN single crystals. In the mean time the field-induced ferroelectric phase of sodium niobate was established [26].

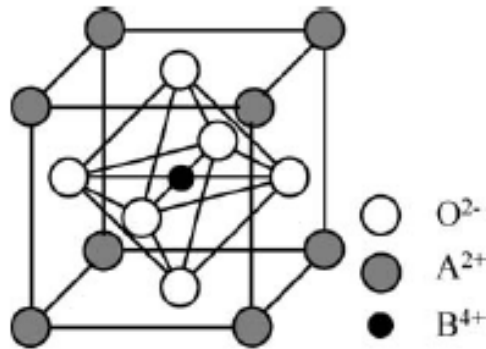


Fig. 2.1. ABO_3 cubic perovskite structure [39].

After intense investigations of the single crystals approximately till the end of 80's the interests on NN vanished. Just in the end of 90's, and especially in the beginning of 2000's due to European LEAF Project [61] within the GROWTH program, the overall objective of what was to try to find alternatives or replacements for the conventional lead-based materials and several lead-free and "low-lead" systems [61-64]. In this project, alkali niobates were proposed as alternative piezoceramic materials, rather than compositions based on heavy metals. Several ferroelectric perovskites of this family were discovered in the 50's and 60's [8], but research on alkali niobates in ceramic form has not been intensive since the 70's. Papers on the powder synthesis [65-69], the neutron diffraction [70] and Raman spectroscopy [71-73] on powders of NN were published. The new methods were established to make NN ceramics [66, 74, 75]; and some new results on dielectric properties, x-ray [40, 76-78], and Raman spectroscopy [79] were reported. The great focus was especially on $(\text{Li},\text{Na})\text{NbO}_3$ (LNN) and $(\text{K},\text{Na})\text{NbO}_3$ (KNN) alkali niobates [80, 81]. In comparison with PZT [82], which has been studied intensively for many years and optimized both in terms of processing and dopants, the KNN system is rather complicated, as Fig. 2.2 shows. It can be seen that with decrease of K concentration the phase diagram becomes extremely complicated. The pure NaNbO_3 exhibits series of the phase transitions [12] (Tab. 2.1).

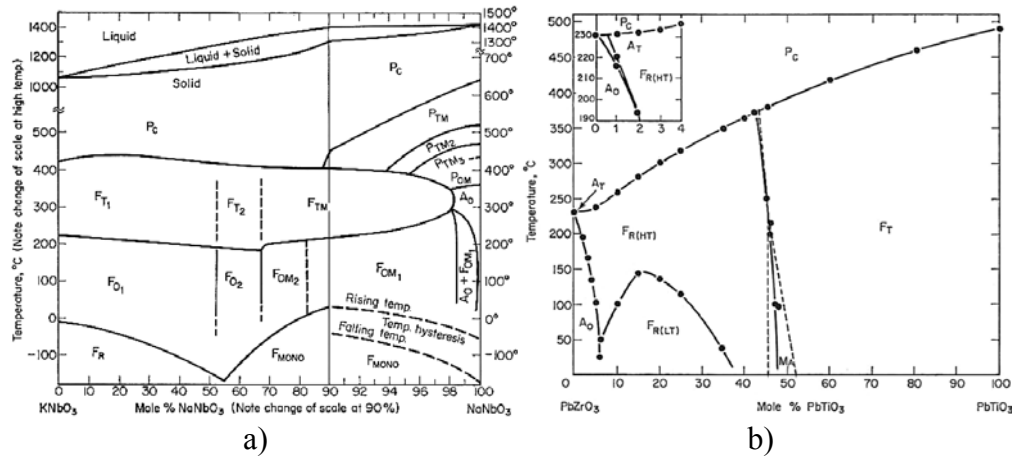


Fig. 2.2. Phase diagram for KNN, the system $\text{KNbO}_3\text{--KNaO}_3$ [80] (a). This system shows a relatively high degree of complexity, e.g. in comparison with the well-known PZT system [80, 82] (b). The area within the dashed lines at the morphotropic phase boundary is the monoclinic phase discovered recently.

C.N.W. Darlington and K.S. Knight found that the diffraction pattern at the room temperature can be indexed successfully using the pseudocubic cell [12]

$$a_{pc} = 2 \times 3.92011, b_{pc} = 2 \times 3.91602,$$

$$c_{pc} = 4 \times 3.87953, a = b = 90^\circ, c = 90.64^\circ$$

as well as the equivalent, rhombic, monoclinic cell is

$$a = 5.5101, b = 5.5717, c = 15.5181,$$

$$a = b = 90^\circ, c = 89.94^\circ$$

The multiplicities, pseudocubic angles and symmetries of the phases of sodium niobate from [12] are presented in Table 2.1. For completeness, phase N, which is stable at low temperatures [12], has been added to the list. The unit cells of phases R and S are the largest reported for a low-symmetry phase of any perovskite. Fig. 2.3 shows the plot of pseudocubic subcell parameters a_{pc} , b_{pc} and c_{pc} versus temperature [16]. The smooth curves were drawn from least-squares fitting of the data to polynomials of degree 1, 2 or 3.

Tab. 2.1. The phases of sodium niobate [12].

Temp ($^\circ\text{C}$)	Phase	Symmetry	Pseudocubic subcells & angles	Multiplicity
– 80	N	Rhombohedral	$a' = b' = c' \alpha = \beta = \gamma < 90^\circ$	$2 \times 2 \times 2$
	P	Monoclinic	$a' \neq b' > c' \alpha = \beta = 90^\circ, \gamma < 90^\circ$	$2 \times 2 \times 4$
370	R	Orthorhombic	$a' \neq b' \neq c' \alpha = \beta = \gamma = 90^\circ$	$2 \times 4 \times 6$
480	S	Orthorhombic	$a' \sim b' \sim c' \alpha = \beta = \gamma = 90^\circ$	$2 \times 4 \times 6$
520	T_1	Orthorhombic	$a' < b' < c' \alpha = \beta = \gamma = 90^\circ$	$2 \times 2 \times 2$
575	T_2	Tetragonal	$a' = b' < c' \alpha = \beta = \gamma = 90^\circ$	$2 \times 2 \times 1$
640	U	Cubic	$a = b = c \alpha = \beta = \gamma = 90^\circ$	$1 \times 1 \times 1$

The cell contains 48 formula units (Fig. 2.4, taken from [46]), and hence the symmetry per formula unit is low. For example, the number of crystallographically distinct sodium atoms is probably 12. Why both these structures should require such a large number of degrees of freedom is unclear and poses an intriguing problem.

If we look what were done on NN thin films, then we can find only some papers: dielectric, x-ray and STM investigation of NN thick films on glass [83], NN thin films on STO/SRO substrate [84], and on Si substrate [67]. There are no reports

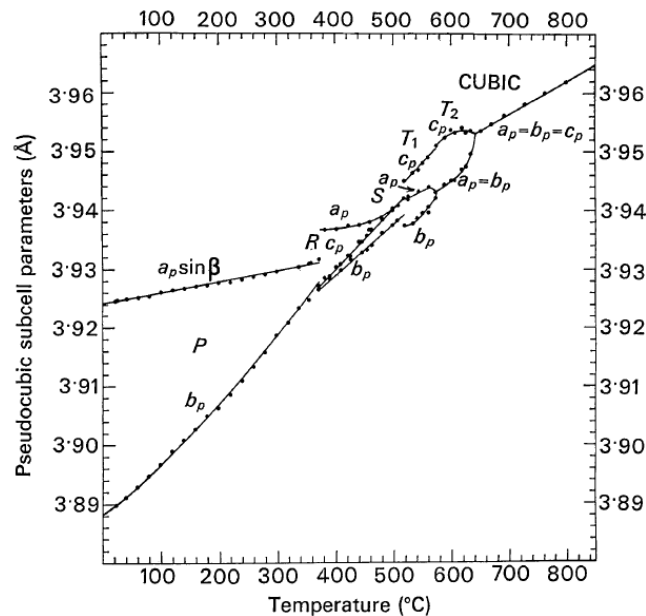


Fig. 2.3. Plot of lattice parameters as a function of temperature, pseudocubic subcell edge lengths [16].

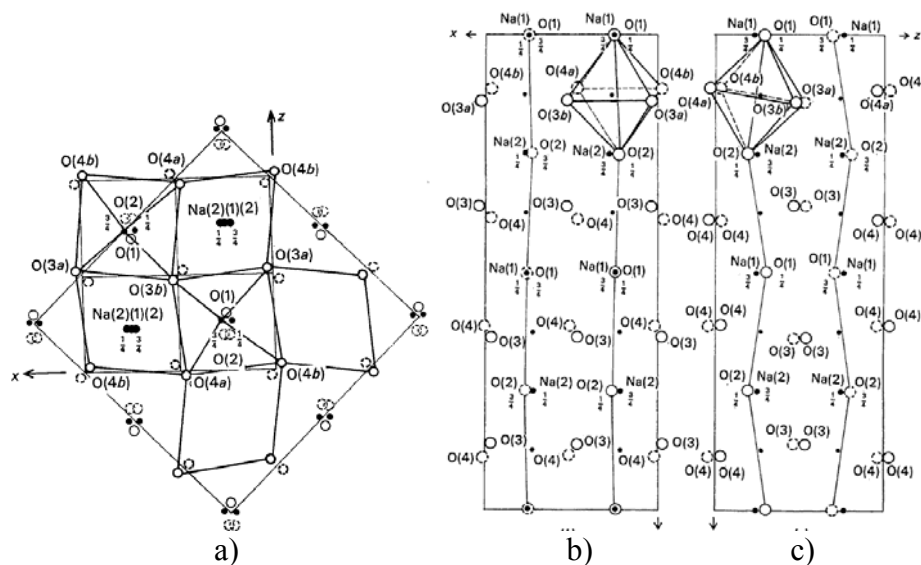


Fig. 2.4. Projection of structure on three principal planes. Small black circles Nb, larger black circles Na, open circles (full or dashed lines) O. a) Heavy full circles are O(3) and O(4), superposed pairs, at heights near $1/8$, $3/8$; heavy dashed circles similar pairs near $5/8$, $7/8$. Light full circles are O(1) at heights 0 and $1/2$, light dashed circles O(2) at either $1/4$ or $3/4$. Atoms marked as Na(1) are superposed pairs at heights 0 and $1/2$. Full lines joining Nb-O and O-O lie near $1/8$ and $3/8$; Nb atoms not so joined lie near $5/8$ and $7/8$. Base of primitive cell outlined (together with lines at $x = 1/2$ and $z = 1/2$) and orthorhombic x , z , axial directions marked (y axis upward). Larger square at 45° is base of B-centered pseudocubic cell; b) and c) Oxygen at heights 0, $1/4$, $1/2$, $3/4$ are shown respectively by heavy dashed circles, thin full circles, heavy full circles, thin dashed circles. One octahedron is outlined in each diagram, and lines joining apical oxygen atoms are shown for all octahedra. Areas outlined represent projection of one unit cell [46].

on optical studies of NN thin films, as the phase transition studies in the wide temperature range, where all six phase transitions of NN can be detected. This field according to the NN thin phase transitions, optical properties and optical gradient is open for discussion.

Physical properties investigation versus temperature, pressure, electric and magnetic fields causing phase transition such as structural and order-disorder was always under intense investigations since the middle of the last century till our days. Some of the most popular techniques for such studies are lattice shift detection by x-rays, latent heat capacity measurements, lattice vibration investigation by Raman spectroscopy, and neutron scattering. In this work we a novel way to detect phase transitions in the solids applying spectroscopic Ellipsometry is presented.

Studies of the temperature dependence of the refractive indices $n(T)$ and another optical parameters are the subject of permanent interest. Such investigations provide valuable information about physical phenomena in solids, in particular, about structural phase transitions (PT), processes in precursor region of ferroelectric PT's, order parameters fluctuations, refraction indexes anomalies. These specific anomalies of the optical properties can be detected also at the interface and surface of the material in case of thin films and single crystals, what is one of the unique possibility and advantage of ellipsometry in respect to other methods. Another advantage of this method is operativeness. The evidence of PT can be seen already in the temperature dependence of main ellipsometric angles.

Ellipsometry gives an opportunity to make in situ dynamic measurements during the modification process of a sample (the growth of a thin film, etching or cleaning of a sample). By in situ ellipsometry measurements it is possible to determine fundamental process parameters, such as, growth or etch rates, variation of optical properties with time and temperature [85], for example.

Temperature dependence of refractive index influenced by the structural PT has been studied since 70's and 80's of the last century. In the beginning an interest was focused on an amorphous semiconductors (Si, Ge, GaAs, GaP, As₂S₂, Te, and Se) [86 - 89], glasses (also disordered glasses SiO_x systems, where $0 \leq x \leq 2$, [90]), and complex glass systems (such as Pb, Ca, Ge and Ba glasses) [90 - 92] due to its possible applications as switching elements and optical communication systems, and insulator materials in the intergraded circuits. The linear increase of the refractive index at the high temperature $n(T)$ was usually expected, owing to elasto-optical and thermo-optic contributions to the optical polarizability. But these conditions have validity only at the regions far from the PT. Hofmann et al. [93] reported drastic deviation from the linear behavior of $n(T)$ in BaTiO₃ on approaching the cubic-tetragonal PT, explaining it with the precursor polarization in the paraelectric state. Similar deviations from linear behavior of $n(T)$ at the PT showed also Dejneka *et al.* [30, 31]. It was shown that $n(T)$ is sensitive to the order parameter of PT in transparent crystals [93, 94]. Afterwards the systematic studies of this phenomena in perovskite type ferroelectrics followed by Burns and Dacol on BaTiO₃ [95] and by Kleemann on KNbO₃, and SrTiO₃ [96]. But unfortunately the clear theory describing thermo-optical effects in FE at PT are still not established due to the complex process involved from the internal contribution of the expansion of the marital, change of the geometrical form, elasto-optical contribution, and electron-phonon interaction. The one of the problems is also to understanding the sine of the thermo-optical coefficients, which differs for different material and the experimental evaluation of this phenomena is determinant.

Thermo-optical studies in these earlier works were performed by the interferometry and linear birefringence, what is very sensitive experimental method but at the same time convened essential restrictions determined by the technique itself. The conventional

optical interferometers generally use precise custom-made bulky optics, which is expensive. These interferometers also suffer from disadvantages of systematic error due to the aberration of the lenses and surface imperfection of the mirrors in the interferometer. Generally two-beam interferometers have disadvantage of instability, which comes from vibration and atmospheric disturbances when the interfering beams have different paths in the interferometer.

Relatively not long time ago the development of spectroscopic ellipsometry enabled to investigate the complex refractive index of thin films and bulks in the wide spectral range (gives access to fundamental physical parameters; morphology, crystal quality, chemical composition, or electrical conductivity), eliminating such disadvantages of other non-destructive and contactless optical technique as dependence on the intensity of the light source (reflectometry), vibration and atmospheric disturbances (interferometry) [85].

Typical ellipsometer can accurately measure ψ and Δ to better than 0.02° and 0.1° respectively. Due to such high accuracy the change of refractive index of $10^{-3} - 10^{-4}$, and film thickness changes down to the sub-Å scale can easily be resolved with this technique [85]. A reflectometer system can not accurately measure intensity values to better than 0.1%, and therefore a reflectivity measurement is not sensitive enough to a small changes of the material optical properties and in the thin film thicknesses.

With spectral ellipsometry one can establish dispersion of the complex dielectric constant of the bulk materials and thin films with very high accuracy. This technique do not require a large size of the sample; it is enough to have a size $\sim 5 \times 5$ mm. In situ spectral ellipsometry studies allows to detect surface PT, as well as of the interface what is very important for thin film and crystal studies [85].

At the structural phase transition of the solid, series of the physical “chain reactions” occurs: due to the expansion of the material, atoms are shifting, changing its positions (changes in the crystallographic symmetry), as the result there are adjustment of the distribution of the wave function of the system due to the change of the periodic potential of the crystal lattice and obviously changes in the band structure of the solid, which cause afterwards changes in the wide range of the physical properties of this material, such as electrical and optical. By spectral ellipsometer dispersion of the complex dielectric (or refractive index) function of the materials can be established. Such materials like dielectrics, ferroelectrics, and semiconductors have the fundamental absorption edge at the near ultraviolet and visible spectral range. Analyzing such materials with the ellipsometer gives an opportunity to study band gap and band structure of the solids. An investigation of the temperature dynamics of the refractive index, absorption coefficient, also thickness of films, and the band gap energy gives an advantage to study phase transitions of the bulks and thin films. Optical properties and optical band gap energy can be carefully and very effective studied with spectral thermo-ellipsometer due to its high accuracy and sensitivity, measuring ψ and Δ not only as the function of the wavelength λ and incident angle φ of the light beam, but also as the function of the temperature T : $\psi, \Delta (\varphi, \lambda, T)$. Thermo-ellipsometry enables detecting anomalies of the optical properties at the PT in the bulk and thin films, and also evaluate these anomalies at the surface and interface of the thin film heterostructures [30, 31].

The one of the purpose of this work is to show an efficiency of thermo-ellipsometric studies on perovskite ferroelectric structural PT. The NaNbO_3 thin films were chosen, because of high complexity of the PT, and single crystals unlike the thin films of this material were widely explored and there are a lot of experimental data available for comparison.

2.2 Lead zirconate titanate $\text{Pb}(\text{Zr},\text{Ti})\text{O}_3$

In comparison with NaNbO_3 the $\text{PbZr}_x\text{Ti}_{1-x}\text{O}_3$ (PZT) family is much more studied. There are hundreds of scientific publications [97] about PZT while just tenths of papers about NN. PZT is a solid solution of PbTiO_3 and PbZrO_3 compounds. As is the case for most ferroelectric materials, it has an ABO_3 type perovskite structure (Fig. 2.1) where A is a metal ion with a +2 valence (e.g., Pb) and B is a metal ion with a +4 valence (e.g., Ti, Zr). In the case of PZT, the A positions (corners of the cube) are occupied by Pb^{2+} ions, B positions (body center) by Zr^{4+} or Ti^{4+} ions, and O^{-2} ions occupy the face centers. PbTiO_3 has a Curie temperature of 490°C , at which it undergoes a first-order phase transition from cubic-paraelectric phase to tetragonal-ferroelectric phase with lattice parameters $c = 4.153 \text{ \AA}$, $a = 3.899 \text{ \AA}$ [98]. In contrast, PbZrO_3 ($a = 5.886 \text{ \AA}$, $b = 11.749 \text{ \AA}$, $c = 8.248 \text{ \AA}$ [99]) is an antiferroelectric material at room temperature with a Curie point equal to 230°C , where a transition from cubic-paraelectric to orthorhombic-antiferroelectric phase occurs. Above the Curie temperature, PZT is cubic over the whole range of compositions. Composition dependence of the lattice constants for epitaxial $\text{PbZr}_x\text{Ti}_{1-x}\text{O}_3$ films grown on $\text{SrRuO}_3(001)$ -buffered $\text{SrTiO}_3(001)$ substrates [100], are shown in Fig. 2.5. The values for PZT ceramics obtained by Shirane and Suzuki [101] are shown for comparison. The discrepancy between the lattice parameters obtained for thin films and those for ceramics arises from strain in the films caused by lattice and thermal mismatch between the films and the substrates as well as by the phase transition upon cooling the films from the growth temperature. The properties of $\text{PbZr}_{1-x}\text{Ti}_x\text{O}_3$ depend the fraction of PbTiO_3 (that is, x) and temperature, according to a PbTiO_3 - PbZrO_3 phase diagram. The phase diagram obtained first by Jaffe [80] in 1971 is given in Fig. 2.2b. The most prominent feature of this diagram is the existence of a “morphotropic phase boundary” (MPB), which divides the ferroelectric region into two parts: a tetragonal Ti-rich region with space group symmetry $P4 \text{ mm}$ and a rhombohedral Zr-rich region, containing high and low-temperature phases $\text{FR}(\text{HT})$ and $\text{FR}(\text{LT})$ with symmetries

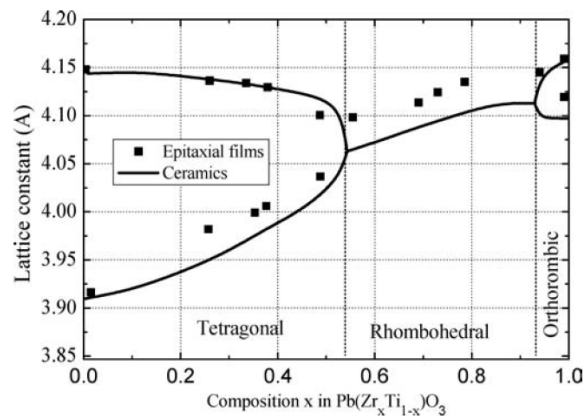


Fig. 2.5. Lattice constants of epitaxial $\text{PbZr}_x\text{Ti}_{1-x}\text{O}_3$ thin films grown at 700°C on epitaxial $\text{SrRuO}_3(001)$ -buffered $\text{SrTiO}_3(001)$ derived from XRD data as a function of composition (solid squares) [101]. The solid lines are the lattice constants for ceramics [101].

$R3m$ and $R3c$, respectively. There is also another particular region at the phase diagram close to PbZrO_3 , where the rhombohedral ferroelectric phase changes into an antiferroelectric orthorhombic phase. The MPB occurs at $x \approx 0.47$, and PZT solid solutions of this composition exhibits superior ferroelectric and piezoelectric properties. It was believed for a long time that increased ferroelectric sensitivity of PZT at MPB was due to coexistence of tetragonal and rhombohedral phases at MPB. More recent structural

studies of PZT revealed a monoclinic phase in the vicinity of what was previously regarded as the boundary separating the rhombohedral and tetragonal regions of the PZT phase diagram [102–104]. Now it is believed that the monoclinic phase is responsible for the unusually high piezoelectric response of PZT. The existence of the monoclinic phase, however, is not irrefutable, and the phase composition at MPB is still open for debate [105].

According to the optical properties of the PZT thin films, there are already several studies in contradistinction to NN thin films, where are no data available on the literature. Optical properties of PZT films of various compositions were measured by a number of authors [97, 100, 106–117], using different techniques, inter alia also spectroscopic ellipsometry [97, 116, 107–112]. The compositional dependence of the refractive index of epitaxial PZT thin films grown on SrRuO₃ (001) buffered SrTiO₃ (001) substrates were reported by Foster [100]. The linear variation of the effective refractive index at 632.8 nm with composition x was found (Fig. 2.6a), which is expected for an ideal solid–solution system. These results showed that for PZT films of sufficient thickness the refractive index data in Figure 2.6 provide a convenient and

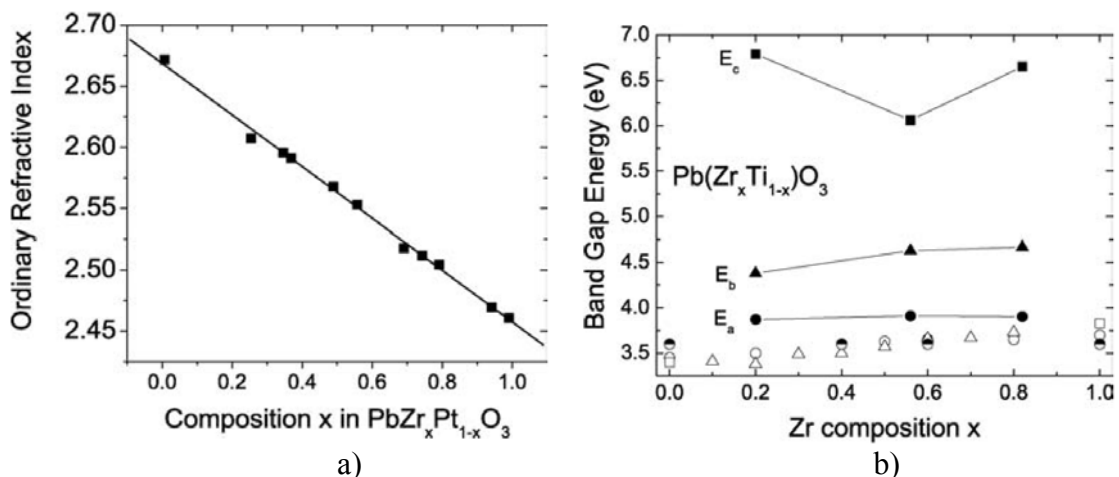


Fig. 2.6. a) Variation of the refractive index at 632.8 nm with composition for epitaxial $\text{PbZr}_x\text{Ti}_{1-x}\text{O}_3$ thin films obtained by prism-coupled waveguide measurements [100]; b) Plot of band gap values of PZT: filled symbols (data obtained by SE, [97]), unfilled circle [106], unfilled triangle [107], unfilled rectangle [118], and half-filled circle [116].

reasonably accurate ($\sim 2\text{--}3\%$) method for quickly determining the composition of the film, specifically the Zr/Ti ratio [97]. It is very important that this ratio is impossible to determine from the optical reflection or transmittance spectra because the band gaps of PbZrO_3 and PbTiO_3 are very close [116]. The band gap energy values as a function of Zr composition reported by Lee [113] and those from other references [116, 106, 107, 118] are given in Fig. 2.6b. Lee [112] used the standard critical point (SCP) fitting to the second derivative of the dielectric function in the deep UV spectral range and could fit the higher band-gap energy E_c . It can be seen from Figure 2.7, the band gap energies E_a and E_b increase only slightly with increasing Zr composition, suggesting that the substitution of Ti by Zr does not change much the electronic band structure of PZT. The band gap energy reported by Lee [112] is $\sim 0.1\text{--}0.4$ eV larger than the values reported by other authors. The discrepancy may be due to the fact that Lee [110, 112] determined the band gap values using the SCP line shape fitting and other authors found these values from the slope of optical absorption coefficient as a function of energy. For example, Peng [119] estimated the optical band gap energies using the absorption spectra. This method is less accurate and tends to underestimate the band gap energy.

But the question lies only on the precision of the technique. If we look more closely to the Fig. 2.4b we can see that E_g detected by Tauc relation [106, 107, 116, 118] shows, that E_g changes by $\sim 0.2 - 0.3$ eV by increase of the Zr concentration. The amount of the change is similar like with the case of refractive index dependence on x (Fig. 2.4a). If there is technique, which can evaluate the precise enough absorption dependence on the photon energy, and have appropriate fit to the experimental data, then, from the authors' point of view, the $E_g(x)$ depended also can be used to determinate the Zr/Ti ratio of the PZT thin films. And one of such technique can be spectroscopic ellipsometry due to its high precision and accuracy.

There is a number of publications devoted to optical properties of PZT, but these properties are still relatively poorly investigated, especially according to the optical gradient of the PZT thin films. The increase of interest in graded refractive index films for applications in optical devices, for instance, rugate filters [8], anti-reflection coatings [9] is observed not long time ago, and importance to study optical properties depth profile of thin films are very significant. A challenging aspect accordingly to the PZT thin film studies lies in the development of an appropriate characterization method of the optical gradient. There is report on detected concentration gradient of the chemical element of the PZT thin films studied by high resolution TEM [20]. Nicolas Ledermann and *et al* studied sol-gel PZT thin films composition with $x = 0.3, 0.4, 0.45, 0.53$ and 0.6 . PZT thin films were deposited on platinized silicon wafers by multiple spin coating of the solution precursors, each layer was subsequently slowly (ramp of 20°C/s) pyrolyzed at 350°C for 15 s. After the deposition of four single layers (three layers with 10% lead excess, one layer with 30% lead excess), the PZT film was thermally annealed at 650°C for 1 min or 12 min using a rapid heating module in flowing oxygen [20]. Increase of Zr and decrease of Ti from the bottom to the top of the layers (Fig. 2.7) was found by TEM for these PZT thin films. The lead was increasing in all layers from the bottom of to the top of the films (Fig. 2.7). However, the sample preparation for TEM investigations is tedious and time consuming. Investigations using other methods such as Rutherford back-scattering (RBS) result in the sample modification or even destruction after the analysis. As a non-destructive technique, spectroscopic ellipsometry (SE) has long been recognized as a powerful method for the characterization of the thin films and its inhomogeneity [21 – 34, 85, 97, 116, 107-112, 121 - 132].

SE was already applied to the refractive index depth profile studies of the oxynitride SiO_2N_x films [21 - 24] (additionally confirmed by chemical etching [24]), lead silicate glass [25], oxidized copper layers [26], polymers [27], semiconductor indium tin oxide (ITO) films [28, 29], and RF-sputtered self-polarized PZT thin films, approved by discharge optical emission spectroscopy (GD-OES) and pyroelectric profile measurements by the laser intensity-modulation method (LIMM) [30, 31]. SE was also applied to the determination of an ion implantation depth profile of silicon wafers and

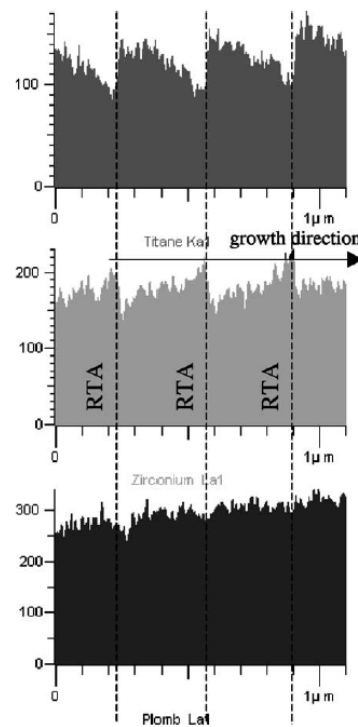


Fig. 2.7. Ti, Zr and Pb EDX chemical analysis profile, arbitrary units [20].

confirmed by the RBS [32, 33]. Sensitivity of the SE was shown to graded oxygen compositions in $\text{YBa}_2\text{Cu}_3\text{O}_{7-\delta}$ (YBCO) thin films detecting changes in the oxygen concentration to within one unit cell [34].

According to theoretical prediction [120], the behavior of polarization profile changes considerable for very thin PZT films. This is illustrated on Fig.2.8a. In this case, the film polarization decreases monotonous with thickness. Fig.2.8b compares the theoretically calculated (solid lines) and three PZT films of different thickness [30, 31]. But for the knowledge of the author of this work there are no studies done on sol-gel PZT thin film inhomogeneity investigations done by optical techniques. Due to the broad technical applications of sol-gel PZT thin films, for example, actuated micromirror for fine-tracking mechanism of high-density optical data storage [7], various sensors, nonvolatile and dynamic random access memories, tunable capacitors for high-frequency microwave applications, electro-optic modulators, applications in

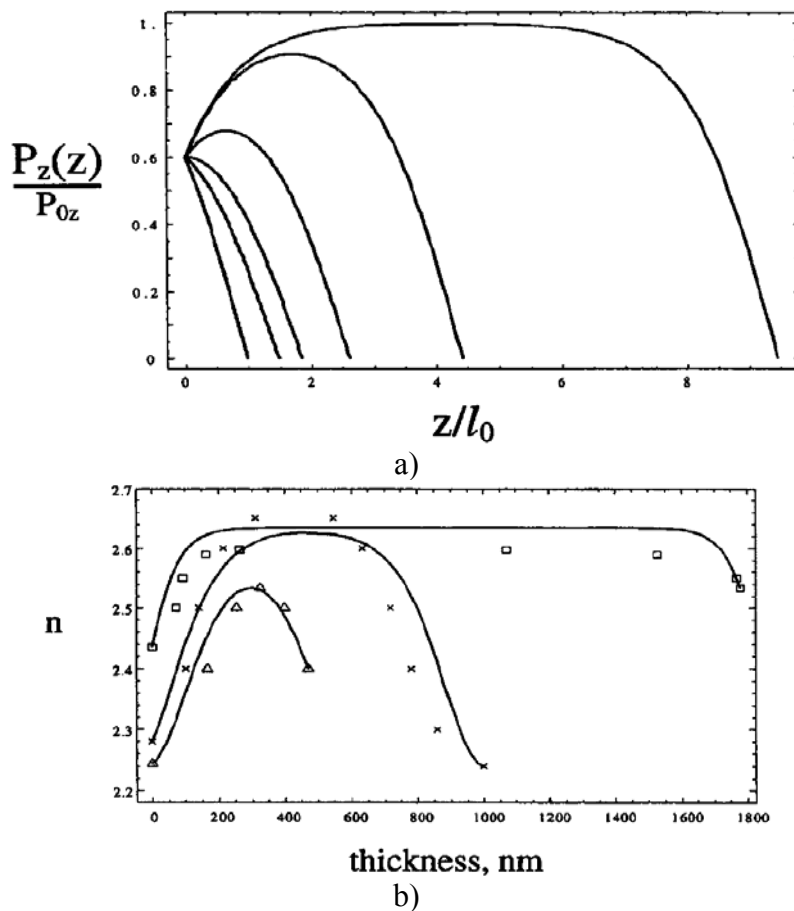


Fig. 2.8. a) Polarization profiles for the films with different thickness; b) Theoretical and experimental results of PZT films refractive index profile [30, 31].

optical devices, for instance, rugate filters [8], anti-reflection coatings [9], infrared detectors, and microelectromechanical systems, the understanding of the chemical composition and physical properties resulting from different processing methods is crucial. The variation of chemical composition with film thickness mirrors in the variation of physical properties of the film. Thus, the knowledge of the compositional gradient within the film allows identification and further optimization of the thin film performance. In this work SE will be applied to investigate sol-gel PZT thin films optical depth profile, as well as optical properties, interface, optical band gap, and surface roughness dependency on the thickness.

3. Reflectometry and ellipsometry

3.1 Introduction

Ellipsometry and reflectometry are currently being used extensively in industry to measure the thickness, optical properties, electronic and lattice vibrational properties for studying of different kinds of materials, including crystals, and thin films of semiconductors, conductors, dielectrics and ferroelectrics. Two specifications of this class of techniques are reflectometry and ellipsometry. The increased speed of reflectometry and the small spot size makes it a desirable tool for the large number of measurements required for statistical process control on a patterned wafer. Both techniques are also used for analyzes, where the structure (and optical constants) is often unknown. Ellipsometry is preferable for measuring very thin layers, that is, submonolayer coverage to several tens of atoms deep. But there are not the only one possibilities of Ellipsometry.

In the paper [121] was demonstrated the use of ellipsometry for the characterization of thin polyfluorene (PFO) films. They investigated the electronic properties of PFO by analyzing ellipsometry data; demonstrated the interference enhancement variable angle spectroscopic ellipsometry suitability for the measurement of film birefringence; showed that temperature dependent ellipsometry can be used to monitor conjugated polymer phase transitions, and to deduce glass and crystalline phase transition temperatures.

M. Campoy-Quiles proposed generalized ellipsometry as a powerful tool for measurement of anisotropic optical function spectra of biaxial materials [122]. He demonstrates generalized ellipsometry for precise measurement of the principal indices of refraction, the extinction coefficients, and the orientations of the crystal a , b , and c axes of orthorhombic absorbing materials.

The work of B.J. Gibbons [34] describes the sensitivity of spectroscopic ellipsometry (SE) to graded oxygen compositions in $\text{YBa}_2\text{Cu}_3\text{O}_{7\pm\delta}$ (YBCO) thin films. Specially, the ability of SE to deduce slight differences in the graded oxygen compositions of films that are otherwise the same was explored. It was shown for c -axis oriented films that SE is, in principle, sensitive to changes in the oxygen concentration to within one unit cell, even when the oxygen profile is graded.

A new method of the anisotropy micro-ellipsometry (AME) was developed by A. Michaleis [123, 124] Ellipsometric measurements on crystalline, homogeneous areas of anisotropic materials show a strong sensitivity on the crystallographic orientation of the system. The application of AME allows one to determinate both standard parameters such as layer thicknesses and optical constants (for ordinary and extraordinary rays) and the orientation of the c axes of the substrate and layer [123]. Later he showed that with AME the crystallographic orientation angles φ of the substrate grains can be determined prior to oxide formation [124].

These are just few examples of the high sensitivity of ellipsometry and wide applications. In this work spectroscopic ellipsometry will be showed as a tool to detect phase transition of the ferroelectric thin films. This positive point of this technique is that it does not requires a specific sample preparation before experiment, and it is non-destructive, and sample do not need to have top electrodes as in case of the dielectric measurements.

The reflectometry was used to quickly detect the thickness of the films. And specific case of ellipsometry – a null-ellipsometry, was applied to evaluate precise optical properties at

the single wavelength. These data afterwards were used to fit the spectroscopic ellipsometry data. The author of this work acquired experience on nul-elipsometry and reflectometry during development of the bachelor's work [38b] and master's work [39c]. The basic idea and main results are presented in [39d]. In this chapter a brief discussion about basics of reflectometry and ellipsometry are given.

3.2 Reflectometry

The basic principle behind a reflectometry experiment is very simple – the intensity of light is measured before and after it reflects from the sample under study. The ratio of the intensity of the reflected beam to the intensity of the incident beam is termed the absolute reflectance of the sample. It is generally very difficult to directly measure the intensity of the light beam before it strikes the sample under test, so that most measurements of reflectance involve the measurements of relative reflectance.

From a macroscopic point of view, the quantities of interests are the amplitude of the incoming wave and the amplitude of the resulting outgoing wave; or the ratio of them – total reflection coefficient, which are analogous to the Fresnel reflection coefficients. Let us have electromagnetic wave falling on the stack of the j layers (Fig. 3.1) with thickness d_j at the incident angle φ_0 . The layers are isotropic, continued with the sharp borderlines. This is the case of the multilayer model, which is very useful to describe isotropic thin films and heterogeneous films by using homogenous layers (first solved Abbe).

The multilayer system matrix for p and s polarized light describes the system [125]

$$\tilde{M}_{ij s,p} = \tilde{I}_{01 s,p} \tilde{L}_1 \tilde{I}_{12 s,p} \tilde{L}_2 \cdot \dots \cdot \tilde{I}_{ij s,p} \tilde{L}_j \tilde{I}_{j+1} \quad (3.1)$$

where $\tilde{I}_{ij s,p}$ – boundary interface matrix for p and s polarized light, \tilde{L}_j – layer matrix, $i = 0, 1, \dots, j-1, j = 1, 2, \dots, j$. The boundary condition [125] for the wave passing from the one ambience to another is

$$\tilde{I}_{ij s,p} = \frac{1}{t_{ij s,p}} \begin{pmatrix} 1 & r_{ij s,p} \\ r_{ij s,p} & 1 \end{pmatrix} \quad (3.2)$$

$$\tilde{L}_j = \begin{pmatrix} e^{i\beta_j} & 0 \\ 0 & e^{-i\beta_j} \end{pmatrix}, \quad (3.3)$$

where $\beta_j = \frac{2\pi d_j n_j}{\lambda} \cos \varphi_j$, $\cos \varphi_j = \sqrt{\frac{1 - n_0^2 \sin^2 \varphi_0}{n_j^2}}$ describes the phase suspension at

the corresponding layer, φ_0 - the incidence angle of the light, φ_j - angle of refraction for the j layer, which can be found by applying the Schnell low of reflection for all layers, n_0 - refraction coefficient for the zero ambient and n_j , d_j - refraction coefficient and thickness for the j layer, $r_{ij s,p}$ and $t_{ij s,p}$ - reflection and transmittance coefficients for the p and s polarized light for the corresponding boundary. Reflection and transmittance coefficients can be found from Fresnel formulas

$$r_{ij p} = \frac{n_j \cos \varphi_i - n_i \cos \varphi_j}{n_j \cos \varphi_i + n_i \cos \varphi_j}, \quad t_{ij p} = \frac{2n_i \cos \varphi_i}{n_j \cos \varphi_i + n_i \cos \varphi_j}, \quad (3.4)$$

$$r_{ij s} = \frac{n_i \cos \varphi_i - n_j \cos \varphi_j}{n_i \cos \varphi_i + n_j \cos \varphi_j}, \quad t_{ij s} = \frac{2n_i \cos \varphi_i}{n_i \cos \varphi_i + n_j \cos \varphi_j}. \quad (3.5)$$

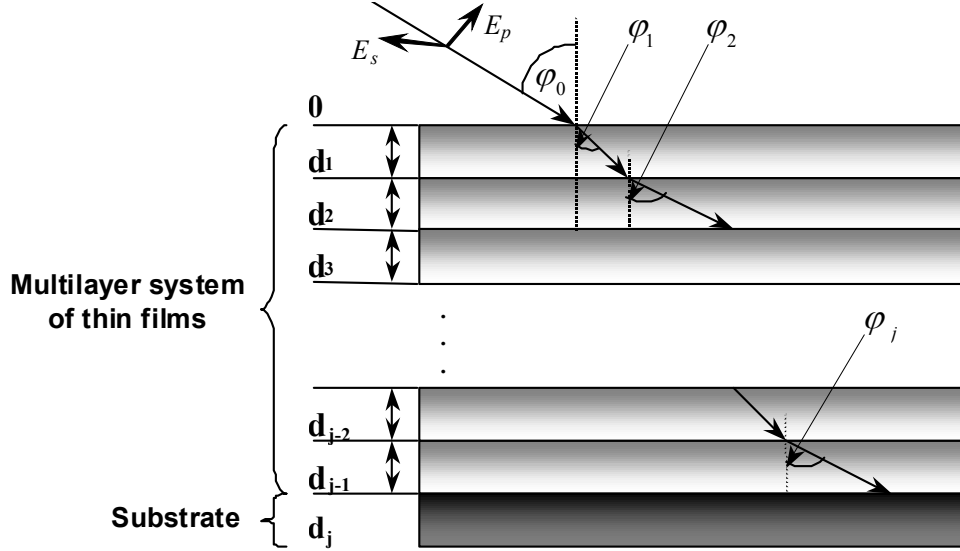


Fig. 3.1. Scheme of the multilayer model.

Reflective properties for the sample can be ascribed using layer and interface matrix for polarized light

$$R_p = \frac{\tilde{M}_{21p}}{\tilde{M}_{11p}}, \quad R_s = \frac{\tilde{M}_{21s}}{\tilde{M}_{11s}}, \quad (3.6)$$

where $R_p = |r_p|^2$, and $R_s = |r_s|^2$.

These total reflective coefficients are connected with the main ellipsometric angles ψ and Δ

$$\tan \psi = \frac{|r_p|}{|r_s|} \quad (3.7)$$

$$\text{tg} \psi e^{i\Delta} = \frac{r_p}{r_s} = \gamma, \quad (3.8)$$

where γ is the quantity of ellipticity. The details of ellipsometry and ellipsometric main angles will be discussed below.

3.3 Ellipsometry

Ellipsometry measures the change of the polarization state of light upon grazing reflection. It overcomes two major problems of conventional spectroscopy or reflectivity: the phase problem (in ellipsometry the phase is measured and does not have to be calculated by Kramers-Kronig transform) and the reference problem (ellipsometry requires relative, not absolute, intensities). Paul Drude was the first to study optical properties using the ellipsometry technique. He published the equation of ellipsometry in 1887, and his experimental results in 1888. Generally, after reflection on a sample the polarization state of the light is elliptical (Fig. 3.2). The electrical field components parallel and perpendicular, E_{ip} and E_{is} , with respect to the plane of incidence change their amplitude and phases due to reflection upon the sample.

This reflection is described by two complex reflection coefficients $r_p = |r_p|e^{i\delta_p}$ and $r_s = |r_s|e^{i\delta_s}$. Ellipsometry operates with the ratio γ of two electrical field intensities components $E_{ip}/E_{is} = r_p/r_s = \tan \psi e^{i\Delta} = \gamma$, where the ellipsometric parameters ψ and Δ are

$\tan\psi = |r_p|/|r_s|$, $\Delta = \delta_p - \delta_s$ or in complex the modulus of the ellipticity $|\gamma| = tg\psi$ and argument $Arg\gamma = \Delta$ (Fig. 3.3a). On the other hand, these parameters are functions of the dielectric constants of the sample:

$$\psi = \psi(\varepsilon, \sigma, \omega), \quad (3.9)$$

$$\Delta = \Delta(\varepsilon, \sigma, \omega), \quad (3.10)$$

where ε is the real part of dielectric function, σ is the real part of conductivity, and ω is the frequency. There are two equivalent descriptions: the first one operates with real and imaginary parts of the dielectric function $\varepsilon_1, \varepsilon_2$, the second one operates with the real part of dielectric function and the real part of the conductivity. The ratio between conductivity and dielectric function $\sigma \propto i\omega\varepsilon$ makes these descriptions equivalent.

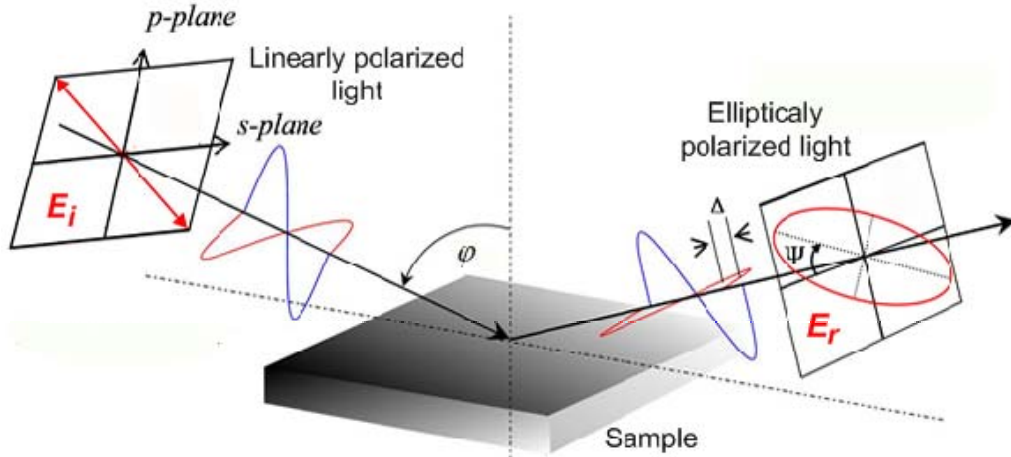


Fig. 3.2. Light reflecting from a sample at angle φ . The linearly polarized incident light has two electric field components E_{ip} and E_{is} in the directions parallel and perpendicular to the propagation plane, respectively. The reflected light has elliptical polarization.

By solving equations (3.9) and (3.10) one can obtain the values of ε and σ at a frequency ω . The specific form of the equations (3.9) and (3.10) depends on the sample type. For the simplest case of an isotropic medium, the solution has the following form:

$$\varepsilon \propto \sin^2 \varphi \left(1 + \frac{\tan^2 \varphi (\cos^2 2\psi - \sin^2 2\psi \sin \Delta)}{(1 + \sin 2\psi \cos \Delta)^2} \right), \quad (3.11)$$

$$\sigma \propto \frac{\sin^2 \varphi \tan^2 \varphi \sin 4\psi \sin \Delta}{(1 + \sin 2\psi \cos \Delta)^2}, \quad (3.12)$$

φ is the angle of incidence. The coefficients of proportionality depend on the unit system used.

According to equations (3.11) and (3.12) the deduced values of the dielectric constants are very sensitive to small errors in the angle of incidence. Therefore, the surface of the sample should be rather well defined and flat, and one should use a collimated incident beam. Significant errors in the angle of incidence will lead to corresponding distortions of the deduced dielectric function. The ellipsometric parameters themselves depend on the angle of incidence φ (Fig 3.3b). In the vicinity of the Brewster angle the ellipsometric parameters, especially Δ , are changing most rapidly. For the ellipsometric measurements to be most sensitive and accurate one thus needs to choose an angle of incidence that is rather close to Brewster's angle of the material. Brewster's angle itself depends on the dielectric properties of the material. For example, in the far infrared it is close to 74 degree for Si and almost 90 degree for metallic or

superconductive samples. One can conveniently characterize the elliptically polarized light with the parameters ψ and Δ (Fig. 3.3c). ψ is the azimuth angle and $|\tan \psi|$ is the ratio of the ellipse axes. The ψ varies from zero to $\pi/4$, but Δ has different conventions: $-\pi/2 < \Delta < \pi/2$ or else $0 < \Delta < \pi$. Both conventions are equivalent since Δ is defined as a phase difference and equations (3.11) and (3.12) only contain $\cos(\Delta)$. Originally ψ and Δ were chosen because they are the output of the original null-ellipsometer. They also have an important physical meaning. The ψ is sensitive to the angle of incidence as compared to Brewster's angle (the angle of minimum intensity of p polarized light), and is minimum at this angle. Therefore, is equal to $\pi/4$ for $\varphi = \pi/2$ and $\varphi = 0$. Δ is related to absorption of the sample. For a transparent sample Δ is either π (below Brewster angle) or 0 (above Brewster angle). In the case of absorption Δ will be between these values and will tend to $\pi/2$ as the absorption increases. The rapid decline in Δ near the Brewster angle indicates that the sample is not very absorptive, smoother decline corresponds to a higher absorption.

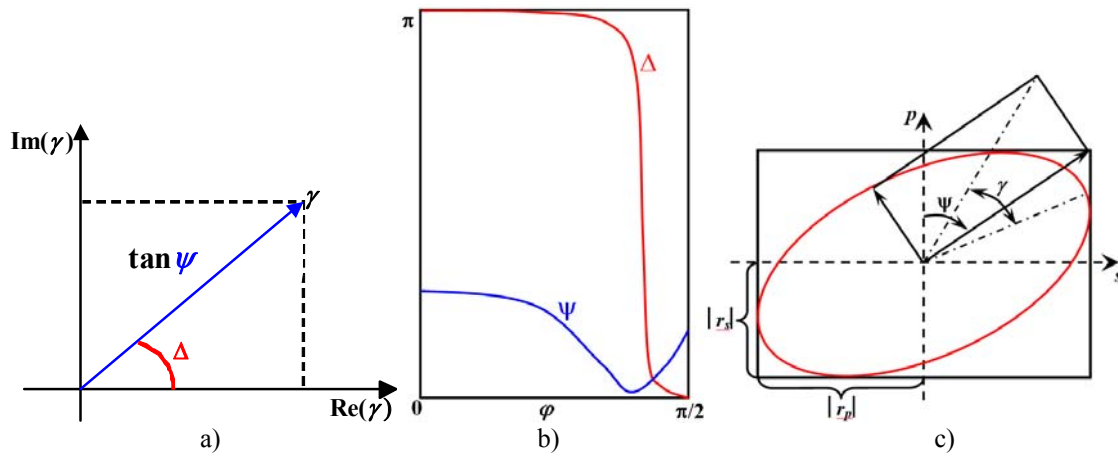


Fig. 3.3. a) main ellipsometric angles ψ and Δ in the complex plane; b) angles ψ and Δ versus the angle of incidence φ ; c) polarization ellipse of the reflected light.

Formulas (3.9) and (3.10) illustrate the simplest way of evaluating the dielectric constants of a sample. In general, one may have to take into account the anisotropy of a material (as is the case for HTSC), imperfections of optical elements in the experimental setup, diffraction effects, depolarization of light, and nonlinear effects. After all, one has to find a good compromise between the complicity of the formalism, the accuracy of the measurement, and the number of effects that need and can be corrected for.

3.3.1 Null-ellipsometry

One needs to measure the parameters ψ and Δ in order to calculate the dielectric constants of a sample using the equations in (3.9) and (3.10). There are several different kinds of ellipsometric setups. One of the oldest ellipsometric configurations is the null ellipsometer [126]. Interesting, this configuration is also one of the most accurate and robust. The configuration of a null ellipsometer is shown in Fig. 4. In a nulling ellipsometer, the light beam passes through a linear polarizer P and a compensator before striking the sample. After reflection from the sample, the beam passes through another compensator K (typically fixed on $+\pi/4$) and analyzer A before striking the detector. Main goal is to adjust the rotational position of P and A in order to completely extinguish (null) the signal from the detector. As the result with the null-ellipsometer the one obtains

main ellipsometric angles directly. Averaging four-zones of P and A (Fig. 3.5), main ellipsometric angles ψ and Δ give very accurate experimental data with few or no systematic errors. For example, at the 1st zone angle of compensator

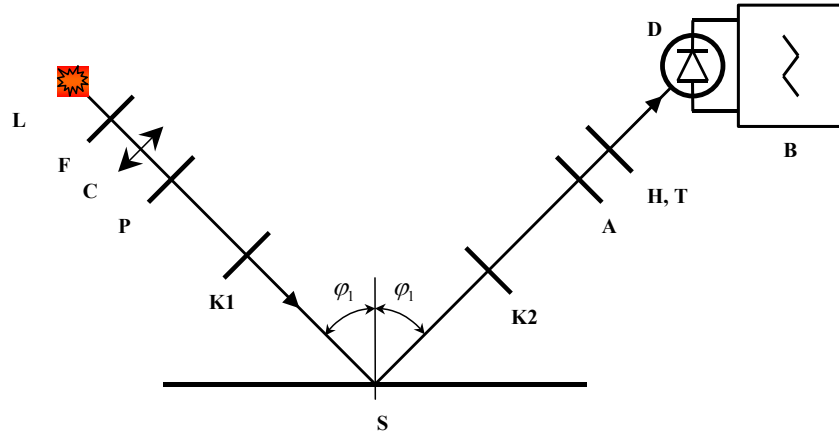


Fig. 3.4. The optical scheme of the null-ellipsometer: light L is going through monochromatic filter F, collimator C, linearly polarizes from polarizer P, passes compensator K1 (it change the phase shift between p and s polarized light), reflects from the sample S, again passes compensator K2, goes through analyzer A and is entered by photodiode D, what is intensified by the electric block B.

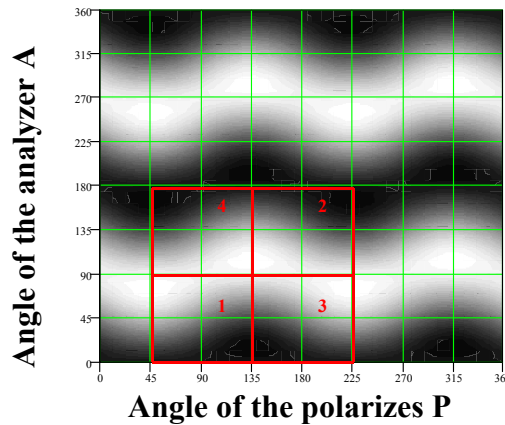


Fig. 3.5. The lanes of the light intensity, dependent on the azimuth position of the analyzer and polarizer. The optimal zones 1, 2, 3 and 4 to search of the light intensity minimum are presented.

Tab. 3.1. Position of the polarizer's azimuths if compensator is fixed.

Zone	Azimuth of compensator	Polarizer P azimuth		Analyzer A azimuth	
		$0 \leq \Delta \leq \pi$	$\pi \leq \Delta \leq 2\pi$	$0 \leq \Delta \leq \pi$	$\pi \leq \Delta \leq 2\pi$
1	$+\pi/4$	$-\pi/4 \leq P_1 \leq \pi/4$	$\pi/4 \leq P_1 \leq 3\pi/4$	$0 \leq A_1 \leq \pi/2$	
2	$+\pi/4$	$\pi/4 \leq P_2 \leq 3\pi/4$	$3\pi/4 \leq P_2 \leq 5\pi/4$	$\pi/2 \leq A_2 \leq \pi$	
3	$-\pi/4$	$\pi/4 \leq P_3 \leq 3\pi/4$	$3\pi/4 \leq P_3 \leq 5\pi/4$	$0 \leq A_3 \leq \pi/2$	
4	$-\pi/4$	$-\pi/4 \leq P_4 \leq \pi/4$	$\pi/4 \leq P_4 \leq 3\pi/4$	$\pi/2 \leq A_4 \leq \pi$	
$A_1 + A_4 = A_2 + A_3 = \pi; \quad P_2 + P_4 = 0, \pi; \quad P_2 + P_3 = \pi, 2\pi$					

is $Q_1 = +\pi/4$, and the null of light can be found by rotating P and A by a definite angles, when $-\pi/4 \leq P_1 \leq \pi/4$ or $\pi/4 \leq P_1 \leq 3\pi/4$ and $0 \leq A_1 \leq \pi/2$. If measurements runs at the 3^d and the 4th zones, then

$$\psi = \frac{1}{2} (180 - A_4 + A_3) \text{ and} \quad (3.13)$$

$$\Delta = 360 - (P_3 + P_4 - 180) \quad (3.14)$$

(see for details [127]). The position of the azimuth of the P and A by zones, when K is fixed, are summarized in Tab. 3.1.

3.3.2 Rotating analyzer ellipsometry

The present experiments have been performed with a so-called rotating analyzer ellipsometer where the sample is placed between two polarizers [85] one of which is rotated while the other one is kept fixed as sketched in Figure 3.6. The components are a monochromatic light source, an ideal polarizer oriented at the angle α_1 , the reflection at angle φ upon the ideal sample which is described by the parameters ψ and Δ , a second rotating ideal polarizer (the so-called analyzer) placed behind the sample, and an ideal detector that measures the intensity depending on the analyzer angle. The detector sensitivity must be independent from the polarization state of the incoming light. In this ideal case the relative intensity will have the form

$$I(\alpha_2)/I_0 = 1 + A \cos 2\alpha_2 + B \sin 2\alpha_2, \quad (3.15)$$

$$\text{where } A = \frac{\cos 2\alpha_1 - \cos 2\psi}{1 - \cos 2\psi \cos 2\alpha_1} \text{ and } B = \frac{\sin 2\psi \sin 2\alpha_1 \cos \Delta}{\cos 2\alpha_1 - \cos 2\psi}.$$

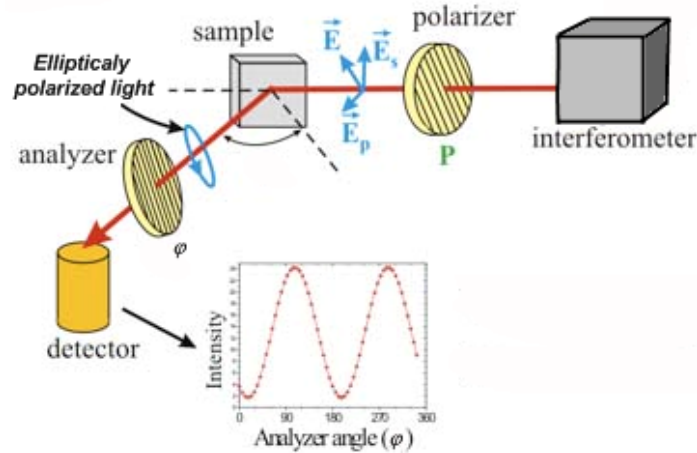


Fig. 3.6. Illustrative scheme of the rotating analyzer ellipsometry.

From the measured dependence of $I(\alpha_2)$ the coefficients A and B can be obtained by performing a fit to the experimental data in form of 1.5. Accordingly ψ and Δ are

$$\tan \psi = \tan \alpha_1 \sqrt{\frac{1-A}{1+A}} \text{ and } \cos \Delta = \frac{B}{\sqrt{1-A^2}}. \quad (3.16)$$

Eventually, from ψ and Δ one obtains the dielectric constants by using equations (3.11) and (3.12). The extension of ellipsometry to a wide spectral range requires either the use of a monochromator (typically based on gratings) or a so-called Fourier transform interferometer.

3.4 Generalized ellipsometry

3.4.1 Dielectric constant extraction from ellipsometric parameters

There are two common ways to determine the influence of linear optical elements on light. Using these methods one can find relations between ellipsometric parameters, detected intensity and parameters of a setup. These two methods are called the Muller matrix formalism and the Jones matrix formalism. The advantage of matrix formalism is that each element of an ellipsometer can be considered separately, and then matrices multiplied to obtain the complete relationship between the incoming light and the detected intensity for the cases of different samples and different ellipsometric configurations. The Jones matrix formalism uses 2×2 complex matrices is the simplest of these two methods. The Muller matrix formalism operates with 4×4 matrices and is necessary to consider partially polarized light. More detailed description of the Jones and Muller formalisms can be found in the works of Azzam and Bashara [128] and Tompkins [85].

3.4.2 Polarization States of Light

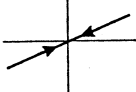
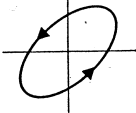
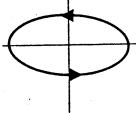
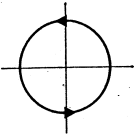
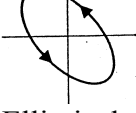
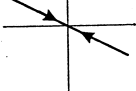
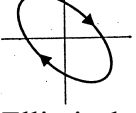

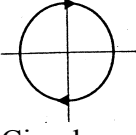
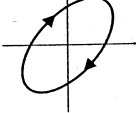
In this section, basic parameters of polarized light are considered. So, completely polarized light can be represented as

$$\vec{E} = \Re \left[\vec{E}_0 e^{i\vec{k}^L \vec{r} - i\omega t} \right] \quad (3.17)$$

where \vec{E}_0 is the complex amplitude of the light, ω is the angular frequency, \vec{k}^L is the wave vector, t is time, and \vec{r} is the position vector, \Re is the real part function.

The equation (1.7) can be broken into two components as

Tab. 3.2. Polarization types according to the value of phase shift and amplitudes of the electric field.

Phase shift	Polarization	
	$E_{0p} \neq E_{0s}$	$E_{0p} = E_{0s}$
$\delta_p - \delta_s = 0^\circ$		
	Linear	
$0^\circ < \delta_p - \delta_s < 90^\circ$		
	Elliptical	
$\delta_p - \delta_s = 90^\circ$		
	Elliptical	Circular
$90^\circ < \delta_p - \delta_s < 180^\circ$		
	Elliptical	
$\delta_p - \delta_s = 180^\circ$		
	Linear	
$180^\circ < \delta_p - \delta_s < 270^\circ$		
	Elliptical	
$\delta_p - \delta_s = 270^\circ$		
	Elliptical	Circular
$270^\circ < \delta_p - \delta_s < 360^\circ$		
	Elliptical	

$$\begin{aligned}\bar{E} &= \Re \left\{ \begin{bmatrix} \bar{E}_{0p} \\ \bar{E}_{0s} \end{bmatrix} e^{i\bar{k}^L \bar{r} - i\omega t} \right\} = \\ &= \Re \left\{ \begin{bmatrix} |E_{0p}| \bar{E}_{0p} e^{i\delta_p^L} \\ |E_{0s}| \bar{E}_{0s} e^{i\delta_s^L} \end{bmatrix} e^{i\bar{k}^L \bar{r} - i\omega t} \right\} \quad (3.18)\end{aligned}$$

here \bar{E}_{0p} , \bar{E}_{0s} , δ_p^L , δ_s^L are amplitudes and phases of the electric field components that are parallel (p polarization) and perpendicular (s polarization) to the plane of incidence, respectively. As a result, we have the electric field tracing out an ellipse as a function of time. To connect it with ellipsometry one defines the parameters ψ and Δ as

$$\tan \psi^L = \frac{|E_{0p}|}{|E_{0s}|}, \quad (3.19)$$

$$\Delta^L = \delta_p^L - \delta_s^L. \quad (3.10)$$

ψ^L is related to the tilt of the ellipse, and Δ^L is related to the eccentricity of the ellipse, being 0 or π for circular polarization, when $E_{0p} = E_{0s}$. All types of polarization, depending from phase shift and amplitudes of electric field, are summarized in Tab. 3.2. If a sample is described in terms of ψ and Δ defined through the reflective index then the light reflected from the sample will have $\psi^L = \psi$ and $\Delta^L = \Delta$.

3.4.3 Muller matrix formalism

The Muller matrix formalism is associated with the Stokes parameters of light. For a completely polarized wave, these parameters are defined as [85]

$$s_0 = |E_{0p}|^2 + |E_{0s}|^2 \quad (3.11)$$

$$s_1 = |E_{0p}|^2 - |E_{0s}|^2 \quad (3.12)$$

$$s_2 = 2|E_{0p}||E_{0s}|\cos\Delta^L \quad (3.13)$$

$$s_3 = 2|E_{0p}||E_{0s}|\sin\Delta^L \quad (3.14)$$

These quantities have the dimensions of intensity and represent the different possible states of polarization of a quasi-monochromatic electromagnetic wave. Partially polarized and unpolarized light is included by the use of Stokes parameters. The value s_0 is proportional to the energy of a light wave, s_1 adds information about its polarization ellipse, while s_2 and s_3 contain information about the eccentricity of the ellipse. Using Stokes parameters, we can obtain the following relations for the ellipsometric angles

$$s_1/s_0 = -\cos 2\psi^L \quad (3.15)$$

$$s_2/s_0 = \sin 2\psi^L \cos \Delta^L \quad (3.16)$$

$$s_3/s_0 = \sin 2\psi^L \sin \Delta^L \quad (3.17)$$

Following from (3.15 – 3.17) the four Stokes parameters are not independent for the case of completely polarized light since:

$$s_0^2 = s_1^2 + s_2^2 + s_3^2 \quad (3.18)$$

In the opposite case of unpolarized light $E_{0p} = E_{0s}$, and Δ^L is a rapidly varying random function ($\cos\Delta^L = \sin\Delta^L = 0$ on average), so that $s_0 > 0$ and $s_1 = s_2 = s_3 = 0$. Partially polarized light can be presented as the sum of completely polarized and unpolarized components, and we have another relation instead of (3.18), namely

$$\begin{aligned}
s_0 &= s_{0u} + s_{0p} = \\
&= s_{0u} + \sqrt{s_1^2 + s_2^2 + s_3^2}
\end{aligned} \tag{3.19}$$

where s_{0u} , s_{0p} are the intensities of unpolarized and polarized parts of the light, correspondingly. The degree of polarization is the ratio of the intensity of the polarized component to the one of the total wave

$$P_{0l} = \frac{s_{0p}}{s_0} = \frac{\sqrt{s_1^2 + s_2^2 + s_3^2}}{s_0} \leq 1 \tag{3.20}$$

This formula has a simple geometric interpretation. Since $P_{0l} = 0$ is unpolarized light, each point on the surface of the unit sphere, $P_{0l} = 1$, represents a distinct totally polarized state. Excluding the origin, a point inside the unit sphere, $0 < P_{0l} < 1$ represents a partially polarized wave. The equality holding for the case of totally polarized light, where equations (3.15 – 3.17) are valid. The transformations of the Stokes parameters are carried out by the 4x4 Muller matrix. The processing of the light wave by the optical system is calculable from the premultiplication of an incident Stokes vector by the system of Muller matrix to produce the Stokes vector of the outgoing wave. Note that the elements of the Muller matrix are real. And we have

$$\vec{S}_e = M \vec{S}_i \tag{21}$$

where M is the Muller matrix, and \vec{S}_e and \vec{S}_i are the Stokes vectors of the final and initial polarization states, respectively. These vectors are of the form

$$\vec{S} = \begin{pmatrix} s_0 \\ s_1 \\ s_2 \\ s_3 \end{pmatrix} \tag{3.22}$$

The important property of the Muller matrix is that one can compute the matrix of a cascaded optical system by multiplication

$$M = M_N M_{N-1} M_{N-2} \dots M_1 = \prod_{i=1}^N M_i \tag{3.23}$$

This allows one to calculate intensity at a detector as the final result of all multiplications of an initial Stokes vector to Muller matrices of each optical element of the system. The necessary matrices are as follows: the Muller matrix for ideal polarizer with orientation φ

$$M_P = \frac{1}{2} \begin{pmatrix} 1 & \cos 2\varphi & \sin 2\varphi & 0 \\ \cos 2\varphi & \cos^2 2\varphi & \sin 2\varphi \cos 2\varphi & 0 \\ \sin 2\varphi & \sin 2\varphi \cos 2\varphi & \sin^2 2\varphi & 0 \\ 0 & 0 & 0 & 0 \end{pmatrix} \tag{3.24}$$

The linear retarder with retardation δ

$$M_R = \begin{pmatrix} 1 & 0 & 0 & 0 \\ 0 & 1 & 0 & 0 \\ 0 & 0 & \cos \delta & \sin \delta \\ 0 & 0 & -\sin \delta & \cos \delta \end{pmatrix} \tag{3.25}$$

An ideal isotropic reflecting surface with the ellipsometric angles ψ and Δ defined in the x - y coordinate system of Stokes vectors has the following Muller matrix, resulting from the Jones matrix

$$M_S = \frac{|r_x|^2 + |r_y|^2}{2} \begin{pmatrix} 1 & -\cos 2\psi & 0 & 0 \\ -\cos 2\psi & 1 & 0 & 0 \\ 0 & 0 & \sin 2\psi \cos \Delta & \sin 2\psi \sin \Delta \\ 0 & 0 & -\sin 2\psi \sin \Delta & \sin 2\psi \cos \Delta \end{pmatrix} \quad (3.26)$$

the partial linear polarizer with the maximum and minimum transmittances τ_M and τ_m

$$M_{part} = \frac{1}{2} \begin{pmatrix} \tau_M + \tau_m & \tau_M - \tau_m & 0 & 0 \\ \tau_M - \tau_m & \tau_M + \tau_m & 0 & 0 \\ 0 & 0 & 2\sqrt{\tau_M \tau_m} & 0 \\ 0 & 0 & 0 & 2\sqrt{\tau_M \tau_m} \end{pmatrix} \quad (3.27)$$

The matrix (1.27) is similar to (1.26) with ellipsometric parameters $\psi = \Delta = 0$.

Now we consider the transformations of Stokes vector and Muller matrix under rotation of a Cartesian coordinate system. Let \vec{S}' and M' be the Stokes vector and Muller matrix in the system having been rotated to the angle α , and \vec{S} and M represent these quantities in the original system. Then the transformation laws from M to M' and from \vec{S} to \vec{S}' are follows

$$\vec{S}' = R(\alpha) \vec{S} \quad (3.28)$$

$$\vec{M}' = R(\alpha) M R(-\alpha) \quad (3.29)$$

where R is the rotator matrix given by

$$R(\alpha) = \begin{pmatrix} 1 & 0 & 0 & 0 \\ 0 & \cos 2\alpha & \sin 2\alpha & 0 \\ 0 & -\sin 2\alpha & \cos 2\alpha & 0 \\ 0 & 0 & 0 & 1 \end{pmatrix} \quad (3.30)$$

Thus, using Muller matrices, one obtains the Stokes vector for the light passing through a polarizer, bouncing off the sample, passing through an analyzer and finally getting on the detector \vec{S}_d

$$\vec{S}_d = M_A M_S M_R M_P \begin{pmatrix} I_0 \\ 0 \\ 0 \\ I_d \end{pmatrix} \quad (3.31)$$

here I_0 is the intensity of the beam in front of a polarizer. The element I_d is the intensity in front of the detector S_d . Looking at the representations of Muller matrices for the work elements of the device, one can conclude that the ratio of intensities I_d/I_0 is a function of the analyzer angle, the polarizer angle, the angle of incidence, and the ellipsometric parameters ψ and Δ of a sample. These conclusions are also valid for the remaining parameters of the Stokes vector s_1, s_2, s_3 . Since characteristics of the analyzer and the polarizer are known, one can obtain the values of ψ and Δ , and afterwards, the dielectric function of the sample. The specific realization and accuracy depends on the approach and Muller matrices used for the description of known elements of the optical system.

3.4.4 Jones matrix formalism

We consider the propagation of a uniform monochromatic plane wave $\vec{E}(x, y, z, t) = \vec{E}_0(x, y, t)e^{ikz}$. The electric field of this wave can be represented as a 2×1 vector, the so-called Jones vector

$$\vec{E}_0 = \begin{pmatrix} E_x \\ E_y \end{pmatrix} \quad (3.32)$$

For ellipsometry it is convenient to direct the axes x and y along p and s polarizations respectively, then $E_x = E_p$ and $E_y = E_s$. From this time dependent 2×1 Cartesian Jones vector the 2×2 coherency matrix can be constructed by the direct multiplication of \vec{E}_0 to its Hermitian adjoin (defined as complex conjugate of transpose of the matrix)

$$\vec{J} = \langle \vec{E}_0(t) \times \vec{E}_0^\dagger(t) \rangle = \begin{pmatrix} \langle E_x E_x^* \rangle & \langle E_x E_y^* \rangle \\ \langle E_x E_y^* \rangle & \langle E_y E_y^* \rangle \end{pmatrix} \quad (3.33)$$

The brackets $\langle \rangle$ denote the time averaging. Eventually, we have obtained 2×2 time independent coherence matrix, which is also called Jones matrix. The elements J_{xx} , J_{yy} present the intensities of the x and y wave components, and total intensity can be calculated as the trace of this matrix. For a monochromatic wave, products E^* appear to be time independent, and the Jones matrix assumes the form

$$\vec{J} = \begin{pmatrix} a_x^2 & a_x a_y e^{i\Delta} \\ a_x a_y e^{-i\Delta} & a_y^2 \end{pmatrix} \quad (3.34)$$

where $a_x = |E_x|$, $a_y = |E_y|$ are the magnitudes of the wave components, $\Delta = \delta_x - \delta_y$ is the ellipsometric parameter of the wave. By virtue of the definition of Stokes parameters (see formulae 3.11-3.14), they can be presented as functions of Jones matrix elements and vice versa

$$s_0 = a_x^2 + a_y^2 = J_{xx} + J_{yy} \quad (3.35)$$

$$s_1 = a_x^2 - a_y^2 = J_{xx} - J_{yy} \quad (3.36)$$

$$s_2 = 2a_x a_y \cos \Delta = J_{xy} + J_{yx} \quad (3.37)$$

$$s_3 = 2a_x a_y \sin \Delta = -i(J_{xy} - J_{yx}) \quad (3.38)$$

$$J_{xx} = \frac{1}{2}(s_0 + s_1) \quad (3.39)$$

$$J_{yy} = \frac{1}{2}(s_0 - s_1) \quad (3.40)$$

$$J_{xy} = \frac{1}{2}(s_2 + is_3) \quad (3.41)$$

$$J_{yx} = \frac{1}{2}(s_2 - is_3) \quad (3.42)$$

The relations between Stokes vector and Jones matrix elements can be rewritten in the matrix form [85]

$$\begin{pmatrix} s_0 \\ s_1 \\ s_2 \\ s_3 \end{pmatrix} = \begin{pmatrix} 1 & 0 & 0 & 1 \\ 1 & 0 & 0 & -1 \\ 0 & 1 & 1 & 0 \\ 0 & -i & i & 0 \end{pmatrix} \begin{pmatrix} J_{xx} \\ J_{xy} \\ J_{yx} \\ J_{yy} \end{pmatrix}. \quad (3.43)$$

Coordinate transformations that transform Jones vector with the transforming matrix R change the Jones matrix \vec{J} according to the following law

$$\vec{J}' = R \vec{J} R^\dagger \quad (3.44)$$

Note, that under unitary transformations the determinant and the trace of a Jones matrix remain invariant.

Let us assume that in front of a linear optical element, we have the Jones vector \vec{E}_0 , and \vec{E}'_0 on the output of the element. Due to linearity, \vec{E}'_0 and \vec{E}_0 are coupled by a linear transformation which is denoted as a matrix T . Then, by virtue of (3.32), one has obtained the Jones matrix transformation caused by this optical element:

$$\vec{J}' = T \vec{J} T^\dagger \quad (3.45)$$

The matrix T is called the Jones matrix of the element, and can be applied for both transformations: of Jones vectors and of Jones matrices. The relation (3.45) can be easily extended to a cascade of consistent linear elements, and the resulting Jones matrix will be the product of Jones matrices of all elements composing the device. Jones matrices for devices used in the ellipsometry have been calculated and are known. So, a linear polarizer oriented at the angle φ has Jones matrix

$$T(\varphi)_P = \begin{pmatrix} \cos^2 \varphi & \sin \varphi \cos \varphi \\ \sin \varphi \cos \varphi & \sin^2 \varphi \end{pmatrix}. \quad (3.46)$$

A retarder with the azimuth α and relative retardation δ

$$T(\varphi, \delta)_R = \begin{pmatrix} \cos(\delta/2) + i \cos 2\varphi \sin(\delta/2) & i \sin 2\varphi \sin(\delta/2) \\ i \sin 2\varphi \sin(\delta/2) & \cos(\delta/2) + i \cos 2\varphi \sin(\delta/2) \end{pmatrix}. \quad (3.47)$$

A reflecting surface with reflection coefficients $r_p e^{i\delta_p}$ and $r_s e^{i\delta_s}$ ($r_p, r_s, \delta_p, \delta_s \in \mathfrak{R}$ to be responsible the amplitude and phase changes)

$$T = \begin{pmatrix} r_p e^{i\delta_p} & 0 \\ 0 & r_s e^{i\delta_s} \end{pmatrix}. \quad (3.48)$$

Now apply the Jones matrices formalism described above to the Ellipsometry device the scheme of which is depicted in Fig. 2c. Let \vec{E}_0 be the electric field of the wave in front of the polarizer. Further, the wave reflects on the sample and comes through the analyzer, and the field \vec{E}'_0 in front of a detector can be presented according to the relation (3.45) as

$$\vec{E}'_0 = T_A T_S T_R T_P \vec{E}_0, \quad (3.49)$$

where T_A, T_S, T_R, T_P represent the Jones matrices of the analyzer, the reflecting surface, the retarder, and the polarizer respectively. The relation (3.49) can be also presented as the evolution of the Jones matrix

$$\vec{J}' = T_A T_S T_R T_P \vec{J} T_A^\dagger T_S^\dagger T_R^\dagger T_P^\dagger \quad (3.50)$$

where \vec{J}' and \vec{J} are the coherency matrices of the light on the detector and on the polarizer correspondingly. To calculate the intensity on the detector, one should take the trace of J' or calculate $|E'_0|^2$ using (3.49). As the result, we will have intensity depending on the analyzer angle that makes possible to calculate reflective coefficients of the

material the sample is made of, and afterwards the dielectric function of this material at the frequency of the incident wave.

3.5 Muller matrix theory with imperfections

3.5.1 Definition of matrices

Consider the following system of optical elements: the incoming light with degree of polarization P_s and its polarization state (ψ_s, δ_s) ; the polarizer with fixed angle α_p , transmissions A_p, a_p and its imperfection $\chi_p = a_p/A_p$; the sample surface with parameters ψ and Δ and reflectivity A_s ; the compensator with retardation δ , transmission A_c and depolarization D ; and the analyzer with transmissions A_a , an imperfection $\chi_a = a_a/A_a$. Now, trace out the Muller matrices for these elements. So, the Muller matrix for rotator to the angle α has the form:

$$M_{rot} = \begin{pmatrix} 1 & 0 & 0 & 0 \\ 0 & \cos 2\alpha & \sin 2\alpha & 0 \\ 0 & -\sin 2\alpha & \cos 2\alpha & 0 \\ 0 & 0 & 0 & 1 \end{pmatrix}. \quad (3.50)$$

The Muller matrix for partial polarizer with maximum and minimum transmissions A and a , and oriented at the angle α [85]

$$M_{part} = \begin{pmatrix} A+a & A-a & 0 & 0 \\ A-a & A+a & 0 & 0 \\ 0 & 0 & 2\sqrt{Aa} & 0 \\ 0 & 0 & 0 & 2\sqrt{Aa} \end{pmatrix} \quad (3.51)$$

Thus, the total matrix for polarizer is $M_p = M_{rot}(\alpha_p)M_{par}(a_p, A_p)M_{rot}(-\alpha_p)$ and the similar matrix for the analyzer, with substituted $A_p \Leftrightarrow A_a, a_p \Leftrightarrow a_a, \alpha_p \Leftrightarrow \alpha_a$. The retarder unit is virtually broken to ideal retarder with retardation δ and to depolarizing element with depolarization D . Denote the degree of polarization after compensator as $P_c = 1 - D$. The matrix for ideal retarder has a form:

$$M_{ret} = \begin{pmatrix} 1 & 0 & 0 & 0 \\ 0 & 1 & 0 & 0 \\ 0 & 0 & \cos \delta & \sin \delta \\ 0 & 0 & -\sin \delta & \cos \delta \end{pmatrix}, \quad (3.52)$$

and the matrix of virtual depolarizing element

$$M_D = \begin{pmatrix} 1 & 0 & 0 & 0 \\ 0 & P_c & 0 & 0 \\ 0 & 0 & P_c & 0 \\ 0 & 0 & 0 & P_c \end{pmatrix}. \quad (3.53)$$

3.5.2 Intensity on the detector

Consider the evolution of the Stokes vector using the Muller matrices (3.50 – 3.53). The incoming light is generally characterized by the following Stokes vector

$$\vec{S}_0 = s_0 \begin{pmatrix} 1 - P_s \\ 0 \\ 0 \\ 0 \end{pmatrix} + s_0 P_s \begin{pmatrix} 1 \\ -\cos 2\psi_s \\ \sin 2\psi_s \cos \Delta_s \\ -\sin 2\psi_s \cos \Delta_s \end{pmatrix} \quad (3.54)$$

Then after polarizer we will have the vector $\vec{S}_1 = M_{pola} \times \vec{S}_0$, where $M_{pola} = M_{rot}(\alpha_p)M_{par}(a_p, A_p)M_{rot}(-\alpha_p)$. Then, after retarder we have $\vec{S}_2 = M_D \times M_{ret} \times \vec{S}_1$. Then, after the light has reflected upon the sample, its Stokes vector assumes the form $\vec{S}_s = M_{sam} \times \vec{S}_2$. Further, multiplying to the analyzer matrix $M_{anal} = M_{rot}(\alpha_a)M_{par}(a_a, A_a)M_{rot}(-\alpha_a)$, we obtain the Stokes vector characterizing the light on the detector. The next step is to extract the intensity of the wave as the first element of the Stokes vector. Expression of intensity [85]

$$I = I_0 (A + B \cos 2\alpha_a + C \sin 2\alpha_a) \quad (3.55)$$

where $I_0 = 1/4 A_{pol} A_{ret} A_{anal} \sqrt{r_x^2 + r_y^2}$ is the general pre-factor depending on the transmissions A_{pol} , A_{ret} , A_{anal} , reflection of a sample A_{sam} , and the incident light intensity s_0 . Coefficient A , B (structure of free terms A and B can be found in [129]), are dependent on polarizer angle, imperfections of polarizer and analyzer, depolarization and retardation of the compensator, and Ψ and Δ of the sample.

3.5.3 Sample as depolarizer of the light

Up to this point, it has been assumed that the sample does not depolarize the light beam, and that Eqs. (12) can be used to determine the sample Muller matrix from the simple Jones matrix. For many situations normally encountered in spectroscopic ellipsometry measurements, this is a good assumption. However, there are several situations, where the sample does depolarize the light beam. In this case, there is no rigorous connection between Jones matrix formalism and the Muller matrix formalism. Examples of sample depolarization:

- 1) nonuniform film thickness,
- 2) transparent substrate,
- 3) rough surface,
- 4) monochromator or spectrograph depolarization.

Even if the light beam is partially depolarized from the sample, it still possible to correct for these effects if the amount of depolarization is measured [85]. In this case, the measured sample Mueller matrix has additional elements

$$\vec{M} = \beta \vec{M}_J + (1 - \beta) \begin{pmatrix} 1 & 0 & 0 & 0 \\ 0 & 0 & 0 & 0 \\ 0 & 0 & 0 & 0 \\ 0 & 0 & 0 & 0 \end{pmatrix} \text{ and } \vec{M} = \begin{pmatrix} 1 & -N_m & 0 & 0 \\ -N_m & 1 & 0 & 0 \\ 0 & 0 & C_m & S_m \\ 0 & 0 & -S_m & C_m \end{pmatrix}, \quad (3.56)$$

where \vec{M}_J is the Mueller Jones matrix of the non-depolarizing samples and β - the fraction of polarized light in the light beam (then $\beta < 1$, if the sample depolarizes the incident light beam [130]), what is an expression of the associated ellipsometric parameters [131]

$$(N_m^2 + S_m^2 + C_m^2) = \beta^2. \quad (3.57)$$

The subscript m emphasizes that these quantities are measured, and therefore subject to random and systematic errors. Each of the parameters in this equation is given by integration over the distribution of the film thickness over the size of the spot. If the film thickness varies from H_1 to H_2 over the spot size, the parameter N_m will be given by

$$N_m = \int_{D_1}^{D_2} f(H)N(H)dH, \quad (3.58)$$

where $f(H)$ is the probability distribution function describing the film thickness variation

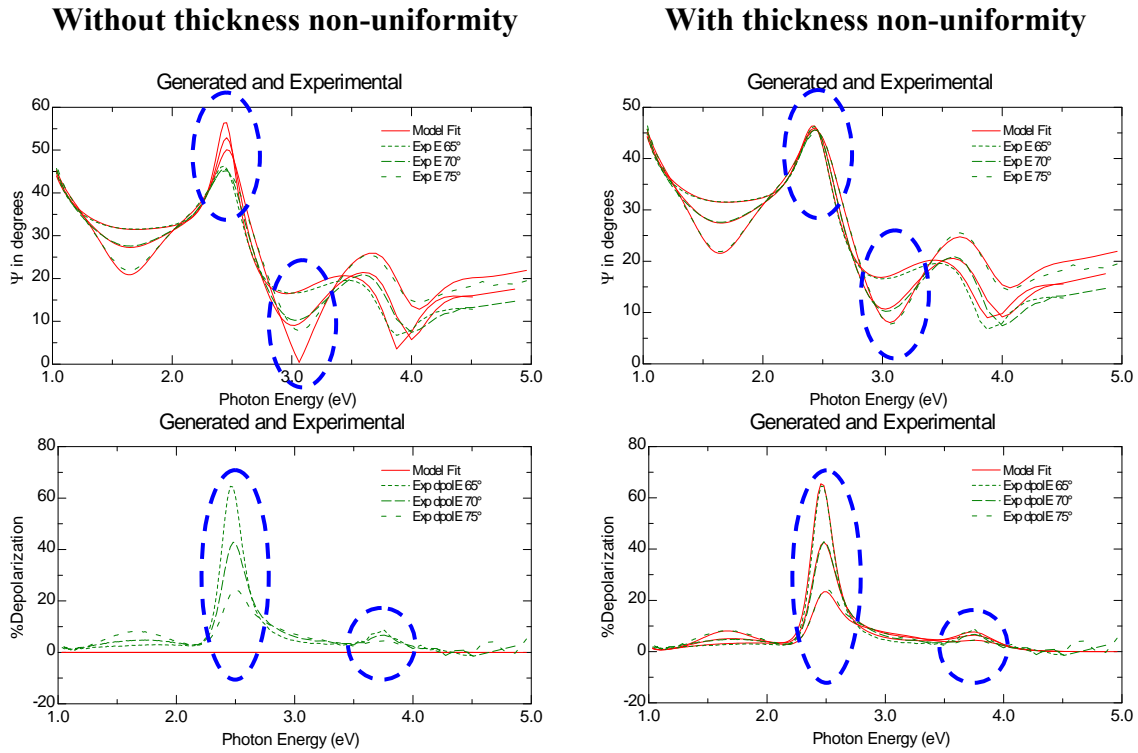


Fig. 3.7. Example of how depolarization of the sample affect the form of ψ and Δ . If the thickness non-uniformity is not taken into the model, bad agreement of fitted and experimentally established maximums and minimums of ψ and Δ and depolarization can be found. Depolarization measurements show that in this case thin film of $\text{SrBi}_2\text{Ta}_2\text{O}_9$ film (thickness 134 nm) strongly depolarize the light due to the thickness non-uniformity.

and $N(H) = \cos(2\psi(H))$. Similar expressions can be determined for S_m and C_m , considering that $S(H) = \sin(2\psi(H))\sin(\Delta(H))$ and $C(H) = \sin(2\psi(H))\cos(\Delta(H))$ [131]. During ellipsometric experiments not only main ellipsometric angles were evaluated, but also the depolarization of the film was measured that allowed us to establish amount of the thickness non-uniformity of the film.

In this work the light depolarization of the sample was measured. The depolarization was measured, using spectroscopic ellipsometer with auto-retarder. Example of how thickness non-uniformity affects the ψ and Δ , and depolarization values is shown in Fig. 3.7.

3.6 Dielectric function

Consider the complex refractive index as

$$\tilde{n} = n - ik \quad (3.59)$$

where n – refractive index, k – extinction coefficient, it can be written in a form of dielectric permittivity $\tilde{n} = n(1 - i\alpha) = \sqrt{\varepsilon}$ [125], where $\varepsilon = \varepsilon_1 - i\varepsilon_2$ - complex dielectric permittivity, and $\alpha = 4\pi k/\lambda$ - absorption coefficient. First, the dielectric permittivity is a response function, therefore

$$\varepsilon(-\omega) = \varepsilon^*(\omega) \quad (3.60)$$

Second, from the causality principle we have the Kramers-Kronig (KK) relations [85]

$$\varepsilon_1(\omega) - 1 = \frac{2}{\pi} P \int_0^{+\infty} \frac{x\varepsilon_2(x)}{x^2 - \omega^2} dx, \quad (3.61)$$

$$\varepsilon_2(\omega) = -\frac{2\omega}{\pi} P \int_0^{+\infty} \frac{\varepsilon_1(x) - 1}{x^2 - \omega^2} dx, \quad (3.62)$$

where P – is the symbol of the main quantity of the integral. For isotropic media $\tilde{n}^2 = \varepsilon(\omega)$, $n^2 - k^2 = \varepsilon_1(\omega)$, $2nk = \varepsilon_2(\omega)$, then KK can be written in

$$n^2(\omega) - k^2(\omega) - 1 = \frac{4}{\pi} P \int_0^{+\infty} \frac{xn(x)k(x)}{x^2 - \omega^2} dx, \quad (3.63)$$

$$n(\omega)k(\omega) = \frac{\omega}{\pi} P \int_0^{+\infty} \frac{n^2(x) - k^2(x) - 1}{x^2 - \omega^2} dx. \quad (3.64)$$

The combination of KK relations with physical arguments about the behavior of optical conducts us to the sum-rule expression.

3.6.1 Oscillator models for the dielectric function

One of the way of looking at the optical properties of materials is to consider the field re-radiated by the induced dipoles of the classical oscillators. Such classical oscillators are Lorentz oscillator, for example. In this model the dipole radiation field interferes with the incident field in such a way as to produce absorption or refraction. The Lorentz model assumed that an electron bound with the nucleus as a harmonic oscillator. By solving the equation of motions, distribution of the complex dielectric function can be found as $\tilde{\varepsilon}$ [85]

$$\tilde{\varepsilon} = \varepsilon_{\infty} \left(1 + \frac{A^2}{(E_c)^2 - E(E - iB)} \right). \quad (3.65)$$

The model fitting parameters ε_{∞} , E_c , E , B and A are in units of energy, and they are respectively: the high-frequency lattice dielectric constant, the centre energy of the oscillator, the photon energy, the vibration frequency (broadening) of the oscillator, and the amplitude (strength) of the oscillator. Lorentz oscillator was applied to describe optical properties of the substrate, ie., platinum Pt and strontium ruthenium oxide SrRuO₃ (SRO).

Unfortunately the Lorentz oscillator (LO) does not fit well the characteristics of the complex dielectric function at the near ultraviolet and ultraviolet (UV) regions for ferroelectrics and some semiconductors [132, 133]. LO functions were used to model molecular or lattice vibrations in the infrared [133], complex refractive index of

conductive oxides [134], metals [135], and ferroelectrics till the absorption edge [136]. LO is symmetric in shape, and the high and low energy sides of the function decrease at the same rate. It is because the low energy portions of the ε' curves are most strongly affected by the area under of the curve (area is proportional to $A \cdot B$), and the peak shifts to lower energies as broadening increases. As a result LO have long asymptotic tails away from the absorption peaks and can cause unacceptable absorption artifacts in transparent regions.

But Tauc-Lorentz [137] and Cody-Lorentz oscillator (TLO and CLO) as more flexible functions at the fundamental band gap E_g and higher energies in the UV, since these functions rapidly decrease to zero away from their center energy and do not have long asymptotic tails as LO which can result in unwanted absorption through the band gap and below. As the result the typical absorption of dielectrics due to the electrons transition from the valence band to the conductive band at high photon energies can be very well described. The subscript of TLO indicates that the model is based on the Tauc joint density of states (model follows a Tauc law $\varepsilon_2(E) \propto (E - E_g)^2 / E^2$) and the Lorentz oscillator: expression of the $\tilde{\varepsilon} = \varepsilon_1 + i\varepsilon_2$ by TLO is written below

$$\varepsilon_2 = \frac{1}{E} \frac{AE_c B(E_c - E_g)^2}{(E^2 - E_c^2)^2 + B^2 E^2}, \text{ if } E > E_g \quad (3.66)$$

$$\varepsilon_2 = 0, \text{ if } E < E_g. \quad (3.67)$$

The CLO assumes that $\varepsilon_2(E) \propto (E - E_g)^2$, as the result the expression of the $\tilde{\varepsilon} = \varepsilon_1 + i\varepsilon_2$ is

$$\varepsilon_{n2}(E) = \begin{cases} \frac{E_1}{E} \exp\left(\frac{E - E_{gn} - E_m}{E_{un}}\right); & 0 < E \leq E_{gn} + E_m \\ G(E)L(E) = \frac{(E - E_{gn})^2}{(E - E_{gn})^2 + E_{pn}^2} \cdot \frac{A_n E_{on} \Gamma_n E}{(E^2 - E_{on}^2)^2 + \Gamma_n E^2}; & E > E_{gn} + E_m \end{cases} \quad (3.68)$$

$$E_1 = E_m G(E)L(E).$$

The model fitting parameters: A_n – amplitude (strength) of each oscillator (eV), E_{mn} – centre energy of each oscillator (eV), B_{pn} – vibration frequency of each oscillator (eV) E_{gn} – band gap energy of each oscillator (eV), E_{pn} , E_m , E_{un} – characterize peak position and form of ε_2 , E – photon energy (eV). The real part of the dielectric function ε_1 for TLO and CLO is Kramers–Kronig integral [134], given by

$$\varepsilon_1 = \varepsilon_\infty + \frac{2}{\pi} P \int_{E_{gj}}^{\infty} \frac{\xi \varepsilon_2(\xi)}{\xi^2 - E^2} d\xi, \quad (3.69)$$

where the P stands for the Cauchy principal part of the integral. The TLO and CLO models were used to describe the NaNbO_3 and $\text{PbZr}_x\text{Ti}_{1-x}\text{O}_3$ thin films optical function in this work.

3.7 Effective approximation theory for the mixed media

When doing optical analysis, one frequently encounters mixtures of materials with unknown optical properties for the constituents. If the local variations of the optical properties are of a much smaller scale than the wavelength of the light, the mixture can be modeled as a continuum. The optical properties of the mixture can be calculated from the

optical properties of the constituents. For this purpose, the effective medium approximation (EMA) method was used [138]

$$\frac{\varepsilon_e - \varepsilon_h}{\varepsilon_e + y\varepsilon_h} = \sum_{i=1}^n f_i \frac{\varepsilon_i - \varepsilon_h}{\varepsilon_i + y\varepsilon_h}, \quad (3.70)$$

to describe the top layer and interphase between the film and the bottom electrode, where f_i and ε_i are the volume fractions and complex dielectric constant of material (component) i , ε_e and ε_h are the dielectric functions of the EMA (total system) and the host material, respectively. The quantity n is the number of components, which are mixed together to form the EMA material. The screening parameter or depolarization factor [85], is related to the parameter $y = \frac{1}{m} - 1$, where m is the screening factor ($0 \leq m \leq 1$). Screening factor

describes the microstructure of the mixtures: 1 corresponds to a flat disk, $1/3$ – to a spherical microstructure, and screening factor $1/2$ - to a columnar microstructure. The thickness of the top layer correlates with the root mean square (RMS) value of the surface roughness provided that the percentage of voids is set to 50% and the screening parameter is assumed to be 0.33.

3.8 Optical gradient

Depth profile of the optical properties was established by dividing the single layer by slices, and the shape of the grading profile was characterized using exponential (or simple graded model) variation (Fig. 3.8) of the refractive index versus film thickness [85]. If film has no gradient of the refractive n index, n changes linearly and, in case of the simple graded model, exponent is equal to 1.

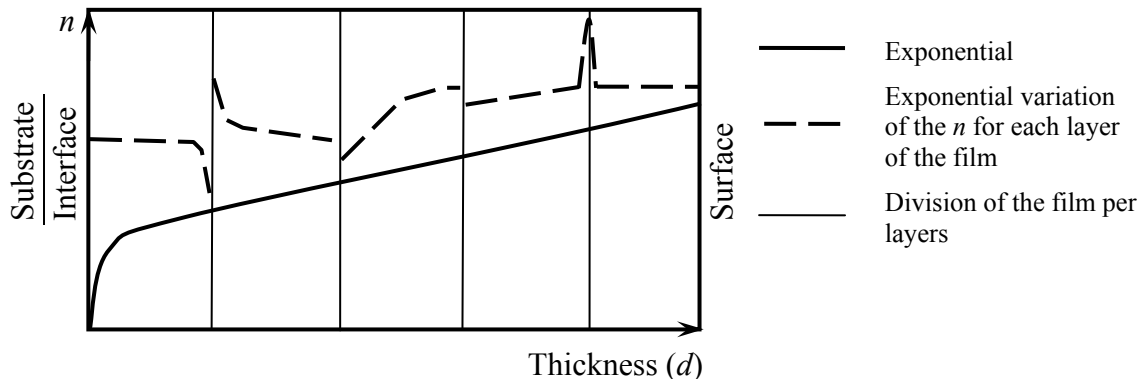


Fig. 3.8. The optical depth models applied to fit experimental SE data: continues line – exponential variation of n through the film, considering it as a one complete layer; discontinues liens - exponential variation of n at the each layer of the film. The different shapes of exponent were accomplished by changing the value of exponent and variation of the refractive index.

Variation of the refractive index from the substrate to the film surface is adjusted by exponent greater or smaller then 1. In this graded model the fitting parameters are value of exponent and variation of n . Optical gradient was calculated in the wavelength region of 500 – 1000 nm, where samples are not absorbing to minimize fitting parameters correlation caused artifacts.

3.9 Thermo-optics

The influence of structural phase transition (PT) on the temperature dependence of refractive index of transparent crystals [94] and thin films [30] are under intensive investigation. Structural phase transitions in crystals are primarily characterized by shifts of average positions of ionic nuclei, in respect of the displacive or of the order-disorder type of phase transition. As a secondary effect, they are accompanied by changes of the susceptibilities χ_{ij} in the optical region, and changes in the band gap energy. These reveal themselves as optical index ellipsoid rotation and/or as changes δn of refractive indices n . Measurements birefringence Δn give often the first information on the existence of a phase transition, on its (dis)continuity, and, together with the analysis of domains, on the point symmetry of both parent (PP) and distorted (DP) phases. But in addition, precise studies of these quantities are being repeatedly used to determine the temperature dependence of the order parameter q [94]. The anomalies in the refractive index can be detected due to its proportionality to the autocorrelation function of the fluctuating polarization $\langle \delta P^2 \rangle$ in the precursor region of ferroelectrics above T_c [96]:

$$\delta n(T) = -(n_0^3/2)(g_{11}^F + 2g_{12}^F) \langle \delta P^2(T) \rangle, \quad (3.80)$$

where g_{ij}^F are the free electro-optic coefficients and n_0 – unperturbed cubic refractive index. Similar relations hold for magnetic and soft-mode PT, inserting the respective order parameters and coupling constants instead of δP and g_{ij}^F [94]. Typically two contributions are usually considered. One comes from the thermal expansion. Another is to the dependence of dipole moment on ionic displacement [130], which is called electron-phonon interaction. Temperature change of refractive index in crystals without phase transitions can be written as [139, 140]

$$\eta = \eta_{TOE} + \eta_{VE} = \frac{dn}{dT} = \left(\frac{dn}{dT} \right)_{TOE} + \left(\frac{dn}{dT} \right)_{PE}, \quad (3.81)$$

where dn/dT – thermal coefficient of refractive index is considered to be as sum of contribution from thermo optical effect η_{TOE} and from photoelastic η_{PE} , connected with volume expansion (deformation). The proper thermo optical effect η_{TOE} is considered of three contributions – the first term is electronic polarizing power η_{TOE}^{EPP} [141], the second is caused by the temperature shift of absorption edge η_{TOE}^{TAE} [142, 143], and the third is phonon contribution η_{TEO}^{PH} , controlled by the fundamental phonon frequency ω_0 [130]. Taking into consideration analyses [142], the relation (3.81) can be written as

$$\eta = \eta_{TOE} + \eta_{VE} = \eta_{TOE}^{EPP} + \eta_{TOE}^{TAE} + \eta_{TOE}^{PH} + \eta_{PE}. \quad (3.82)$$

There are several ways how to express dn/dT . The non-linear behavior of the $dn(T)$ interpretation using microscopic parameters was reported by Shi-Yao Zhu [144], where contribution of the thermal expansion and electron-phonon interaction have been consider as

$$\frac{dn}{dT} = -\frac{n_0^2 - 1}{2n_0} \beta + \frac{1}{2n_0} \frac{dD_3}{dT}, \quad (3.83)$$

where β - volume expansion coefficient, D_3 - corresponding quantity for the crystal and refracts the response of the electrons interacting with the phonons to the light field. This relation was found by solving total Hamiltonian for the medium

$$H = H_{el} + H_{ph} + H_{el-l} + H_{ph-l} + H_{ph-e}, \quad (3.84)$$

where five Hamiltonians represents electrons, phonons, interaction of light field with the electrons and ions, and interaction between phonons and electrons. From the polarization of the medium

$$P(z) = m_0 A \left\langle \left\langle p(l=z) \right\rangle \right\rangle, \quad (3.85)$$

where m_0 – the cell number density and A means statistical average of x over a small volume location at z , whose dimension is much less than the wavelength of the light but much larger than dimension of the cell, the refractive index of the media was obtained and concluded in the formula (3.83). This relation showed that thermo optical coefficient is proportional to the T^3 at low temperatures, and it is linear [96] or constant [144] at the high temperatures. In this work drastical deviation from these concepts are reported due to the analysis of $n(T)$ at the PT. The main ellipsometric angles were measured at the selected wavelengths with increase and decrease of the temperature. Because of the high sensitivity of ellipsometric technique to any global and local structural changes, we cannot separate the phase transition taking place in whole films with surface or interface phase transition, and due to that we may observe PT at different temperatures from those detected for single crystals, for example, and we may observe nonlinear behavior of n at the high temperatures as well.

Deviations from these $n(T)$ concepts was reported also in other works [30, 96], what is attributed to the non-linearity of $n(T)$ to the influence of the temperature dependent ferroelectric soft-mode $\omega_s(T)$.

What contributions are on the optical band gap energy E_g with change of the temperature? The temperature dependence of the optical gap at a constant pressure $\Delta E_g(T)$ is mainly considered as a sum of two contributions

$$\Delta E_g(T) = \Delta E_g(T)_{ph} + \Delta E_g(T)_{exp}, \quad (3.86)$$

where $\Delta E_g(T)_{ph}$ is the phonon term (interprets the thermal disorder), and $\Delta E_g(T)_{exp}$ is the thermal expansion term. In the first approximation we can neglect the second term contribution (its magnitude is $\sim 20\%$ of the $\Delta E_g(T)$ value), assuming the temperature dependence of E_g is controlled mainly by the phonon term and as the result we can find [145]

$$E_g(T) = E_g(0) - A / [\exp(\hbar\omega_{ph} / k_B T) - 1], \quad (3.87)$$

where $E_g(0)$ is the optical gap at $T = 0$ K, A is a material constant (the sum of two contributions: (i) an intrinsic constant volume and (ii) thermal expansion), $\hbar\omega_{ph}$ is a mean phonon frequency, and k_B is Boltzmann constant. To fit our experimental $E_g(T)$ we were using Varshni quadratic relation [146], which can be found by simplifying the second term in (3.87) by expansion of

$$\exp(\hbar\omega_{ph} / k_B T) = \sum_{k=0}^{k=\infty} (\hbar\omega_{ph} / k_B T)^k / k! \quad (3.88)$$

given in ref. [147]. If $k = 1$, we get widely used linear relation of

$$E_g(T) = E_g(0) - A k_B T / \hbar\omega_{ph}, \quad (3.89)$$

if $k = 2$, we obtain Varshni quadratic relation

$$E_g(T) = E_g(0) - 2A(k_B T / \hbar\omega_{ph})^2. \quad (3.90)$$

Insomuch as linear relation of $E_g(T)$ gave higher $E_g(0)$ value as it should be from experimental $E_g(T)$, we were choosing Varshni quadratic relation.

But unfortunately the clear theory describing thermo-optical effects in FE at PT are still not established due to the complex process involved from the internal contribution of the expansion of the marital, change of the geometrical form, elasto-optical contribution, and electron-phonon interaction. The one of the problems is also to understanding the

sine of the thermo-optical coefficients, which differs for different material and the experimental evaluation of this phenomena is determinant.

4. Experiment and calculation methods used in this work

4.1 Experiment

Ferroelectric thin films were made by PLD and sol-gel techniques (see the details in chapter “5. Samples”), and were studied by XRD, Raman spectroscopy, dielectric spectroscopy, spectral ellipsometry, null-ellipsometry, reflectometry and atomic force microscopy (AFM).

XRD

The crystal structure of the NN films was analyzed by x-ray diffraction (XRD) using Siemens D5000 x-ray diffractometer (Fig. 4.1.) with Co anode material (radiation wavelength $\lambda(\text{CoK}\alpha_1) = 1.78897 \text{ \AA}$, $\lambda(\text{CoK}\alpha_2) = 1.79285 \text{ \AA}$). The samples were scanned over the 20 till 90 degrees with the step of 0.05 degree. The XRD experiments were done in co-operation with Solid States and Material Research in Dresden (Germany). The orientation of PZT film was determined by the Siemens D5005 diffractometer at the Cranfield University using CuK α radiation and a Goebel mirror. The XRD data were analyzed at the Institute of Solid State Physics in Riga (Latvia) by Dr. phys. Anatolij Misnev.



Fig. 4.1. Siemens D5000 x-ray diffractometer.

Raman spectroscopy

The RENISHAW micro Raman spectrometer (Fig. 4.2) was used for Raman spectroscopy experiments. The Raman spectrum was detected in the temperature range 80 - 573 K and in the frequency ranges 200 cm^{-1} - 1100 cm^{-1} . The light source was Ar laser (wavelength 514.5 nm), manufacturer Spectra Physics, and power $\sim 10 \text{ mW}$, focused at a spot of $2 \text{ }\mu\text{m}$ in diameter. Standard Notch filters supplied by



Fig. 4.2. RENISHAW micro Raman spectrometer.



Fig. 4.3. Dielectric spectroscopy set up of frequency and temperature dependencies measurements.

Renishaw company (manufactured by Kaiser) was used with an extra monochromator (Renishaw calls it NEXT filter) to block the laser line; it enables measurements down to $\sim 10 \text{ cm}^{-1}$ at the penalty of lower signal throughput. The Raman experiments were done at the Institute of Physics, Academy of Science in Prague (Czech Republic).

Dielectric spectroscopy

The dielectric properties of the films were investigated in a frequency range from 20 Hz to 250 kHz and at

temperatures from 290 K up to 620 K at 10 mV by a probe station with a bridge HP4284A (Fig. 4.3.). The dielectric spectroscopy experiments were performed at the Institute of Solid State Physics, University of Latvia, in Riga (Latvia).

Spectroscopic ellipsometry

1. Null-ellipsometry

In this work to detect the thin film thickness and optical properties with the very high precision at the wavelength $\lambda = 632.8$ nm were performed with variable-angle null-ellipsometer (angles set from 45° to 75° , step 5°). The null-ellipsometric experiments were performed by JĀM - 3M ellipsometer at the Institute of Solid State Physics, University of Latvia, in Riga (Latvia).

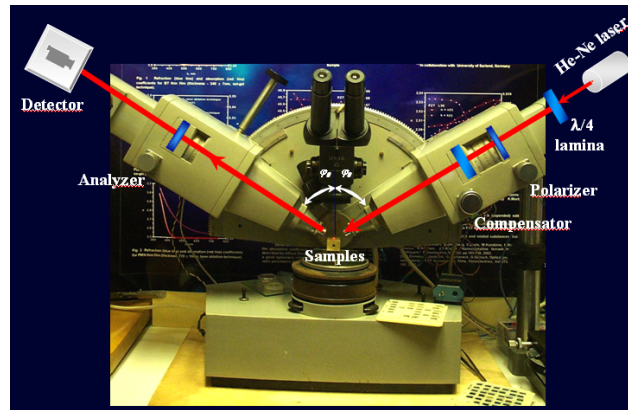


Fig. 4.4. Variable-angle null-ellipsometer JĀM - 3M.

2. Rotating analyzer ellipsometry

The optical measurements at the wide spectral range were performed by means of a J. A. Woollam spectroscopic ellipsometer (Fig. 4.5) operating in rotating analyzer mode. The main ellipsometric angles ψ and Δ were measured in a spectral range from 250 to 1000 nm (1.23 eV till 4.85 eV) at incidence angles of 65, 70 and 75 degrees

Specially constructed sample holder with PC-controlled heating element allowed the real-time measurements of ψ and Δ during heating. These measurements were performed in the temperature range 25 - 550°C at 300 and 400 nm wavelengths and at the incidence angle of 75 degrees. The given wavelength was chosen because of its near band gap position with purpose to increase the sensitivity of ellipsometric measurements to any phase transitions and structural changes in our films. Near the absorption edge, any structural changes give a considerable contribution to the interband transitions witch can be seen in the refraction and absorption indices changing [18]. Low temperature measurements were performed with the Janis liquid helium cryostat at the incidence angle of 70 degrees.

To have the option to measure the temperature dependence of the dielectric constants one also has to incorporate a cryostat into the ellipsometer. This requires the use of optical windows that are located in between the polarizer and analyzer. The properties of these windows are rather crucial since they can give rise to rather large errors in the ellipsometric measurements. Because special calibration was done before the low temperature measurements were performed. Spectroscopic ellipsometry experiments were done at the Institute of Physics, Academy of Science in Prague (Czech Republic).

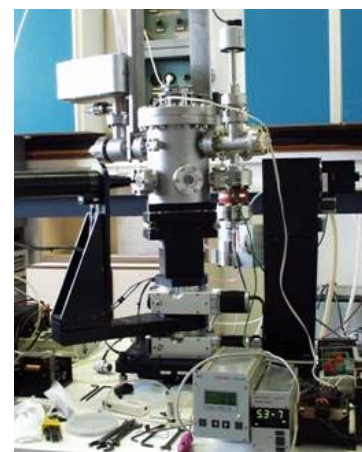


Fig. 4.5. J. A. Woollam spectroscopic ellipsometer with Jaanis crvostat.

The principles of ellipsometry can be found in chapter “3. Reflectometry and ellipsometry”.

Reflectometry

A miniature “Ocean Optics” CCD spectrometer, model PC 1000, designed as a plug-in PC ISA slot with fiber optics input was used for the reflectivity measurements under normal light incidence geometry in the spectral range of 350 –750 nm (Fig. 4.6) un this work. This technique gave an advantage very quickly evaluate approximate thickness and optical properties of the films.

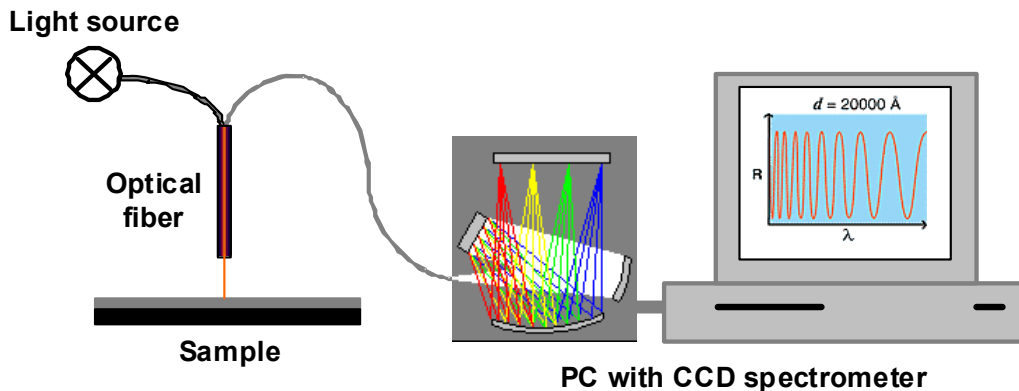


Fig. 4.6. Illustrative scheme of reflectometry set as a fiber optic input under normal light incidence geometry.

Reflectometry measurements were performed at the Institute of Solid State Physics, University of Latvia, in Riga (Latvia). Experience on nul-ellipsometry and reflectometry were acquired during development of the bachelor’s work [38b] and master’s work [39c]. The basic idea and main results are presented in [39d].

AFM

The surface morphology was examined using AFM. For AFM measurements a Stand Alone SMENA microscope (NT-MDT Co.; Fig. 4.7) was employed in a contact mode using conventional silicon tips (spring constant ~30 N/m, resonance frequency ~350 kHz). The deflection set point was - 0.5, the s-point parameter of probe and surface interaction, maintained via feedback during the scanning, was zero amperes, with the integrator gain coefficient included in the general feedback loop coefficient being 1.5 nA. The scanned area was varied from (10×10) to (0.5×0.5) μm, with the scanning rate 0.8–1 Hz.



Fig. 4.7. a Stand Alone SMENA AFM microscope.

4.2 Simulation and fitting of spectroscopic ellipsometric data

To be able to simulate the ψ and Δ spectra obtained in spectroscopic ellipsometry, the impedance formalism for stacks of layers (multilayer Matrix model together with Fresnel formulas [85]) is combined with the description for the refractive index by oscillators (see chapter “3. Reflectometry and ellipsometry”). The implementation of this spectroscopic ellipsometry model has the following main features:

- 1) A layer system is defined as a semi infinite substrate, an arbitrary number of layers of arbitrary thickness, and a semi infinite ambient;
- 2) For each layer material, including substrate and ambient material, the complex refractive index can be defined a series of values read from a file, or a series of harmonic oscillators added to a fixed background;
- 3) Simulations and fits can be done as a function of wavelength, angle of incidence, temperature or thickness of one or several of the constituting layers;
- 4) the thickness, and fitting parameter of each oscillator (the central wave number, width, and strength) are determined by minimizing the sum of squares of differences between measured and calculated values;
- 5) Any fit parameter can be fixed or made variable during the minimization procedure.

Dielectric function was described with Lorentz oscillator [85] for the conductive materials (Pt, SrRuO₃), Tauc-Lorentz oscillator [137], and Cody-Lorentz oscillator [85] for the ferroelectric materials, in this case – NN and PZT. The interface layer between bottom electrode and the film, and surface layer of the film was modeled as effective medium approximation (EMA) [138].

First of all the SE measurements were made on substrates of the film to evaluate the optical properties of the Pt and SrRuO₃. Afterwards the thin films were analyzed by SE. The steps of calculations:

- 1) Complex refractive index of the host material and thickness of the film were evaluated by fitting simple model the experimental data;

Typically ψ and Δ spectra exhibit oscillations at the lower energies because of the interference among multiple-reflected beams in the thin film, if the film is transparent. The frequency of oscillations depends on the thickness of the film: basically, the thicker the film is, the higher the frequency. From the amount and amplitudes of the maxims and minims of ψ and Δ spectra, the one can evaluate the thickness and optical properties [85]. The fitting parameters are film thickness and parameters of the oscillator of the dielectric function.

- 2) From the simple model fit one can see whether the film has thickness nonuniformity and roughness; if there is a significant difference in the amplitude of the calculated ψ and Δ in comparison with the measured one then it is an indication of thickness nonuniformity of the film [85, 130, 131];

The thickness distribution of the thin film rise depolarization of the light, which can be seen as the rounded shape of minima and maxima in Δ (since Δ is very sensitive to the thickness, [85]). The fitting parameter is the thickness nonuniformity, what can be evaluated from the additional depolarization measurements of the sample by SE.

- 3) If the calculated ψ and Δ have higher or lower values in comparison with experimental ψ and Δ at the visible, near UV and UV region, then it is an indication of the surface roughness;

Ignorance of the surface layer in the model results in unphysical absorption artifacts in the measured optical constants, namely significant absorption in the transparent spectral range below the band gap [85]. Adding surface roughness to the model completely

eliminates these artifacts. This demonstrates the sensitivity of spectroscopic ellipsometry to the surface microstructure and the need to include surface effects in the analysis model. So, from these specifics of ψ and Δ in (2) and (3) one can know is it necessary to make the model more complicated, by estimating thickness nonuniformity and the roughness. Additional layer as EMA can be added into the model between film and the ambient. The fitting parameter is the thickness of this layer.

- 4) If after considering the film to be with the roughness, the fit of the ψ and Δ at the visible, near UV and UV region is still not satisfactory (calculated ψ and Δ is higher or lower than experimentally detected), then peculiar it is indication of the interface existence between bottom electrode and the film; additional layer as a EMA can be added into the model between bottom electrode and the film. The fitting parameter is the thickness of this layer.
- 5) If the fit is still not satisfactory, then it is the indication about film inhomogeneity such as porosity and depth profile. Typically whole calculated spectra is slightly higher/lower than experimentally detected; peculiar in the case of a graded optical properties of the film, curved shape of experimentally detected minima of ψ and Δ are much more bended and deformed.

The porosity of the film can be modeled as a EMA model, where film is a mixture of the host material and the voids. The fitting parameters then are thickness of the film and a volume fraction of the voids.

Depth profile of the optical properties can be described by dividing the single layer by slices, and the shape of the grading profile can be characterized using exponential (or simple graded model) variation (see chapter “3.8 Optical gradient”) of the refractive index versus film thickness [85]. If film has no gradient of the refractive n index, n is constant with the thickness, and, exponent is equal to 1. Variation of the refractive index from the substrate to the film surface is adjusted by exponent greater or smaller than 1. The fitting parameters are value of exponent and variation of n . Optical gradient was calculated in the wavelength region of 500-1000 nm, where film is not absorbing to minimize fitting parameters correlation caused artifacts.

In calculations of this work the optical properties of the host material of the NN and PZT thin film were considered to be isotropic. This consideration comes from the XRD analysis of these films and from the polarization measurements of the reflected light from the films with SE. The XRD results showed that NN is polycrystalline with the (see chapter “6.1.1 XRD”) orthorhombic orientation of the crystallites on both substrates Si/SRO and Pt/SRO. If thin film is polycrystalline, then it is satisfactory to consider the film as isotropic due to the impossibility to separate that reflected ψ and Δ spectrum from the randomly oriented crystallites which contain information about anisotropic complex refractive indexes. The isotropy of the NN films was also approved by the polarization measurement of the reflected light by the films by null-ellipsometry and SE.

The XRD of PZT showed that samples mainly have (111) or (100) plain oriented parallel to the substrate surface (see chapter “6.2.1 XRD”). Some films contain mixed phases of (111) and (200) as well as (110) and (112). That means during fit of SpE data the films might be considered as a mixture of two materials (EMA), with different optical properties, due to the different phases. The PZT 52/48 is in a ferroelectric, tetragonal phase and it should be considered correctly as a one-axial anisotropic medium. Analysis of reflected light with different polarization showed that PZT film has negligibly small anisotropy and it can be neglected during data model. This may be due to existence of additional phases in PZT or due to SE weak sensitivity to the transverse anisotropy and small difference of refractive indexes $\Delta n < 0.015$. The weak sensitivity may be explained by the high value of PZT refractive index $n > 2.45$. Independently of the angle of

incidence, a light beam propagates almost along the film's normal after refraction: the larger refractive index of the film, the closer light goes to the normal. In this case this gives low sensitivity to the extraordinary component; so, even the biggest possible difference between the indexes ($\Delta n > 0.015$) may be disregarded almost without influence on the results.

The optimal values for the refractive index n , extinction coefficient k , thickness d , thickness non-uniformity, interface roughness, optical gradient, and temperature dependence of optical band gap E_g and refractive index were found by the mean square procedure for all model minimization, using the software packages ThinFilmWizard and WVASE32.

5. Samples

5.1 Sodium niobate oxide NaNbO_3

Sodium niobate NaNbO_3 (NN) thin film heterostructures were deposited by pulsed laser deposition technique PLD* on $\text{Si}((100), 300 \mu\text{m})/\text{SiO}_2(1000 \text{ nm})/\text{Ti}(10 \text{ nm})/\text{Pt}((111), 100 \text{ nm})/\text{SrRuO}_3(\sim 30 \text{ nm})$ (Fig. 5.1a), and Si/SrRuO_3 (Fig. 5.1b) substrates using KrF-excimer laser (LPX 300, Lambda Physics; wavelength 248 nm) with the repetition rate of 10 s^{-1} and energy density of $2 - 3 \text{ J/cm}^2$. PLD thin films samples were specially made of trapezium shape to study thickness dependence of optical properties. All samples are summarized in the Tab. 5.1.

PLD process was accomplished in the vacuum chamber with Ar/O_2 atmosphere at the pressure of 0.03 mbar. The laser beam was focused on the wobbling and rotating target material to minimize the droplet formation. The deposition temperature T_d for NN and SRO was 580°C .

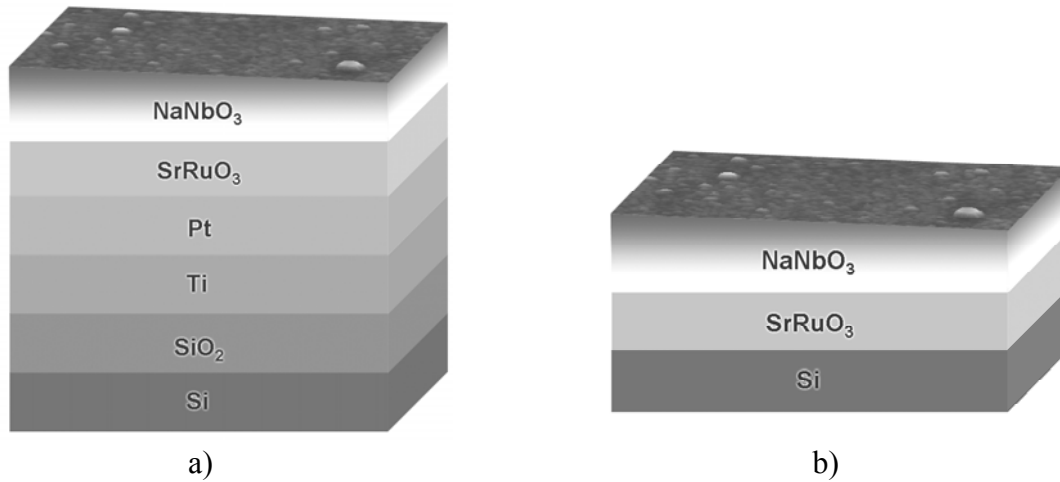


Fig. 5.1. Illustrative pictures of the multilayer structure of the NN thin film on a) $\text{Si}/\text{SiO}_2/\text{Ti}/\text{Pt}/\text{SrRuO}_3$ and b) Si/SrRuO_3 substrates. In direction from the bottom to the top: Silicon Si, Silicon dioxide SiO_2 , titanium Ti, platinum Pt, strontium ruthenium oxide SrRuO_3 , NN thin film with different thickness (trapezium shape) and a top layer of the surface roughness.

The thin Ti layers were grown by a thermal evaporation process at a temperature of 1170 K. Platinum bottom and top electrodes were sputtered by the e-beam method, keeping the substrate temperature around 470 K. The targets of the NN and SRO were made by chemical synthesis technique [148].

The highly conductive oxide SrRuO_3 have been used as the bottom electrode due to its stability, not only in oxidizing, but also in inert gas atmospheres up to quite high temperatures [149–151], unlike the high- T_c superconducting thin films, which typically have relatively poor crystalline quality and rough surfaces, and are not fully chemically and thermally stable. High stability of the bottom electrode and processing compatibility with ultra-large-scale integrated circuit fabrication during electrode deposition are very important to realize the integration between the high-permittivity dielectric materials and active devices located on the substrates.

* In cooperation with Institute for Solid State and Materials Research Dresden (Dresden, Germany).

Tab. 5.1. List of the samples: composition, substrate, deposition temperature T_d , pressure P , laser repetition rate (count), laser voltage V , laser intensity and frequency f .

No	Composition	Substrate	T_d (°C)	P (mbar)	Count ($\cdot 1000$)	V (kV)	Intensity (mJ)	f (Hz)
P637B	NaNbO ₃	Si(300 μ m)/SiO ₂ (1000nm)/Ti(10nm)/Pt(100nm)/SrRuO ₃	580 - 570	0.3	4000	22	403	4
P637D	NaNbO ₃	Si(300 μ m)/ SrRuO ₃	580 - 570	0.3	4000	22	403	4
P637A	NaNbO ₃	Si(300 μ m)/SiO ₂ (1000nm)/Ti(10nm)/Pt(100nm)/SrRuO ₃	580 - 570	0.3	4000	22	403	4
P637C	NaNbO ₃	Si(300 μ m)/SiO ₂ (1000nm)/Ti(10nm)/Pt(100nm)/SrRuO ₃	580 - 570	0.3	4000	22	403	4
W551	-	Si(300 μ m)/SiO ₂ (1000nm)/Ti(10nm)/Pt(100nm)						
P626B	-	Si(300 μ m)/SiO ₂ (1000nm)/Ti(10nm)/Pt(100nm)/SrRuO ₃	650	0.3	1000	20	300	4

5.1.1 Pulsed laser deposition

Pulsed laser deposition (PLD) technique involves all the physical processes of laser-material interaction during the impact of the high-power pulsed radiation on a solid target, as well as a formation of the plasma plume with high energetic species, the subsequent transfer of the ablated material through the plasma plume onto the heated substrate surface and the final film growth process. Generally the PLD (Fig. 5.2) can be

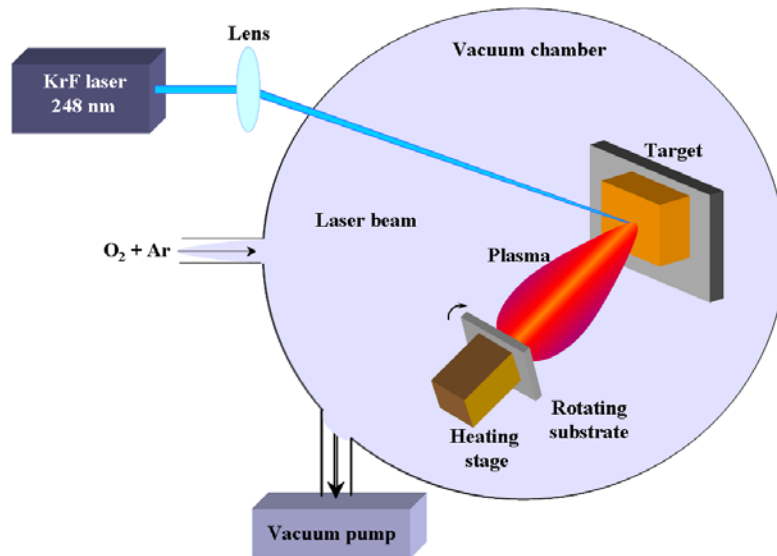


Fig. 5.2. Schematic diagram of PLD.

divided into the following four stages:

1. Laser radiation interaction with the target,
2. Dynamic of the ablation materials,
3. Deposition of the ablation materials on the substrate,
4. Nucleation and growth of a thin film on the substrate surface.

1. The laser beam is focused onto the surface of the target. At sufficiently high energy densities and short pulse duration, all elements in the target surface are rapidly heated up to their evaporation temperature. Materials are dissociated from the target and ablated out with stoichiometry as in the target. The instantaneous ablation rate is highly dependent on the fluencies of the laser irradiating on the target. The ablation mechanisms involve many

complex physical phenomena such as collisional, thermal, and electronic excitation, exfoliation and hydrodynamics.

2. The emitted materials tend to move towards the substrate according to the laws of gas-dynamic and show the forward peaking phenomenon [152]. The spatial thickness varies as a function of $\cos^n q$, where $n \gg 1$ [153]. The laser spot size and the plasma temperature have significant effects on the deposited film uniformity. The target-to-substrate distance is another parameter that governs the angular spread of the ablated materials. A mask placed close to the substrate can reduce the spreading [154].

3. The ejected high-energy species impinge onto the substrate surface and may induce various type of damage to the substrate. The mechanism of the interaction is illustrated in the Fig. 5.3. These energetic species sputter some of the surface atoms and a collision region is established between the incident flow and the sputtered atoms. Film grows immediately after this thermalized region (collision region) is formed. The region serves as a source for condensation of particles. When the condensation rate is higher than the rate of particles supplied by the sputtering, thermal equilibrium condition can be reached quickly and film grows on the substrate surface at the expenses of the direct flow of the ablation particles.

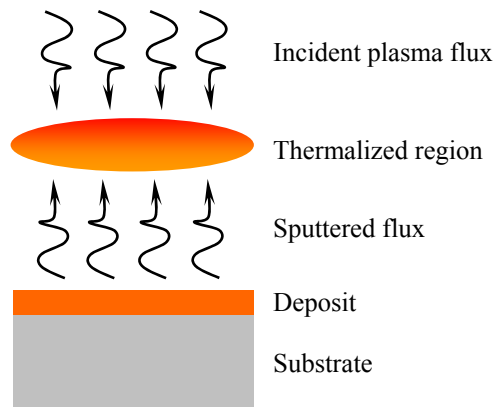


Fig. 5.3. Schematic diagram of the plasma-substrate interaction

4. Nucleation-and-growth of crystalline films depends on many factors such as the density, energy, degree of ionization, and the type of the condensing material, as well as the temperature and the physical-chemical properties of the substrate. The two main thermodynamic parameters for the growth mechanism are the substrate temperature T and the supersaturation D_m . They can be related by the following equation

$$D_m = kT \ln(R/R_e),$$

where k is the Boltzmann constant, R is the actual deposition rate, and R_e is the equilibrium value at the temperature T .

The nucleation process depends on the interfacial energies between the three phases present - substrate, the condensing material and the vapor. The minimum-energy shape of a nucleus is like a cap. The critical size of the nucleus depends on the driving force, i.e. the deposition rate and the substrate temperature. For the large nuclei, a characteristic of small supersaturation, they create isolate patches (islands) of the film on the substrates, which subsequently grow and coalesce together. As the supersaturation increases, the critical nucleus shrinks until its height reaches an atomic diameter and its shape is that of a two-dimensional layer. For large supersaturation, the layer-by-layer nucleation will happen for incompletely wetted foreign substrates.

The crystalline film growth depends on the surface mobility of the adatom (vapour atoms). Normally, the adatom will diffuse through several atomic distances before sticking to a stable position within the newly formed film. The surface temperature of the substrate determines the adatom's surface diffusion ability. High temperature favors rapid and defect free crystal growth, whereas low temperature or large supersaturation crystal growth may be overwhelmed by energetic particle impingement, resulting in disordered or even amorphous structures.

The N_{99} , the mean thickness at which the growing [155, 156], thin and discontinuous film reaching continuity is given by the formula

$$N_{99} = A(1/R)^{1/3} \exp(-1/T),$$

where R is the deposition rate (supersaturation related) and T is the temperature of the substrate and A is a constant related to the materials.

In the PLD process, due to the short laser pulsed duration (~10 ns) and the small temporal spread (< 10 μs) of the ablated materials, the deposition rate can be enormous (~10 μm/s). Consequently a layer-by-layer nucleation is favored and ultra-thin and smooth film can be produced. In addition the rapid deposition of the energetic ablation species helps to raise the substrate surface temperature. In this respect PLD tends to demand a lower substrate temperature for crystalline film growth.

5.2 Lead zirconium titanium Pb(Zr,Ti)O₃

Lead zirconium titanium oxide PbZr_xTi_{1-x}O₃, where x = 30, 52 and 95 (PZT 30/70, 52/48 and 95/05) were made by sol-gel* technique using two different solvent systems: a mixture of acetic acid and methanol (AcOH/MeOH) or 2-Methoxyethanol (2-MEO). The AcOH/MeOH preparation route was reported earlier in Ref. [157]. To prepare the 2-MEO based sol the route reported in Ref. [20] was applied. The concentrations of both sol systems were adjusted to 0.4M. The PZT films using either sol were spin coated onto platinised silicon substrates at 4000 rpm for 30 seconds. To crystallize the films two different thermal profiles were applied; all layers crystallized together (LCT) at the same time, and each layer crystallized individually (LCI). The first profile employed the deposition of one layer followed by drying at 300°C for 1 minute. When the final layer was deposited the sample was placed on the hotplate for 35 minutes at 550°C to crystallize. The second thermal profile involved individual crystallization of each layer by holding the sample for 1 minute at 300°C followed by 550°C for 5 minutes before the next layer was coated. The annealing time was sufficient for all films to crystallize. With either thermal profile or sol a series of 5 films was made having 1 to 5 layers. The films were fabricated by applying sols onto Si(100)/SiO₂(500 nm)/Ti(5nm)/Pt((111), 100nm) by spin coating with a photo resist spinner (Model 1-EC101D-R790, Headway Research Inc).

Totally 29 samples were analyzed by ellipsometry. The list of the samples is summarized in Tab. 5.2. Samples made at the same conditions, but having different amount of layers, are grouped under the same number. The samples, which layers were annealed at the different temperatures were also prepared, as well as samples with the specially made composition gradient.

* In cooperation with Cranfield University, SIMS, Cranfield, United Kingdom

Tab. 5.2. Sample composition, sol-gel solvent, the way of crystallization of the films (LCT or LCI), amount of layers and annealing temperature of the PZT films. The samples, where optical gradient was found, are collared in yellow.

Nr	Composition	Solvent	Crystallization	Total layers	Annealing
1	Compositional gradient sample Layer 1 and 2: PZT 30/70, 1 layer 90 nm or 45 nm /layer Layer 3 and 4: PZT 52/48, 150 nm/layer Layer 5 and 6: PZT 95/05, 160 nm/layer	AcOH/MeOH	LCT	6	550°C: 5 min
2	Different annealing temperatures PZT 30/70	AcOH/MeOH	LCT	3 ~ 71 nm/layer	Layer 1: 550°C, 30 min Layer 2: 510°C, 30 min Layer 3: 450°C, 30 min?
3	Different annealing temperatures PZT 52/48	AcOH/MeOH	LCT	3 128 nm/layer	Layer 1: 550°C, 30 min Layer 2: 510°C, 30 min Layer 3: 450°C, 30 min?
4	5 samples PZT 52/48	AcOH/MeOH	LCT	1 – 5 100 nm/layer	550°: 35 min
5	5 samples PZT 52/48	AcOH/MeOH	LCI	1 – 5 ~ 110 nm/layer	550°: 5 min
6	4 samples PZT 52/48 Thick films	AcOH/MeOH	LCT	1-4 ~ 205 nm/layer	550°: 5 min
7	5 samples PZT 52/48	2-MEO	LCT	1- 5 68 nm/layer	550°: 35 min
8	5 samples PZT 52/48	2-MEO	LCI	1- 5 65 nm/layer	550°: 5 min Final 550°C for 30 min
9	PZT 30/70	AcOH/MeOH	LCT	1 1 layer/68 nm	550°: 5 min
10	PZT 95/05	AcOH/MeOH	LCT	1 1 layer/95nm	550°: 5 min

5.2.1 Sol-gel technique

The sol-gel process is a wet-chemical technique (Chemical Solution Deposition) for the fabrication of materials starting either from a chemical solution (*sol* short for solution) or colloidal particles (*sol* for nanoscale particle) to produce an integrated network (*gel*) [158]. In the sol-gel process, molecular precursors are converted into nanometer-sized particles to form a colloidal suspension, or sol. The colloidal nanoparticles are then linked with one another in a 3D, liquid-filled solid network. This transformation to a gel can be initiated in several ways, but the most convenient approach is to change the pH of the reaction solution.

The drying process serves to remove the liquid phase from the gel thus forming a porous material, then a thermal treatment (firing) may be performed in order to favor further polycondensation and enhance mechanical properties (Fig. 5.4). But the method used to remove liquid from a solid will affect the sol-gel's properties. For example, to preserve a gel's original 3D structure and produce low-density aerogels, supercritical drying are used. If, instead, the gel is dried slowly in a fluid-evaporation process, the gel's structural network collapses, which creates a high-density material known as a xerogel.

The precursor sol can be either deposited on a substrate to form a film (e.g. by dip-coating or spin-coating), cast into a suitable container with the desired shape (e.g. to obtain a monolithic ceramics, glasses, fibers, membranes, aerogels), or used to synthesize powders (e.g. microspheres, nanospheres). The sol-gel approach is interesting in that it is a cheap and low-temperature technique that allows for the fine control on the product's chemical composition, as even small quantities of dopants, such as organic dyes and rare earth metals, can be introduced in the sol and end up in the final product finely dispersed. It can be used in ceramics manufacturing processes, as an investment casting material, or as a means of producing very thin films of metal oxides for various purposes. Sol-gel

derived materials have diverse applications in optics, electronics, energy, space, (bio)sensors, medicine (e.g. controlled drug release) and separation (e.g. chromatography) technology.

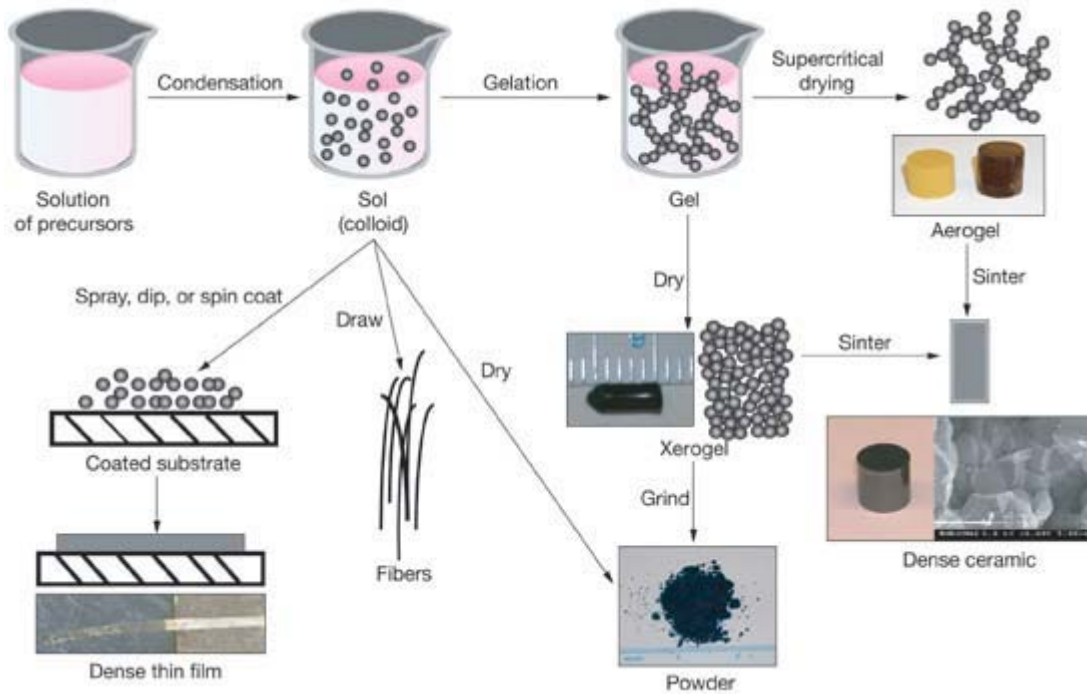


Fig. 5.4. The illustrative scheme of the sol-gel process.

6. Results

6.1 Sodium niobate NaNbO_3

6.1.1 XRD

The XRD patterns show that NN has orthorhombic (space group $P21ma$, space group number 26) polycrystalline structure (Fig. 6.1.1) on both substrates Si/SRO and Pt/SRO, what corresponds with the work of [12]. The full width of the half maxima of the peak at 26.55° is just 0.208° : the sizes of the crystallites are not smaller than 100 nm. The broad peak $\sim 47^\circ$ corresponds to the Pt(111), and peaks marked with “*” corresponds to the SRO. Other peaks correspond to the NN.

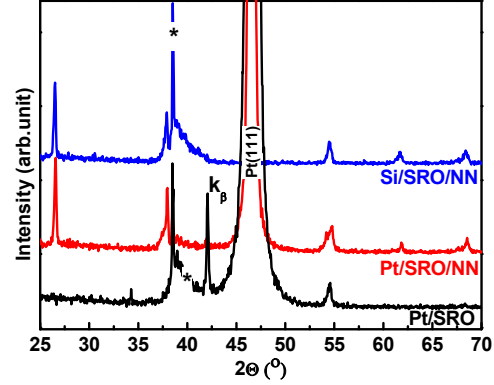
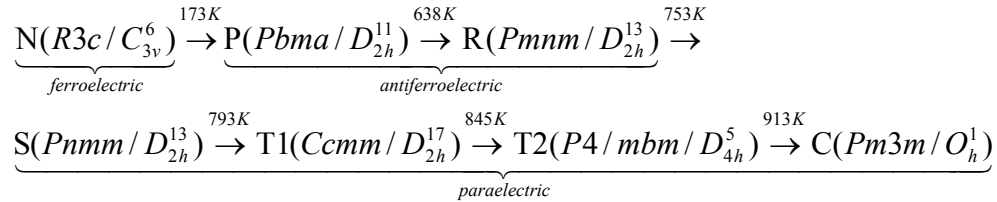


Fig. 6.1.1. X-ray diffraction studies using 20 scans for NN thin films on 2 different substrates - Pt/SRO and Si/SRO, as well as XRD pattern of the substrate.

6.1.2 Dielectrics

Fig. 6.1.2a shows the dielectric permittivity ε and loss factor $\text{tg}\delta$ as a function of temperature (T) for Pt/SRO/NN with appreciable frequency dependence of the dielectric permittivity $\varepsilon(T)$ (110 kHz and 220 kHz): as the frequency increase, the value of ε_{max} decreases and T_c slightly shifts to higher temperature (from 641 to 646 K) [37]. According to the sharp phase transition, the chosen heating rate of 2 K/min was too high so that a certain degree of inaccuracy of about ± 2 K for the established T_c has to be considered. The anomalous peak in ε and $\text{tg}\delta$ at T_c corresponds to one transition (P to R) from a series phase transitions of NN, which are [11]



Of these phases, N is trigonal, P, R, S and T1 are orthorhombic, T2 is tetragonal, and C is cubic. The same behavior of $\varepsilon(T)$ and $\text{tg}\delta(T)$ (a sharp increase of ε and $\text{tg}\delta$) was observed for NN single crystals [40, 50] and ceramics [84]. The detected T_c is in a good agreement with that of the single crystals [11, 40, 48, 50] and ceramics [84, 78]. ε and $\text{tg}\delta$ at 1 kHz at room temperature is 200 and 0.3, respectively. In this work ε is lower and $\text{tg}\delta$ is higher compared with those by Saito [84] (ε and $\text{tg}\delta$ are 252 and 0.03, respectively, for NN film of thickness 780 nm deposited by PLD on SRO/SrTiO₃ substrate), and measured on single crystals [40] and ceramics [78], but in good agreement with detected dielectric values by Matthias [48] for less perfect NN crystals.

The Fig. 6.2b shows frequency dependence of ε and $\text{tg}\delta$: dielectric permittivity decreases till ~ 10 kHz, then it is slightly linearly decreases till 1 MHz; loss factor decreases till ~ 10 kHz, then keeps constant till ~ 100 kHz, and then increases till 1 MHz.

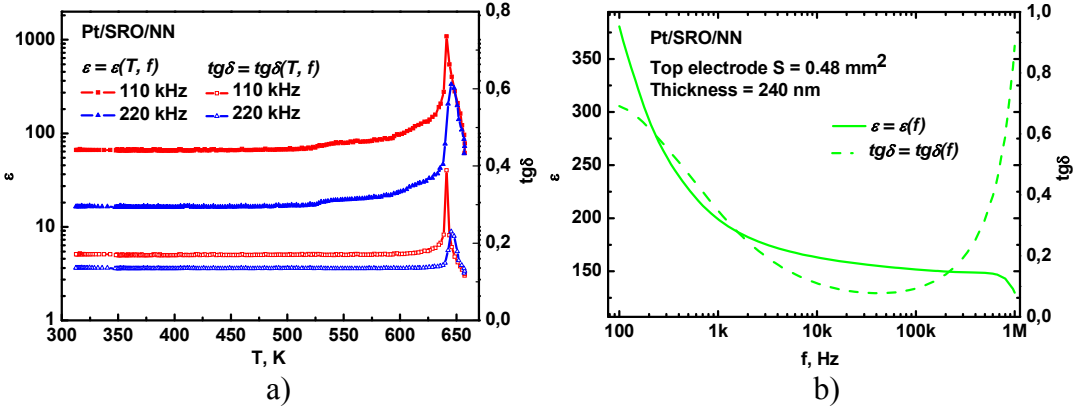


Fig. 6.1.2. Dielectric permittivity ε (solid symbols) and loss factor $tg\delta$ (open symbols) as the function of the temperature at frequencies of 110 kHz and 220 kHz (a); ε and $tg\delta$ as the function of frequency from 100 Hz till 1 MHz (b).

6.1.3 Raman spectroscopy

Figure 6.1.3 shows the Raman spectra of NN samples at 200 – 1100 cm^{-1} , corrected by the Bose-Einstein temperature factor. The broad peaks at ~ 240 , 620 and 850 cm^{-1} were deconvoluted successfully (Fig. 6.1.3bc) and can be reproduced by superposition of 5, 3 and 3 Lorentzians, respectively. Such these broad three bands were observed also for NN powders [67, 73] and one broad band at ~ 600 cm^{-1} for ceramics [71]. At room temperature totally 12 Raman bands were observed in these experiments [37]. The higher-frequency broad bands consist of two strong peaks at 605 and 869 cm^{-1} with two shoulder bands for Pt/SRO/NN, and 615 and 835 cm^{-1} also with two shoulder bands for Si/SRO/NN (Fig. 6.1.3c). These peaks can be attributed to the internal modes of the Nb-O stretching and combination of stretching and bending [73, 159]. The broad peak at ~ 240 cm^{-1} , in accordance with literature, is due to the NbO₆ interbond angle bending [159, 160].

Raman spectra at various temperatures of NN on heating are shown in the Fig. 6.1.3d. Almost all peaks can be resolved up to 743 K: above 200 K, the band at ~ 480 cm^{-1} with weak intensity vanishes, and above 573 K the broad peak at ~ 835 cm^{-1} vanishes. All the Raman bands show the expected broadening with increasing temperature. Raman mode shifts ω as the function of temperature for NN on SRO/Si are given in Fig. 6.1.3e. Up to 743 K, the Raman spectra are not strongly temperature dependent except for the broad peaks at ~ 615 and 835 cm^{-1} . It can be seen that the second-order shoulder bands around 615 and 835 cm^{-1} can be detected only up to 473 K. Similar results were found in the work of Wang [71]: there is one strong peak and two shoulder bands at ~ 600 cm^{-1} , which exist from room temperature up to 460 K, and above 460 K one shoulder band vanishes. The modes at ~ 240 and 620 cm^{-1} of NN deposited on Pt/SRO are shifted to lower values of ω in comparison with those of NN on Si/SRO and for NN ceramics [71] (Fig. 6.1.3ae). Only two modes at 437 and 673 cm^{-1} of the Pt/SRO/NN and Si/SRO/NN are comparable with the data of ceramics. The modes of Pt/SRO/NN at 568, 607 and 869 cm^{-1} , and of Si/SRO/NN at 259 and 280 cm^{-1} are the same as those of ceramics (Fig. 6.1.3 c), but with slightly differences between the films. The higher values of ω at 309, 612, 624 and 873 cm^{-1} for Si/SRO/NN and lower values ω at 219 and 247 cm^{-1} in comparison with ceramics can be due to the strain at the film/substrate interface, which appears due to the lattice mismatch of the film and substrate. However, a size-induced phase transformation and/or grain boundary effects can also be an explanation of the established distinction, which will be discussed below.

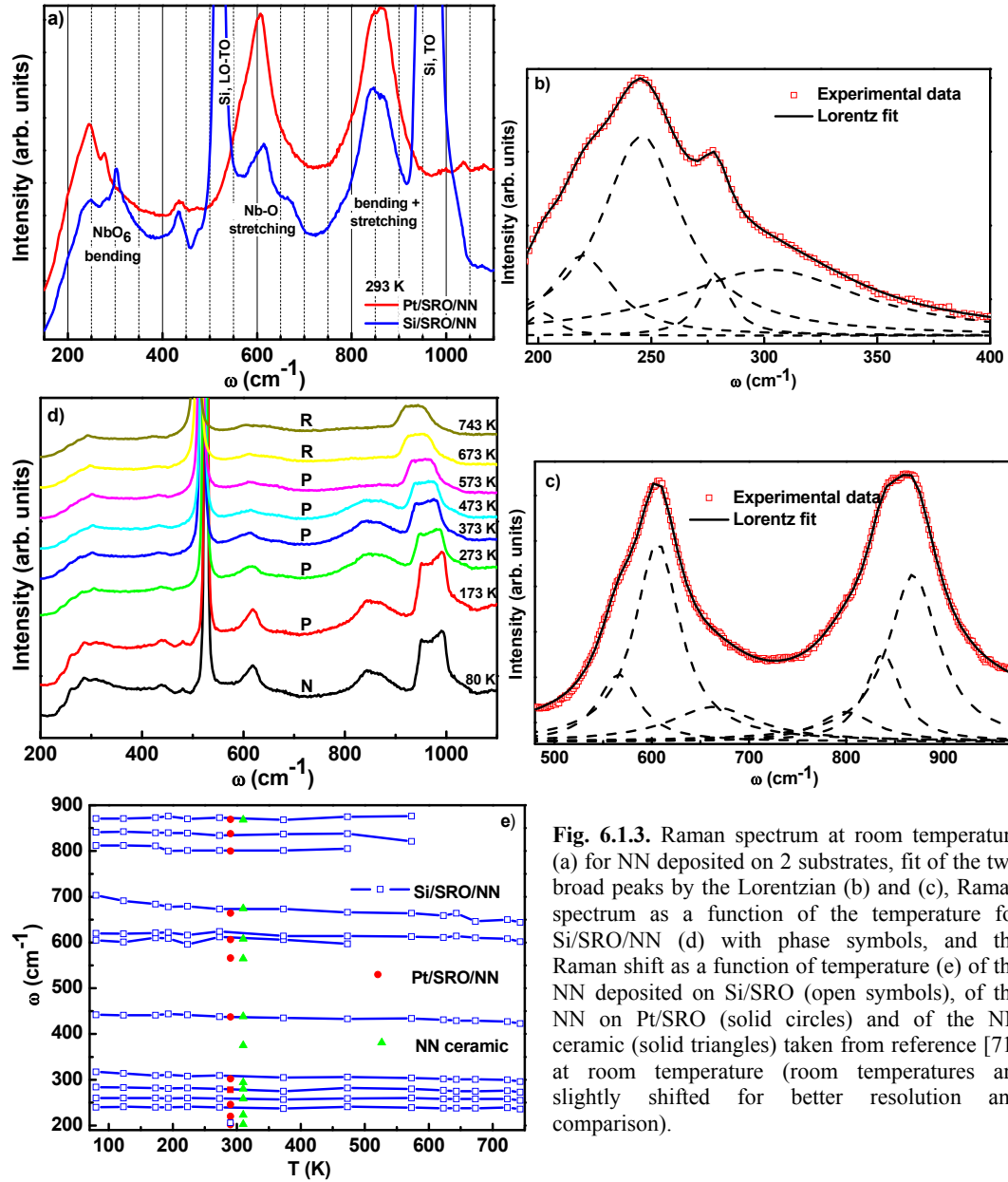


Fig. 6.1.3. Raman spectrum at room temperature (a) for NN deposited on 2 substrates, fit of the two broad peaks by the Lorentzian (b) and (c), Raman spectrum as a function of the temperature for Si/SRO/NN (d) with phase symbols, and the Raman shift as a function of temperature (e) of the NN deposited on Si/SRO (open symbols), of the NN on Pt/SRO (solid circles) and of the NN ceramic (solid triangles) taken from reference [71] at room temperature (room temperatures are slightly shifted for better resolution and comparison).

6.1.4 AFM

Surface morphology images detected by AFM are given in Fig. 6.1.4. The surface of PLD NN films is very smooth: the mean value for all calculated root mean square (RMS) roughness of the films is 3 and 6 nm for NN on Pt/SRO and Si/SRO, respectively. The average grain size is around 100 and 150 nm for NN on Pt/SRO and Si/SRO, respectively. NN films were grown on two different substrates simultaneously, but the higher heat treatment temperature and the substrate and uniformity of the plasma beam may act as a nucleation centre and help the grains to grow larger on the Si/SRO substrate. The local friction force (lateral force) over the sample surface is given in Fig. 6.1.4. It can be seen that the angle of torsion is not changing, which means that the surface is uniform without different zones of different friction factors. The AFM morphology confirmed that a dense and smooth NN thin film can be deposited by PLD on Pt/SRO and Si/SRO substrates.

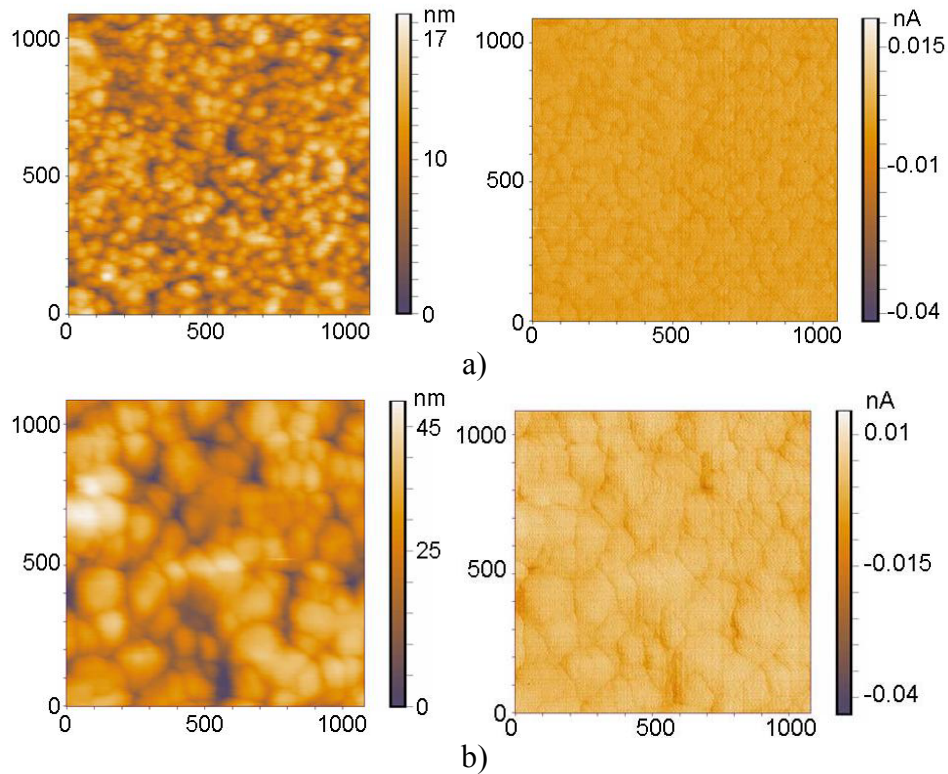


Fig. 6.14. Surface topography (left) and lateral force images (right) with scanned area (1×1) μm for NN on a) Pt/SRO, and b) Si/SRO. The RMS roughness for the given images is 3 and 6 nm.

6.1.5 Optical properties

First of all the substrate optical properties were evaluated. Refractive index n and extinction coefficient k as the function of the photon energy for the platinum and conductive oxide SRO is given in Fig. 6.1.5a and Fig. 6.1.5b, respectively. Dielectric function of these materials were characterized by the quadruplicate and quintuplicate LO, respectively. The fitting parameters of LO are summarized in the Table 6.1.1. Optical properties of the Pt bottom electrode (Fig. 6.1.5a) are in good agreement with the optical properties of the Pt bulk [161]. Optical properties of SRO thin film (Fig. 6.1.5b) are reported for the 1st time in this work. For my knowledge there is no literature on optical properties of SRO thin film. This work is the first report on $n(E)$ and $k(E)$ of the conductive oxide SrRuO₃ [38].

Tab. 6.1.1. Fitting parameters of the LO for Pt and SrRuO₃ materials: amplitudes of the five oscillators A_{1-5} , central energies of the five oscillators E_{c1-5} , and vibration frequencies of the five oscillators B_{1-5} . The values are given in electron volts (eV).

Material	A_{1-5} (eV)	E_{c1-5} (eV)	B_{1-5} (eV)
Pt	480.13; 1.93; 2.05	0.19; 1.42; 11.25	0.35; 4.86; 10
SrRuO ₃	1.55; 1.11; 5; 54; 1.02e-6; 1.95	3.09; 1.56; 6.24; 0.004; 3.67	0.83; 1.02; 2.21; 0.0003; 1.32

Fig. 6a illustrates an experimental data and the second model numerical fit of the main ellipsometric angles ψ and Δ as a function of the photon energy at the incidence angles 65° and 70° for Si/SRO/NN sample. The simple model, where the sample was

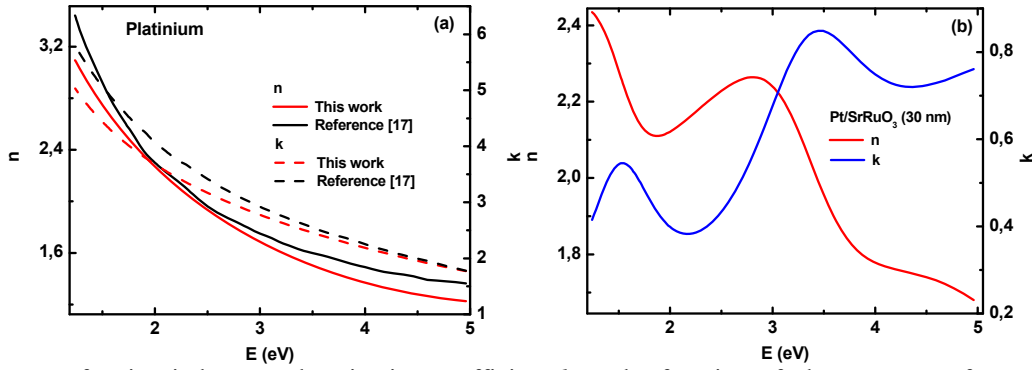


Fig. 5. Refractive index n and extinction coefficient k as the function of photon energy for Pt (a) and SrRuO₃ (b).

considered to consist just from the substrate, film, and top layer, could not give such good agreement between measured spectra and calculated one as it was established assuming that the film is a mixture of the host material and the voids. By using this model it was found that the high-frequency lattice dielectric constant and the volume fraction of the second (porous) phase of NN material were established to be 1.10 and 35%, respectively. The ϵ_{∞} and band gap energy for the 2nd phase is much lower than that for the host material of NN film (see Tab. 6.1.1). Similar results were detected for Pt/SRO/NN sample too, but with the lower value of volume fraction. But there is significant difference in the amplitude of the calculated Δ in comparison with the measured one, what is due to the thickness nonuniformity of the film. The thickness distribution of the thin films rise depolarization of the light, which can be seen as the rounded shape of minima and maxima in Δ (since Δ is very sensitive to the thickness). It means that thickness non-uniformity have to be taken into account while fitting experimental data. Otherwise we can evaluate unphysical parameters of the film. Also it is very important to choose the proper oscillator to characterize complex dielectric function of the material. Unfortunately in this case the Lorentz oscillator (LO) was used, which does not give good fit to experimental data (Fig. 6.1.6a) and characteristics to the complex dielectric function at the near ultraviolet and ultraviolet (UV) regions (gives huge oscillations of n and k at

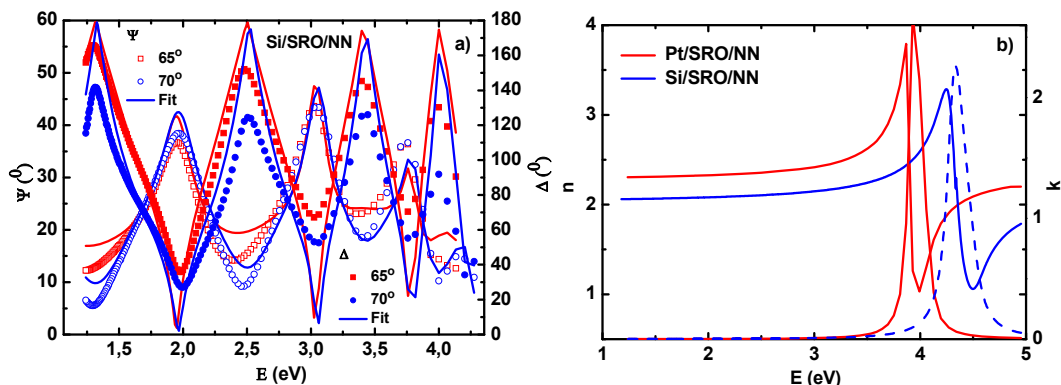


Fig. 6. Experimental ellipsometric angles ψ and Δ (open symbols) and their numerical fit (solid line) as a function of the photon energy E (eV) for the Si/SRO/NN sample (a); refractive coefficient n (the left axis) and extinction coefficient k (the right axis) of NN films deposited on Pt/SRO (solid line) and Si/SRO (dashed line) substrates (b).

the UV (Fig. 6.1.6b) for the ferroelectrics and some semiconductors [132, 133]. The Tauc-Lorentz [137] oscillator (TLO) as more flexible functions at the fundamental band gap E_g and higher energies in the UV, since this function rapidly decrease to zero away from their center energy and do not have long asymptotic tails as LO which can result in

unwanted absorption through the band gap and below. The details of these oscillators can be found in the chapter “3.6.1 Oscillator models for the dielectric function”. After analyzing different oscillators and choosing the proper one, the fitting of the experimental data started from the begging.

Experimental and modeled main ellipsometric angles ψ and Δ of the NN thin film on the Pt/SRO substrate is shown in the Fig. 6.1.7a. In the model was assumed the film thickness non-uniformity and the surface roughness. Gradient of the optical properties was studied in the spectral range from 400 - 1000 nm and will be discussed below. The ψ and Δ spectra exhibit oscillations at the lower energies because of the interference among multiple-reflected beams in the thin film. This indicates that NN film is transparent. The frequency of oscillations depends on the thickness of the film: basically, the thicker the film is, the higher the frequency.

The best model fit of NN thin film was found to be very complicated due to the particular non-idealities of this film. The fit was started from the simple model - substrate/film (Model 1 in Fig. 6.1.8a). The mean square error (MSE) was found to be very high. Significant difference in the amplitude of the calculated Δ in comparison with the measured one is due to the thickness nonuniformity of the film (the like in case of the Si/SRO/NN films). The thickness distribution of the thin film rise depolarization of the light, which can be seen as the rounded shape of minima and maxima in Δ (since Δ is very sensitive to the thickness, [85]). Due to this fact thickness non-uniformity were added in the model, and it was found to be from 3 to 11 % within the ~ 2 mm light spot from the thinner place of the film to the thicker one. The thickness of the trapezium-shaped film is changing from 150 to 300 nm. The MSE significantly decreased by adding thickness non-uniformity (Model 2 in Fig. 6.1.8a). Main ellipsometric angles were measured at several places of the film from the thinner to ticker place. Effective optical properties were evaluated at the each place. Optical properties of the mean value of the host material of the whole film are plotted in the Fig. 6.1.7b. The fitting parameters of the double TLO are summarized in Table 6.1.3.

Tab. 6.13. Fitting parameters of the double TLO for the host material of the NN film: amplitudes of the two oscillators A_{1-2} , central energies of the two oscillators E_{c1-2} , vibration frequencies of the two oscillators B_{1-2} , and optical band gap of the two oscillators E_{g1-2} . The values are given in electron volts (eV).

Material	A_{1-2} (eV)	E_{c1-2} (eV)	B_{1-2} (eV)	E_{g1-2} (eV)
NaNbO ₃	52.41	4.69	1.59	3.39
	227.66	4.48	6.11	3.86

To improve the fit, the before the film was considered to be a mixture of the host material and the voids (or grain boundaries) by using EMA, what is correct as a model it's self for ferroelectric materials [162]. Insomuch as the amplitude of calculated Δ was not improved by the thickness non-uniformity (Fig. 6.1.6a), established values of the volume fraction can be considered just as a best fit model to the experimental data and cannot be connected with a physical properties of the film. If the film was considered to be a mixture of the host materials and voids, after evaluating the film thickness distribution, volume fraction was found to be just 0.5 % and MSE value was slightly improved. Nevertheless, the improvement was so small that it could not be treat as a remarkable characteristic of the film. To minimize the correlation of the fitting parameters [85] the film was not considered being as the EMA media.

The interface layer between bottom electrode and film also did not give any improvement of the fitting. And again to avoid correlation of the fitting parameters the

interface was not taken into account. The surface roughness was found to be 2 – 5 nm (it varied from place to place), and MSE decreased to 24. This is significant improvement of the fit and this parameter describes the surface morphology of the film and it is in good

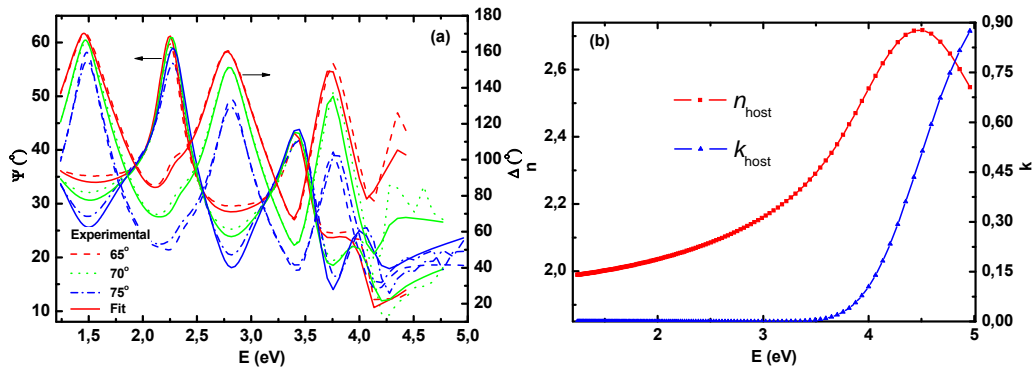


Fig. 6.17. Experimental (discontinuous lines) and modeled (continuous lines) main ellipsometric angles ψ and Δ as the function of incident angles and photon energy of Pt/SRO/NN thin film/roughness. Thickness of the SRO, NN and roughness is 11nm, 190 nm and 3 nm, respectively (a). Optical properties of the mean value of the host material of the NN thin film versus photon energy (b).

agreement with AFM data [37]. Ignorance of the surface layer in the model results in unphysical absorption artifacts in the measured optical constants, namely significant absorption in the transparent spectral range below the band gap. Adding surface roughness to the model completely eliminates these artifacts. This demonstrates the sensitivity of spectroscopic ellipsometry to the surface microstructure and the need to include surface effects in the analysis model.

According to the theoretical predictions [120] and experimental result on perovskite $\text{PbZr}_{0.235}\text{Ti}_{0.765}\text{O}_3$ (PZT)/pyrochlore double layer [30], behavior of the polarization profile remarkably changes for very thin film what can be connected with strains in the film. The wavelength range from 400 nm to 1000 nm with minimal uncertainties and k close to zero was used in these calculations to evaluate depth profile of the refractive index.

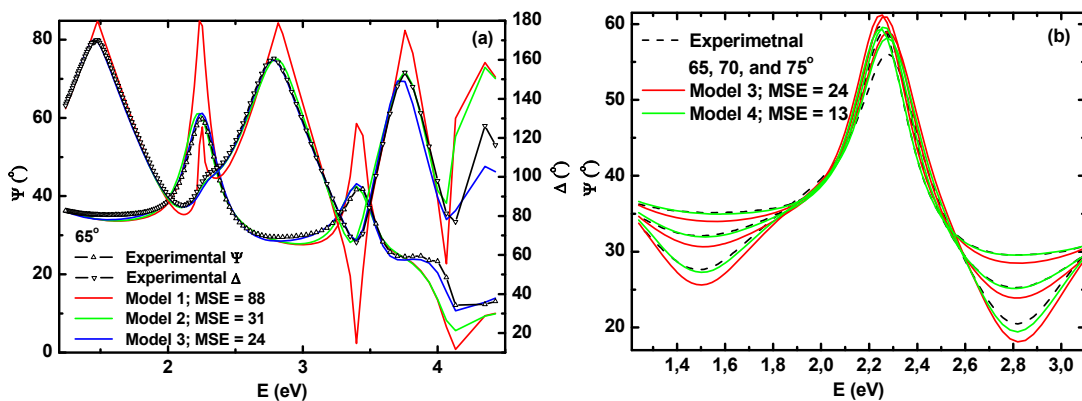


Fig. 6.1.8. Experimental (symbols) and modeled (continuous lines) main ellipsometric angles ψ and Δ as the function of photon energy of Pt/SRO/NN at the incident angle of 65° using different models (a): Model 1 – Pt/SRO/NN, Model 2 – Pt/SRO/NN with thickness non-uniformity, Model 3 - Pt/SRO/NN with thickness non-uniformity/surface roughness. It can be seen how significantly MSE decreases by taking into account thickness non-uniformity and surface roughness. When gradient of the optical properties was added to the model, MSE decreases even more (b).

Effective optical properties at the different sample places from 400 – 1000 nm with different thickness were evaluated (Fig. 6.1.9a). It can be seen that effective refractive index (host material of NN) has a tendency to be constant almost at the all thicknesses,

except thicker one close to the sample edge [38]. Such behavior could be related with both technology aspects and possible stresses often appeared in gradient materials.

In the simple calculations above effective thickness, thickness non-uniformity, surface roughness, and effective optical constants of the NN film was evaluated. The next step is to substitute inhomogeneous film layer by a stack of homogeneous ones (model of graded layers) to make approximation of the reflectivity from inhomogeneous layer. This model parameterized by the thickness and complex index of refraction conforms to the real graded structure [21, 85]. Experimental and calculated ψ in the photon energy range of 1.24 – 3.10 eV using graded model (Model 4) and in comparison with Model 3 is shown in Fig. 6.1.8b. It can be seen that fit is excellent (MSE error decrease to 13) in all spectra except maxima of ψ at the incident angle of 75°. Calculated depth profile of refractive index at 500 nm for the film with different thickness is plotted in Fig. 6.1.9b. An exponential growth of refractive index as the function of thickness was established (Fig. 6.1.9b). With increase of the thickness, n close to the bottom of the film decrease, but closer to the top of the film increase. This explains why effective values of the host material of NN are almost constant with the thickness (Fig. 6.1.9b). With increase of the thickness the value of the exponent has a liability to increase, while variation range of the refractive index reaches its maximum value around 200 nm and then decreases (Fig. 6.1.9b). The real reason of such behavior is under further investigation now, but it could be caused by stress and strain distribution in this gradient structure.

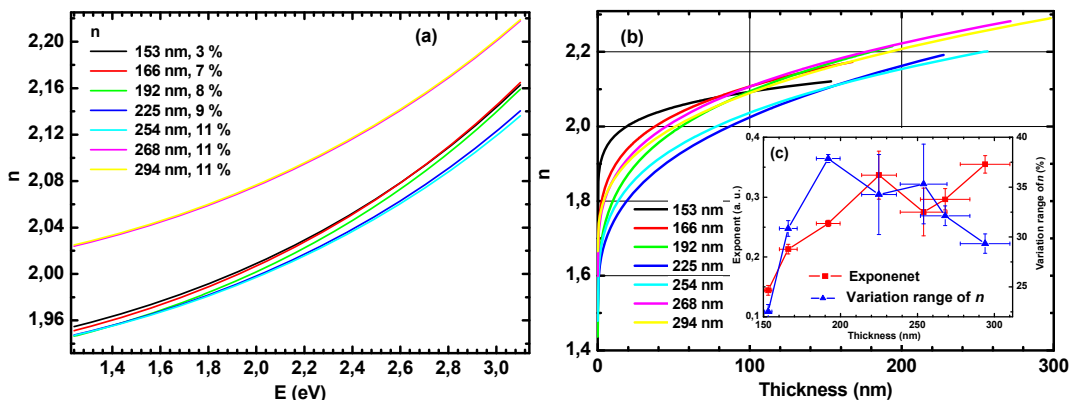


Fig. 6.1.9. Dispersion of the effective refractive index of the NN at the different thicknesses (a) (nm) and thickness non-uniformity (%). Depth profile of the refractive index n as function of the film thickness (b). Value of the exponent and variation range of n versus thickness (c).

6.1.6 Thermo-optics

Temperature dependence of the main ellipsometric angles ψ and Δ at the selected temperature range of 298 – 820 K at as a function of phonon energy is illustrated in Fig. 6.1.10. By fitting each spectra using above described model, temperature dependence of band gap energy and refractive index was found. Refractive index n of Si/SRO/NN thin film at 300 nm as the function of the temperature is presented in the Fig. 6.1.11a. Several found anomalies of $n(T)$ at 645, 726, 750, and 794 K are in good agreement with previous results on effective refractive index temperature dependencies on Si/SRO/NN thin films [35].

For perovskite crystals the n usually increase as the temperature rises [140]. Nevertheless, the polycrystalline film structure, defects and stresses in the film can change this behavior dramatically that can be seen in this case. Moreover, these measurements were performed at shorter wavelengths close to the band gap energy to increase the sensitivity.

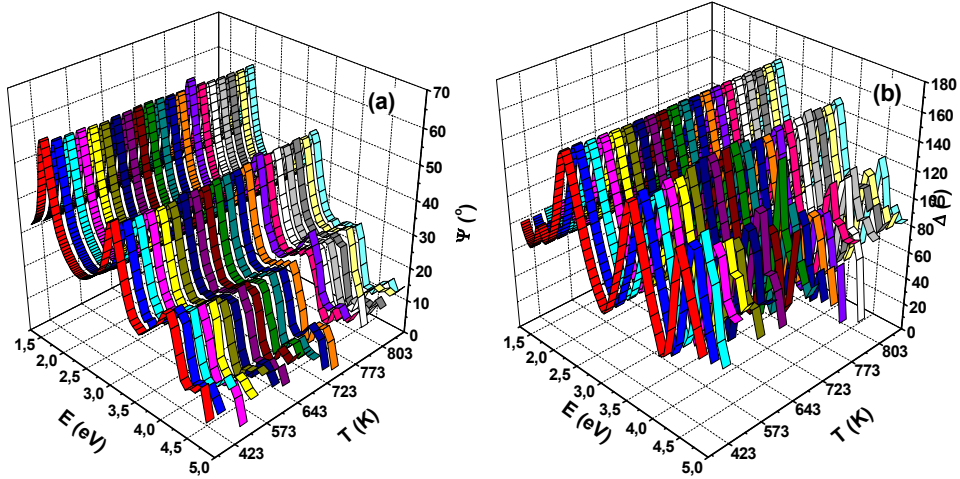


Fig. 6.1.10. Temperature variation of the spectral dependence of main ellipsometric angles a) ψ and b) Δ .

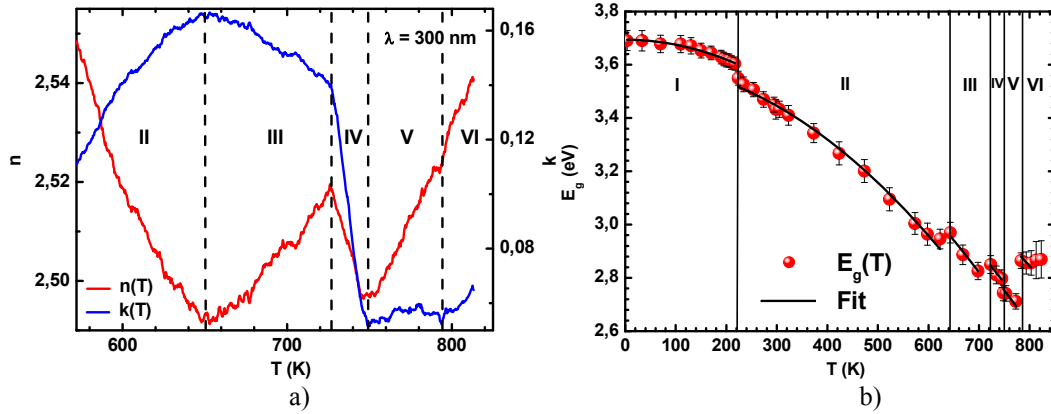


Fig. 6.1.11. (a) Temperature dependence of refractive index n and extinction coefficient k at the wavelength of 300 nm for NN thin film. There are very well pronounced anomalies of the n at 645, 726, 750, and a weak one at 794 K. (b) Temperature dependence of the band gap energy of NN thin film.

Tab. 6.1.4. The fitting parameters of Varshni quadratic relation at the each phase: $E_g(0)$ – band gap energy at 0 K, A - material constant, $\hbar\omega_{ph}$ is a mean phonon frequency, $\partial E_g / \partial T$ - temperature coefficient of the optical gap.

Fitting parameters	Phase I	Phase II	Phase III	Phase IV	Phase V	Phase VI
$E_g(0)$ (eV)	3.6941	3.6079	3.6941	3.6941	3.6941	3.6941
A (meV)	21.21	21.25	32.01	19.75	20.01	17.52
$\hbar\omega_{ph}$ (meV)	12.98	13.22	16.32	13.43	13.33	13.99
$\partial E_g / \partial T$ (meV/K)	-0.46	-1.52	-2.57	-2.40	-1.34	-0.49

The fundamental absorption edge for each film was determined from the spectral dependence of the imaginary part of dielectric constant $\varepsilon_2 = 2nk$ by applying the Tauc relation $\hbar\omega\varepsilon_2 = const \cdot (\hbar\omega - E_g)^l$, where \hbar is the reduced Planck constant, ω is the angular frequency, E_g – band gap energy, and $l = 1/2$ for the allowed direct transitions and 2 for indirect transitions. By extrapolating the linear part, the optical energy gap was deduced at $(\hbar\omega\varepsilon_2)^2 = 0$, giving the fundamental absorption age E_g for the direct transition. The optical band gap as the function of the temperature of Pt/SRO/NN thin

film is given in Fig. 6.1.11b. Essential decrease of the E_g from 4 till ~ 780 K can be seen: from 3.691 to 2.865 eV or 1.3 times. Five pronounced E_g jumps at 225, 643, 723, 750 and 788 K of $E_g(T)$ were evaluated. Varshni quadratic relation (formula (3.90) in chapter “3.9 Thermo-optics”) fit to the experimental $E_g(T)$ can be seen as a black line in Fig. 11b. Fitting parameters of the $E_g(T)$ quadratic relation are summarized in the Tab. 6.1.4.

6.1.7 Discussion

In this work the Raman shift frequencies and optical properties of Pt/SRO/NN film with smaller grains and lower roughness was established to be different from those detected for Si/SRO/NN film with bigger grains and higher value of the roughness. This can be caused by the fact that the Pt/SRO/NN film is denser, with the lower value of volume fraction as it was found from optical results and less stressed at the film/substrate interface than the Si/SRO/NN film. But it could be also due to the size-induced phase transformation of the NN: some specific bands are drastically shifted to the lower wavenumber region on decreasing the grain size. One of the most recent explanations is based on increase in the internal pressure due to the surface curvature and small particle radius (Gibbs-Thomson effect) [163]. It is one of the possible mechanisms for stabilization of more symmetric structures than the transformation from the thermodynamically stable ones at ambient temperature and pressure - transition from a more symmetric to a less symmetric structure attended with a decrement of the lattice. In the work of Shiratori a size-induced phase transformation from a monoclinic structure to a triclinic structure was discovered for $(K_{0.50}, Na_{0.50})NbO_3$ (KNN) powders at a critical size of about 200 nm [163]. The perovskite cell volume of KNN increased due to the transformation, induced by decreasing particle size. Result of KNN is opposite to that for NN powders [73] and makes us to believe that ionic distributions (K/Na) or charge distribution processes resulted in volume expansion [164] as a driving force of this phase transformation. If the grains are small, it is more complicated to implement homogeneous ionic distribution than when the grains are large. In the case of NN, there is no difficulty of such distribution and therefore Gibbs-Thomson effect is likely to be the responsible transformation mechanism. Insomuch as the size induced phase transformation was detected for the powder and not for the thin films, and in this work the difference in the grain size is much smaller than that for Shiratori samples, to be sure whether this kind of effect can be consistent for NN thin films, there is need to provide series of additional measurements with samples of the wide range of grain sizes.

Another substantial explanation of detected deference in the optical and Raman spectra could be the grain boundary effects. From the modeling of ellipsometric measurements, it was established that it was not possible to improve experimental results by using only surface roughness layer even for the high values of $d_s > 20$ nm. When the film was assumed to be with an optical gradient, the fit significantly improved. In the direction to the substrate refractive index of the film decreased till very small values close to the values of glass (Fig. 6.1.9b).

If the sample is inhomogeneous, then its effective dielectric response usually can be determined, which does not give full information about the spatial variation of the dielectric function. The inhomogeneous material often can be considered as a densely filled micro-composite formed by individual, dielectrically homogeneous parts. Depolarization field, which always appears on the boundaries between the different parts, tends to reduce the probing electric field in the higher-permittivity parts. As the result, there can be pronounced differences between the effective dielectric response and the response of individual homogeneous parts.

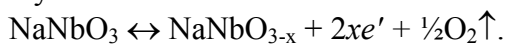
The EMA model is particularly useful in describing the properties of inhomogeneous, granular materials (ceramics, polycrystalline films), in which the grain boundary region (shell) plays the role of the second component whose dielectric properties may differ from that of the bulk (core) [165, 166]. In high-permittivity materials this region has usually lower permittivity (in ferroelectrics it might be non-ferroelectric - dead or passive layer) and in semiconductive ceramics it may differ in conductivity (e. g. blocking boundaries in grain-boundary capacitors).

In the earlier work [37] it was found that sample can be estimated as the EMA media, without taking into account the thickness non-uniformity what is very pronounced in these films. As the result the shift of the Raman modes was explained by the grain boundaries effect. By improving fitting possibilities, the thickness non-uniformity was taken into account and it was found that then EMA model showed no efficiency to fit experimental data. Only depth profile analyzes gave improvement to the fit. From fitting the gradient model to the ellipsometric data, the smaller values of optical constants was found close to the substrate of the film. The evidence of the lower permittivity parts in the sample can be found also from dielectric results of NN films: it was detected that dielectric permittivity is lower and dielectric losses are higher then those for bulk materials (Fig. 6.1.2ab), but in good agreement with the results of less crystalline samples. Such difference can be due to the defects localized on the grains and/or grain boundaries and/or at the interface of the film.

Properties of phonon modes, specially the soft modes, in thin films should obviously reflect the substrate-induced stresses, but in addition to that, influence of grain boundary effects and interfacial layers between the film and substrate or electrode can be very important or even dominant [162]. According to the results on optical and dielectric properties, detected difference between Raman shift frequencies of the films and bulk materials can be caused not only from size impacts, but also from the substrate-induced stresses.

Several anomalies of $n(T)$ at 645, 726, 750, and 794 K (Fig. 6.1.10.) and jumps of the $E_g(T)$ at 225, 643, 723, 750, and 788 K (Fig. 6.1.11b) were established in this work and are summarized in Tab.6.1.5 in comparison with other PT studies on NN. The minimum of n at 645 K and jumps of E_g at 643 K corresponds to the $P \rightarrow R$ phase transition. Detected PT temperature $T_{P \rightarrow R}$ is in good agreement with earlier dielectric measurements on similar films [37]. The PT transition ~ 643 K was established by different techniques by other authors: dielectric measurements on the single crystals [48] and thin films [84], and also on the single crystals by X-ray [12, 15, 16, 42, 54], optics [42, 48] and DTA [15, 54]. In several works this transition was observed at 633 K [14, 40, 77, 50], and in some works even at $T > 643$ K [43, 71]. Should be noticed that NaNbO_3 PT temperatures dramatically changing if there is any small deviation from the NN stoichiometry. The KNbO_3 - KNaO_3 phase diagram [81] shows, that just 2 % of K presences in the NN, changes, for example, phase $P \rightarrow R$ from 643 K to ~ 623 K.

Evidence of different T_c of the $P \rightarrow R$ phase transition (and also others) is very feasible due to the oxygen vacancies $\text{O}_0 \leftrightarrow V_0'' + 2e' + \frac{1}{2}\text{O}_2 \uparrow$ in accordance with the defect chemistry theory [167]: in the sample are formed primarily doubly ionized oxygen vacancies V_0'' and two electrons which can participate in conductivity. In the case of NN crystal it can be written in a form of



It was found by Molak [57] that T_c varies with the concentration of V_0'' . Measurements were performed on NN crystals heated at reduced air pressure thereby causing the generation of V_0'' . The influence of the V_0'' on the transition $P \rightarrow R$ was studied, and was

established that T_c is higher for the crystals with greater oxygen nonstoichiometry, i.e., for the samples heated at lower partial pressure of oxygen: at $2 \cdot 10^{-2}$, $2 \cdot 10^0$ and $2 \cdot 10^4$ Pa the T_c during heating is 647, 640 and 635 K, respectively. It should be noticed that Molak established the same effect also on Mn^{2+} doped NN crystals. Theoretician Levanyuk [168] showed that local fluctuations in the order parameter caused by point defects lead to shifting of T_c . Increasing or decreasing of the T_c is depended on the type of frozen in defects, and by this it is possible to explain the observation of different T_c . It is possible, according to Molak, that these NN thin films samples and samples of the other scientific groups, who determined $T_c > 633$ K for $P \rightarrow R$ transition, have oxygen nonstoichiometry.

Unusual PT at 723 K was found in $E_g(T)$ dependence as well as in $n(T)$ at 726 K. This rather suspicious transition at ~ 718 K was noted in three X-ray studies [14], but described differently in each. Optical observation in [35] was the second evidence for it, and this is already the thread one. The first was done by Lefkiwitz. From X-ray was found that during the $P \rightarrow R$ transition the niobium ions displace inside the oxygen octahedral of NN crystal [46]. This is the transition where the strongest changes of the

Tab. 6.1.5. Phase transition (PT) temperatures of $NaNbO_3$ established in this and earlier works in comparison with results of other scientists (references in crotchets). The type (thin films, ceramic et. al.) of NN, method of detecting PT, phase, symmetry and multiplicity are also given.

PT	This work	Other works on $NaNbO_3$ phase transitions		Phase, symmetry, multiplicity
I		~ 90 [76] ~ 95 [76]		N ; rhombohedral; $2a \times 2a \times 2a$ [12, 16]
I \rightarrow II	225	~ 280 [76] ~ 250 [76]	143 [12], 193 [12] 323 [16]	P ; orthorhombic, $2a \times 2b \times 4c$ [12, 16]
II \rightarrow III	643; 645	633 [77] 643 [35], 645 [84] 649 [71], ~ 650 [76]	633 [14, 50], 635 [54] 643 [12, 42, 48], 646 [15, 16] 663 [43]	R ; orthorhombic, $2a \times 4b \times 6c$ [12, 16]
III \rightarrow IV	723; 726	718 [35]	693 [43], 698 [42] 713 [14]	
IV \rightarrow V	750; 750	776 [35]	743 [14] 753 [12, 16, 42, 48, 54] 758 [15]	S ; orthorhombic, $2a \times 4b \times 6c$ [12, 16]
V \rightarrow VI	788; 794	793 [35]	833 [43] 791 [14], 793 [12, 16, 54] 796 [15]	$T1$; orthorhombic, $2a \times 2b \times 2c$ [12, 16]
		805 [35]	799 [14] 801 [15, 16], 803 [54]	
Type	Thin Films [35, 169] Ceramics [71, 76, 77]	Single crystals Polycrystals [54]		
Method	Ellipsometry [35], Dielectric [76, 77, 84], Raman [71, 76]	Dielectric [48], X-Ray DTA [15, 54]		

NN structure occurs. Due to the presence of $V_{O''}$, reduction in valence of niobium ions appears what leads to change in the local field in the neighborhood of these defects. And what was found at ~ 720 K is some kind of relaxation of defects on grain boundaries.

The next anomalies of n were found to be at 750 and 794 K, and jumps of $E_g(T)$ at 750 and 788 K. The anomaly at 750 K agrees with T_c of $R \rightarrow S$ [12, 16, 54], but transition at 793 K agrees with the T_c of $S \rightarrow T1$ [12, 16, 54].

There were anomalies of n , k or E_g at around 805 K observed for Pt/SRO/NN thin films like it was with the Si/SRO/NN films [35]. In the case of the Si/SRO/NN films we were using an interpretation of an appearance of the regions with S and $T1$ structure.

Because of difference in lattice parameters, strains occur between $T1$ and S regions, impede the growth of $T1$, and stabilize the continued existence of S [16]. While temperature keeps rising, the lattice parameter cause changes in strain, at 805 K the distribution and magnitude of the strains become critical, regions with S structure starts to disappear and $T1$ growth has no longer interception. Lefkovitz [14] found that at the temperature region of 791 and 799 K a negative thermal expansion exists, and explained it by the circumstances of a temperature gradient or a particular type of mechanical stress [14]. Insomuch as no anomaly was observed at ~ 803 K in case of Pt/SRO/NN films, it could be that they are higher oriented then Si/SRO/NN films.

Low temperature phase detected from the $E_g(T)$ at 225 K during cooling is in good agreement with some results on ceramics [76], but no analogy with results on single crystals. There can not be fined any similar data describing this low temperature phase in literature. A large thermal hysteresis of ~ 80 K was reported by Darlington (1973) for the low temperature transition. He found that single-domain crystals of phase P transformed rapidly to the twinned phase N at the temperature below ~ 143 K; reverse transition was again rapid, occurring at ~ 223 K; and these crystals always returned to single-domain crystals of phase P . The large hysteresis can be caused by the great structural change required at the transition, tending to make difficulties of the nucleation at the appearing phase. Moreover, rapid growth of the appearing phase would be the result of a high energy at the interface between the nuclei and bulk. And like in the case of Si/SRO/NN films of the PT of $S \rightarrow T1$, where coexist two phases S and $T1$, here also coexist twinned phases, but in this instance N and P [12]. Insomuch as phase $N \rightarrow P$ appears at the different temperatures as reported in many works (Tab. 6.1.5.), there is a reason to consider that it may be caused by the different volume fraction of the N/P phases [12], what generate instability of the $N \rightarrow P$ phase transition. In the RT studies of the Pt/SRO/NN thin films [38] was found that these films have pronounced depth profile of the refractive index what can be caused by the strains. As the result the lattice parameters of the crystallites at the bottom of the film is slightly different from those at the surface of the film. It should be also mentioned that because of the high sensitivity of ellipsometric technique to any global and local structural changes, the phase transition taking place in whole films with surface or interface phase transition cannot be separated, and due to that PT at different temperatures from those detected for single crystals, for example, can be observed Therefore, the next step of this investigation will be study of the phase transitions by other methods like specific heat measurements and X-ray.

6.2 Lead zirconium titanate $\text{Pb}(\text{Zr},\text{Ti})\text{O}_3$

6.2.1 XRD

The representative XRD results for the majority of the films are presented in Fig. 6.2.1. All films were fully crystallized. Some differences were observed for the films made with same sol but with different thermal profile. To illustrate, the films made with AcOH/MeOH sol having all layers crystallized together (LCT) exhibit predominant (111) orientation with few minor, low intensity peaks representing (100), (110), and (112) orientations (Fig. 6.2.1.a). The films made with the same sol but, where each layer was completely crystallized before the deposition of the new layer, has mixed orientation of (100)/(001), (111), and (200)/(002) peaks. The difference in orientation for films made

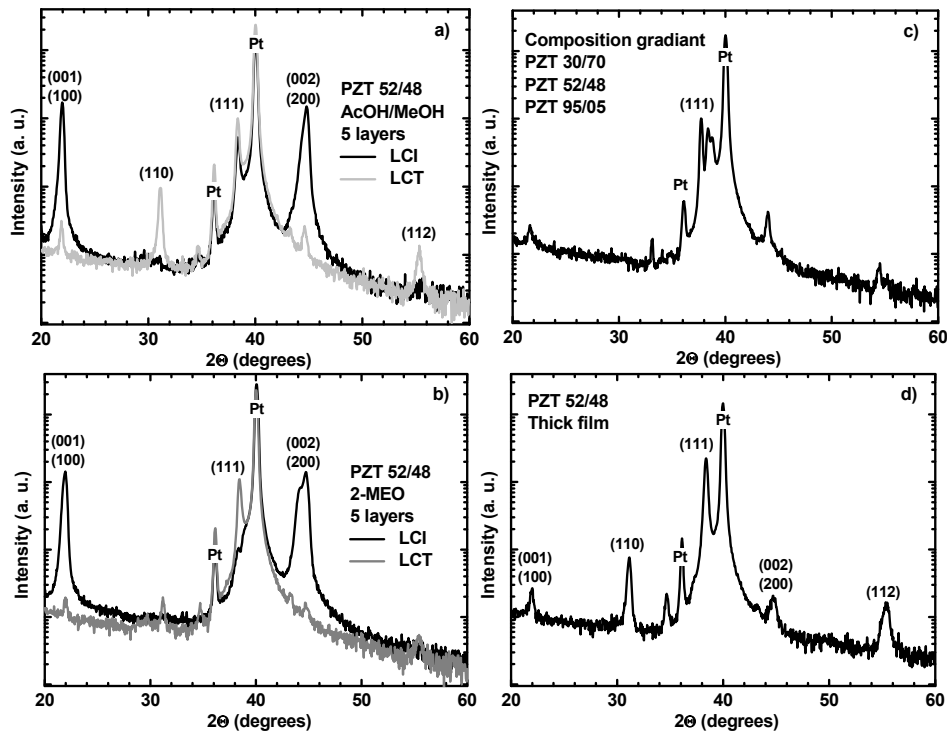


Fig. 6.6.1. The XRD of the samples from Tab. 1. Comparison of x-ray diffractograms for 5 layers a) AcOH/MeOH films and b) 2-MEO films fabricated using two different thermal profiles. c) XRD diffractogram for the compositional gradient sample Nr. 1 in Tab. 1, and d) XRD diffractogram of 4 layers thick PZT 52/48 film Nr. 6 from Tab. 1.

with 2-MEO sol was even more pronounced (Fig. 6.2.1.b). The LCI-film showed pure (100)/(001) orientation whereas the LCT-film showed pure (111) orientation. Thus, it can be concluded that the orientation relates to a greater extent to the processing method than to the sol composition. In the XRD diffractogram of the compositional gradient sample (Fig. 6.2.1.c) only peak group of (111) orientation was found. The (111) peaks stem from the orthorhombic (antiferroelectric) phase, the tetragonal phase and the rhombohedral phase from the different PZT compositions. The thick PZT 52/48 film (Fig. 6.2.1.d) was strongly (111) orientated, but had some minor (100), (110) and (112) peaks detected.

6.2.2 Optical properties

Optical properties of the host material for each film (the table of the samples Tab. 5.2 can be found in chapter “5.2 Lead zirconium titanium oxide $\text{PbZr}_x\text{Ti}_{1-x}\text{O}_3$ ”; Fig. 6.2.2 and 6.2.3) were evaluated by fitting experimental ellipsometric data by simple model substrate/interface/film with thickness non-uniformity/top layer (Fig 6.2.1.ab). The fitting parameters - thickness of the interface between bottom electrode and film, thickness of the film d , thickness of the top layer (roughness), thickness non-uniformity, and fitting parameters of CLO (A_n – amplitude (strength) of each oscillator (eV), E_{nn} – centre energy of each oscillator (eV), B_{rn} – vibration frequency of each oscillator (eV), E_{gn} – band gap energy of each oscillator (eV), E_{pn} , E_{tn} , E_{un} – characterize peak position and form of ε_2), are summarized in Tab. 6.2.1. Then film was considered to be inhomogeneous by dividing film into the layers, and layers into the slices. The amount of layers coincides with the amount of the layers during sol-gel processing of thin films. Each layer was divided into the 25 slices. Remarkable improvement of the fit, considering film to be with the depth profile, was found for the films of group Nr 1, 2, 3, 5, and 8 (MSE decreased 1.5 - 2.5 times). The improvement of the fit during simple graded model is shown in Fig. 6.2.1cd. For other films the graded model did not gave any improvement, except of the PZT 52/48 1 layer thin film from group Nr 4 (Fig. 6.2.5c), what can be caused by the stresses in the single layer film. The model of porosity and grain boundaries did not gave any improvement to the fit to any of the films, approving the graded model as the only one solution of the experimental data fit. Because Pt bottom electrode optical properties were evaluated, the influence of inaccurate optical properties of the substrate to fit SE data of the PZT thin films was eliminated.

PZT 52/48, AcOH/MeOH solvent (group Nr 4, 5, 6, 9 and 10)

Gradient of the optical properties was found in the samples of group Nr. 5 from 2 till 4 layers (Fig. 6.2.4a). These PZT 52/48 thin films were made by crystallizing each layer individually.

The simple model, where film is considered to by as a single continues layer, where refractive index exponentially increase or decrease with the thickness, did not gave any improvement to the fit. The model was compound, where films were assumed to be with gradient profile changing from layer to layer (Fig. 6.2.4a). The gradient differs from 2 layers film to 3 layers and son on till 5 layers thin film after recurrent annealing of already crystallized layer. If we look on the optical properties of these samples (Fig. 6.2.3a), they vary from film to film, too. For all films the 1st layer has no gradient, only at the interface to the next layer there is a sharp jump of $n(d)$. The $n(d)$ decreases thought the 2nd layer for 2 layers film. The 3^d layer has slight increase of $n(d)$, but after adding the 4th layer (in this layer $n(d)$ slightly increase), the 2nd and 3^d layers converge and $n(d)$ has the same shape like in the case of 2nd layer of 2 or 3 layers film. By adding the 5th layer, the shapes of $n(d)$ do not change in the layers from 1 till 4.

Due to the increase of the amount of fitting parameters, the error of the exponent and variation values increases (Tab. 6.2.1), as the result we can not say exactly by what quantity $n(d)$ increases or decreases for the films with the more then 2 layers, or either there is some slight jump of $n(d)$ from, e. g., the 2nd to 3^d layer, but confidence of the fit

Tab. 6.2.1. The fitting parameters - thickness of the interface between bottom electrode and film (nm), thickness of the film d (nm), thickness of the top layer (roughness, nm), thickness non-uniformity (%), fitting parameters of single or double CLO (A_n – amplitude (strength) of each oscillator (eV), E_{nn} – centre energy of each oscillator (eV), B_{rn} – vibration frequency of each oscillator (eV), E_{gn} – band gap energy of each oscillator (eV), E_{pn} , E_m , E_{un} – characterize peak position and form of ϵ_2), and descriptive quantity of the gradient – value of the exponent and variation of the refractive index (%).

Nr	Interf. (nm)	d (nm)	Top (nm)	Unif. (%)	A (eV)	E_n (eV)	B (eV)	E_g (eV)	E_p (eV)	E_r (eV)	E_u (eV)	Exponent	Variation (%)
1	0.3	693 (83; 296; 314)	9.8	1.5	80.78	5.24	7.78	3.53	1.08	0.33	0.17	29±8	26±6
					2.42	4.39	36.07	2.56	1.69	0.18	100	99±37	-9.6±0.9
2	0.9	212	3.2	2	82.23	5.38	7.61	3.45	0.81	0.38	0.22	0.51±0.05	5.9±0.3
3	2.6	387	2.6	1.7	52.89	7.14	7.67	3.21	0.64	0.22	0.23	99±12	45±4
4	0	108	5.5	3.6	55.52	6.59	7.75	3.39	0.45	0.18	0.51	0.06±0.01	33.8±3.5
					61.33	5.48	6.64	3.39	0.87	0.37	0.12	-	-
					9.49	10.46	3.13	2.02	0.37	0	1.71	-	-
					56.94	5.19	5.42	3.41	0.91	0.32	0.12	-	-
					13.52	13.60	3.42	2.02	0.46	0.09	0.72	-	-
5	0	107	6.7	1.5	100.36	5.07	7.48	3.09	1.84	0.37	0.56	-	-
					124.98	4.08	7.48	3.33	1.38	0.22	0.70	34.58±2.37	-45±3
					94.32	4.71	5.44	3.40	1.31	0.19	0.30	0.24±0.02	-11.63±1.13
					94.32	4.71	5.44	3.40	1.31	0.19	0.30	26±4	-32.15±1.56
6	0	212	2.5	1.5	124.98	4.08	7.48	3.33	1.38	0.22	0.70	0.35±0.22	-5±3
					94.32	4.71	5.44	3.40	1.31	0.19	0.30	0.01±0.01	44±5
					94.48	4.89	5.54	3.47	1.24	0.22	0.24	0.12±0.01	-28.20±1.62
					94.48	4.89	5.54	3.47	1.24	0.22	0.24	21±2	1.6±0.4
					94.48	4.89	5.54	3.47	1.24	0.22	0.24	29±2	-47±2
7	0	107	6.7	1.5	100.36	5.07	7.48	3.09	1.84	0.37	0.56	52±5	-37±3
					100.36	5.07	7.48	3.09	1.84	0.37	0.56	0.09±0.01	-22±1
					100.36	5.07	7.48	3.09	1.84	0.37	0.56	0.06±0.02	7±1
					100.36	5.07	7.48	3.09	1.84	0.37	0.56	-	-
					100.36	5.07	7.48	3.09	1.84	0.37	0.56	-	-
8	0	107	6.7	1.5	100.36	5.07	7.48	3.09	1.84	0.37	0.56	-	-
					100.36	5.07	7.48	3.09	1.84	0.37	0.56	-	-
					100.36	5.07	7.48	3.09	1.84	0.37	0.56	-	-
					100.36	5.07	7.48	3.09	1.84	0.37	0.56	-	-
9	0	107	6.7	1.5	100.36	5.07	7.48	3.09	1.84	0.37	0.56	-	-
					100.36	5.07	7.48	3.09	1.84	0.37	0.56	-	-
					100.36	5.07	7.48	3.09	1.84	0.37	0.56	-	-
					100.36	5.07	7.48	3.09	1.84	0.37	0.56	-	-
					100.36	5.07	7.48	3.09	1.84	0.37	0.56	-	-
10	0	107	6.7	1.5	100.36	5.07	7.48	3.09	1.84	0.37	0.56	-	-
					100.36	5.07	7.48	3.09	1.84	0.37	0.56	-	-
					100.36	5.07	7.48	3.09	1.84	0.37	0.56	-	-
					100.36	5.07	7.48	3.09	1.84	0.37	0.56	-	-
					100.36	5.07	7.48	3.09	1.84	0.37	0.56	-	-

is satisfactory to consider about the direction of $n(d)$ gradient, for example, whether it increase or decreases form the bottom electrode to the top of the 1st layer, and from the 1st layer to 2nd layer and so on. Each crystallization of the added layers causes pronounced changes in the optical properties of the films of group Nr. 5. Smaller change of the complex refractive index spectral dependence was found for PZT 52/48 thin and especially for the thick films, which layers were crystallized all together.

No depth profile of refractive index was found for PZT 30/70 (group Nr 9) and 95/05 (group Nr 10) thin films. Optical properties of these films are given in Fig. 3. In this graph also PZT 52/48 thin film (made on the same conditions like PZT 30/70 and 95/05) optical properties are shown. Refractive index remarkably decreases and optical band gap energy (Tab. 6.2.1) slightly increases with decrease of Ti/Zr ratio (Fig. 6.2.6f). It is in good agreement with other works in different compositions of PZT thin films [9, 10, 97]. If we extrapolate this fact to the evaluated gradient profile of PZT 52/48 (Nr 5), then we can explain increases and decrease of $n(d)$ with change of Zr/Ti ratio in the layer, what can be caused due to the crystallization of each layer separately contributing diffusion of elements in the film.

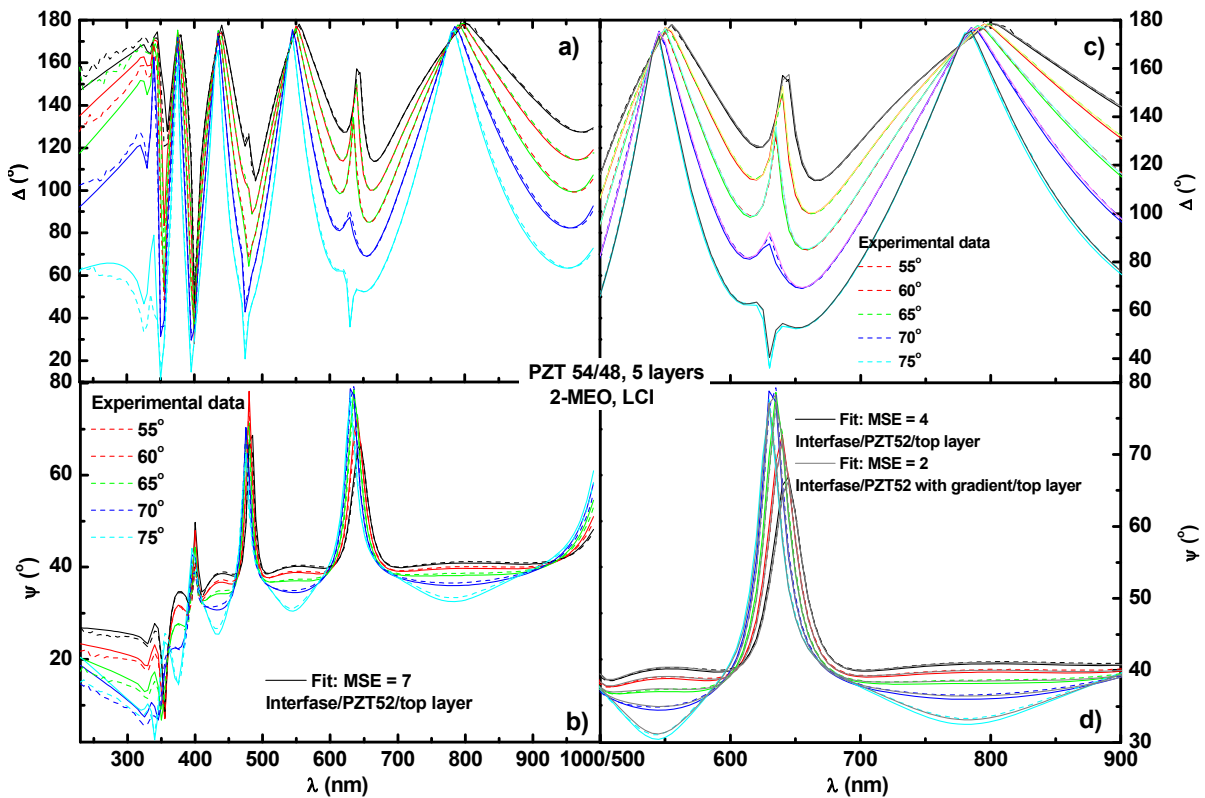


Fig. 6.2.1. Experimental (discontinuous line) and modeled (continues line) ellipsometric angles ψ (b, d) and Δ (a, c) at the whole spectral region of 230 – 1000 nm to estimate the optical properties of the host material of the PZT 52/48 (5 layers, made by 2-MEO sol, LCI), thickness of the film, roughness, interface and thickness non-uniformity (a, b); and at the spectral region of 500 – 900 nm by applying exponential graded model (c, d).

PZT 52/48, 2-MEO solvent (group Nr 7 and 8)

Refractive index depth profile was found for the PZT 52/48, which layers were crystallized individually (group Nr. 8): refractive index exponentially increases with the tetchiness (Fig. 6.2.4b). There can be several reasons of that: 1) stresses in the film, 2) increase of Ti or decrease of Zr in direction to the film surface, and 3) increase of excess

Pb. The fit was satisfactory considering the film to be as a single continuous layer, irrespective to the amount of layers during the film creation. As the result the confidence (Tab. 6.2.1) regarding to the direction of $n(d)$, the quantity of increase of $n(d)$ is with very high validity. But unfortunately it is not possible to say whether there are some “breaks” of the $n(d)$ at the interfaces between PZT thin film layers. Such model was also satisfactory to the fit of experimental data, but due to the increase of fitting parameters and decrease of confidence, the simple model has advantage. Exception certainly is the case of PZT 52/48 of grope Nr 5 described above, where simple model did not gave any improvement to the fit, what is opposite to this case of PZT 52/48 of grope Nr 8.

The $n(d)$ slightly decreases with increase of amount of layers in film (Fig. 5b). It is in a good agreement with the evaluated optical properties of the host material of PZT 52/48 of grope Nr 8 (Fig. 6.2.3b): refractive index also slightly decreases (starting from 2 layers) with increase of layers. Refractive index of the Nr 8 is higher then of the Nr 7 samples (Fig. 6.2.3b). The same was detected for the films or Nr 4 and 5 (Fig. 6.2.3a). If each layer is crystallized individually, we may expect the increase of crystallinity of the film and as the result to have higher refractive index. But if we compare samples made by different sols, but crystallized in the same way (compare group of samples with Nr 4, 7, and 5, 8), refractive index is higher for the films made by AcOH/MeOH sol that for the film made by 2-MEO sol (Fig. 6.2.3cd).

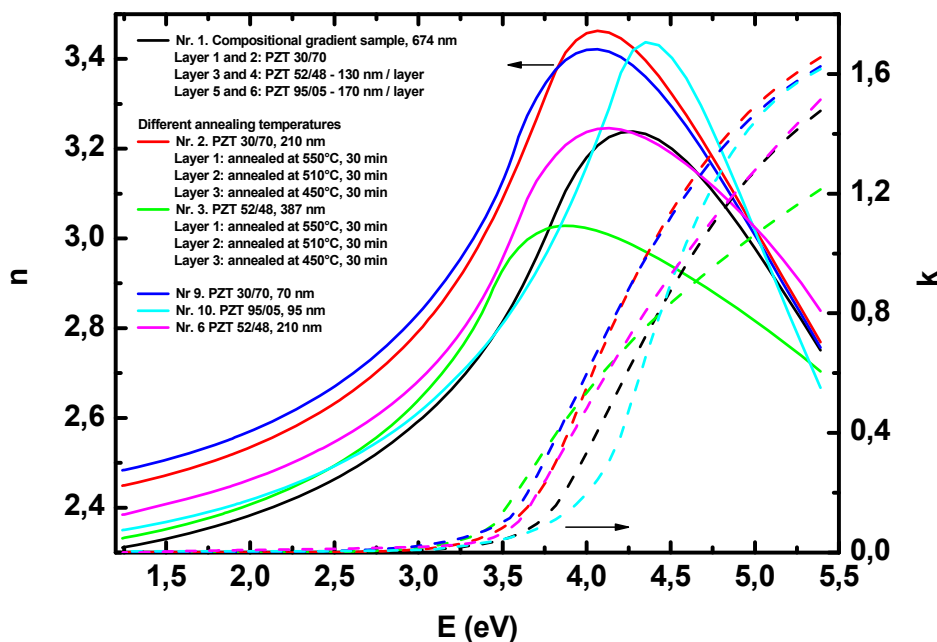


Fig. 6.2.2. Optical properties of the host material of samples Nr. 1 – compositional gradient, Nr. 2 – PZT 30/70 of 3 layers crystallized at the different temperatures, Nr. 3 - PZT 52/48 of 3 layers crystallized at the different temperatures, in comparison with the sol-gel thin films PZT 30/70, PZT 52/48 and PZT 95/05.

Composition graded PZT thin films; films crystallized at different temperatures (group Nr. 1, 2, 3)

These films were specially made to examine spectroscopic ellipsometry: is it useful for the detestation of the optical properties difference thought the layer to layer in the PZT thin films, and can we evaluate similar depth profiles regarding to the experience with films described above.

The composition graded PZT thin film was made in the similar conditions like PZT 52/48 of grope Nr 4, 6, 9 and 10, where no gradient was detected by SE. While

fitting experimental data with simple model substrate/homogenous film/ top layer, quite high MSE was found and optical properties of the host material were evaluated (Fig. 6.2.3).

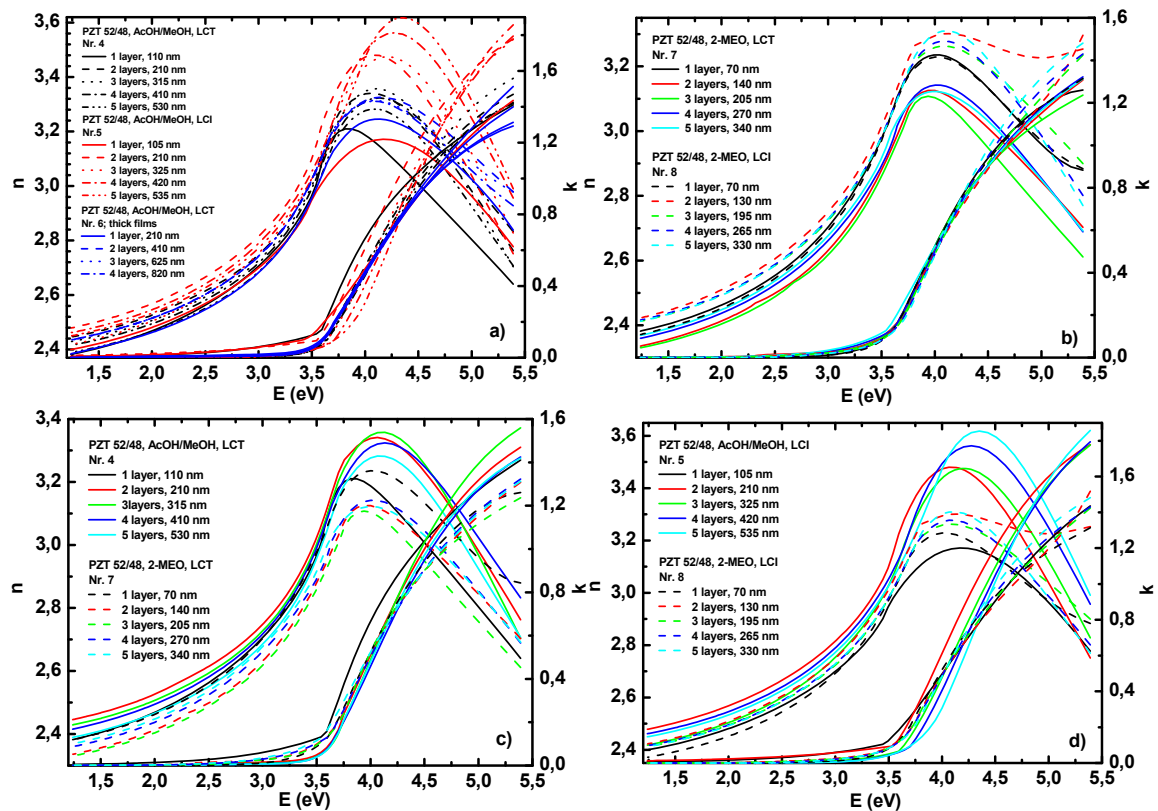


Fig. 6.2.3. Samples with different thicknesses of the group a) Nr 4, 5 and 6, b) Nr 7 and 8, and for comparison of c) Nr 4 and 7, and d) Nr 5 and 8.

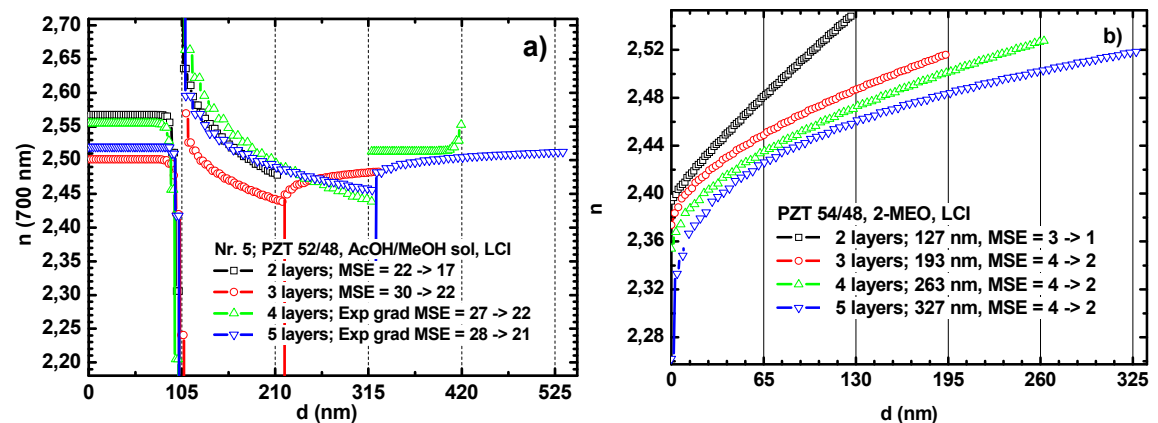


Fig. 6.2.4. Depth profile at the 700 nm of the samples of the group a) Nr 5, and b) Nr 8 with different number of layers.

Such simple model did not describe our sample because first two layers are PZT 30/70, next two are PZT 52/48 and last two are PZT 95/05. As it was evaluated PZT with different Zr/Ti ratio has different optical properties (Fig. 6.2.2). Inasmuch as during film fabrication, approximate thickness of each layer was known, the film was divided into 3 layers from the bottom to the top with thickness ~ 100 , 300 and 300 nm, and already evaluated optical properties of single or double layer of PZT30/70, 52/48 and 95/05 was used to describe optical characteristics of these 3 layers of the sample Nr 1. The fit slightly

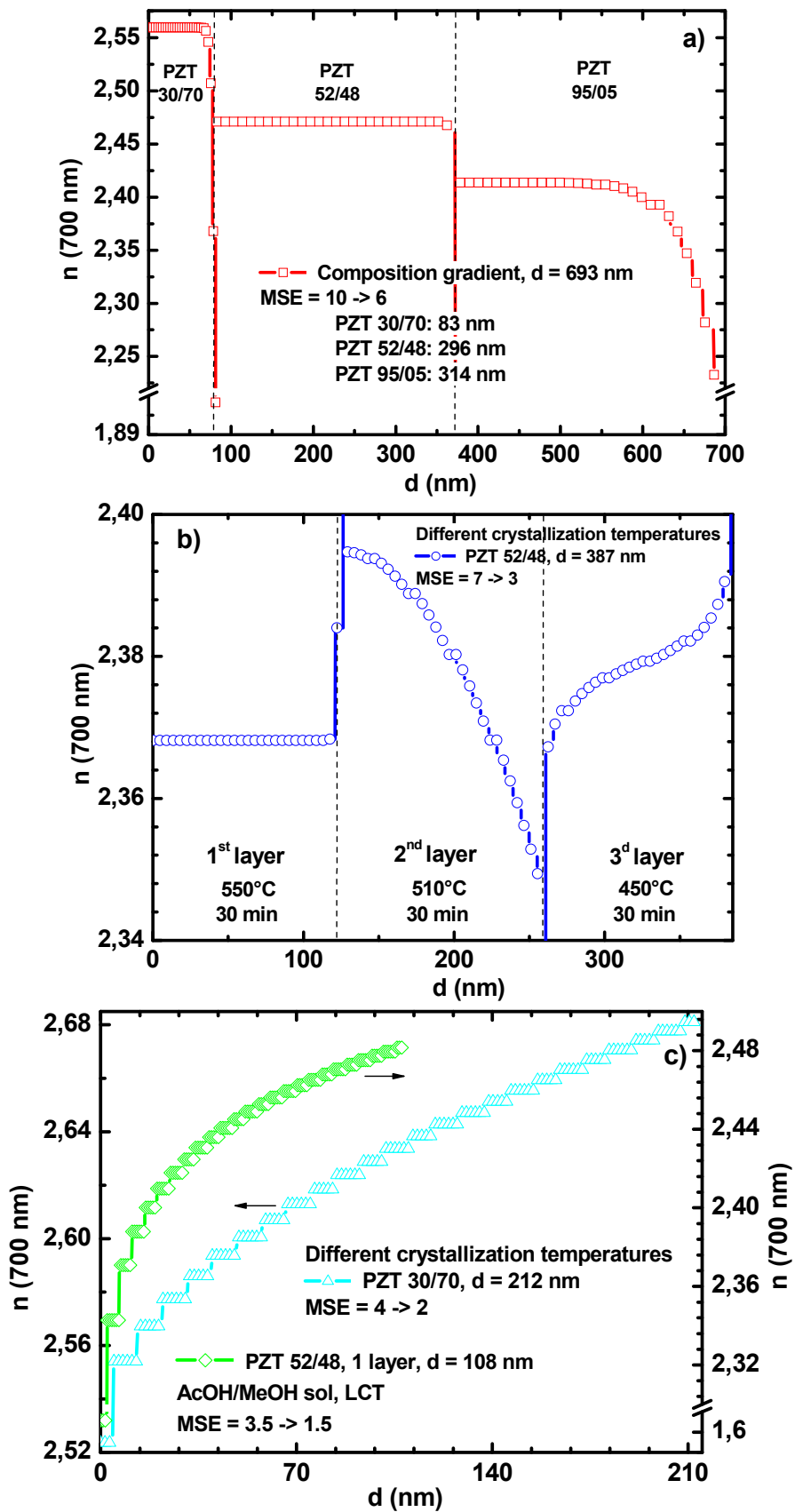


Fig. 6.2.5. Depth profile at the 700 nm of the sample a) with composition gradient – first two layers are PZT 30/70, then PZT 52/48, and last two PZT 95/05 (Nr 1), b) PZT 52/48 with layers crystallized at the different

improved. Then each layer was assumed to be with the gradient, and MSE decreased almost 2 times. The depth profile of refractive index of graded PZT thin film is given in Fig. 6a. There is no gradient of refractive index from the bottom to the almost top of the 1st layer of PZT 30/70, and then there is jump of n at the interface to the 2nd layer of PZT 52/48. Again no gradient through the 2nd layer till the top and jump of n at the interface to the 3^d layer of PZT 95/05. The pronounced gradient was found for the PZT 95/05 at the last 100 nm close to the surface: refractive index decreases with increase of the thickness. Such gradient can be explained with a notable increase of Zr/Ti ratio in this region. But anyhow this is very significant result according to the fact that no gradient was found for the PZT 30/70 and PZT 52/48 layers in sample Nr 1 as it was for other films (Nr 4, 6, 7 and 9) made on similar conditions. This result approves that films of one composition, which layers crystallized all together have no gradient. Small jumps of n at the interfaces can be caused by the slight difference in the lattice parameters and expansion coefficients of different Zr/Ti ratio of PZT layers.

Depth profile of n was found also for the PZT 52/48 (sample Nr 2) and PZT 30/70 (sample Nr 3), which layers were crystallized individually at the different temperatures (Tab. 5.2). The $n(d)$ of PZT 52/48 is changing similar (Fig. 6.2.5b) like gradient of the PZT 52/48 with three layers from group Nr 5 (Fig. 6.2.4a): the 1st layer $n(d)$ is constant, the 2nd layer $n(d)$ decreases, and the 3^d layer $n(d)$ increases. The only difference is that amount of n increase or decrease is smaller for the sample, which annealed at the different temperatures. Depth profile of PZT 30/70 (Fig. 6.2.5c) is similar with the gradient of 1 layer PZT 52/48 of group Nr 4 (Fig. 6.2.5c), and five samples of group Nr 8 (Fig. 6.2.4b). Probably due to the different structure of PZT 30/70, the form of the gradient can differ from those detected for PZT 52/48, made at the same conditions.

6.2.3 Discussion

From estimating the optical properties of the PZT thin films it was found, that refractive index and extinction coefficient slightly varies from the film to film with different amount of layers (Fig. 6.2.6de). If thickness is higher than ~ 400 nm, then this difference vanishes. So, with increase of amount of the layers, and crystallizing layers together, contribute to the forming of the homogenous film with no optical gradient and no variation of refractive index between films with different thicknesses.

The optical band gap almost keeps constant for different amount of the layers for samples of group Nr 4 and 6 (Fig. 6.2.6c). Remarkable increase of the E_g with increase of thickness was found the samples of group Nr 5, where layers had no final annealing. Smaller dependence of E_g with thickness was found also for the samples made by 2-MeO sol. As a conclusion the films with more "stable" refractive index and band gap energy can be made with AcOH/MeOH sol, when layers are crystallized together, with the thickness greater than ~ 300 nm.

A higher value of roughness for the samples of group Nr 4 was established (Fig. 6.2.6 b), what is due to the drying cracks in the films, observed by optical microscope. The roughness has tendency to decrease with increase of the thickness for other thin films.

The XRD results showed that these films, which have optical gradient, exhibit mixed orientation of (100)/(001), (111), and (002)/(200) peaks (Fig. 6.2.1a). It should be mentioned that the layers of those films were crystallized individually. The individual crystallization of the layers contributes to interface forming between layers in the case of films of group Nr 5 due to the missing final annealing. But in case of films of group Nr

8, where layers were finally annealed all together, the form of the gradient is much smoother - increase of n from the bottom to the top of the film.

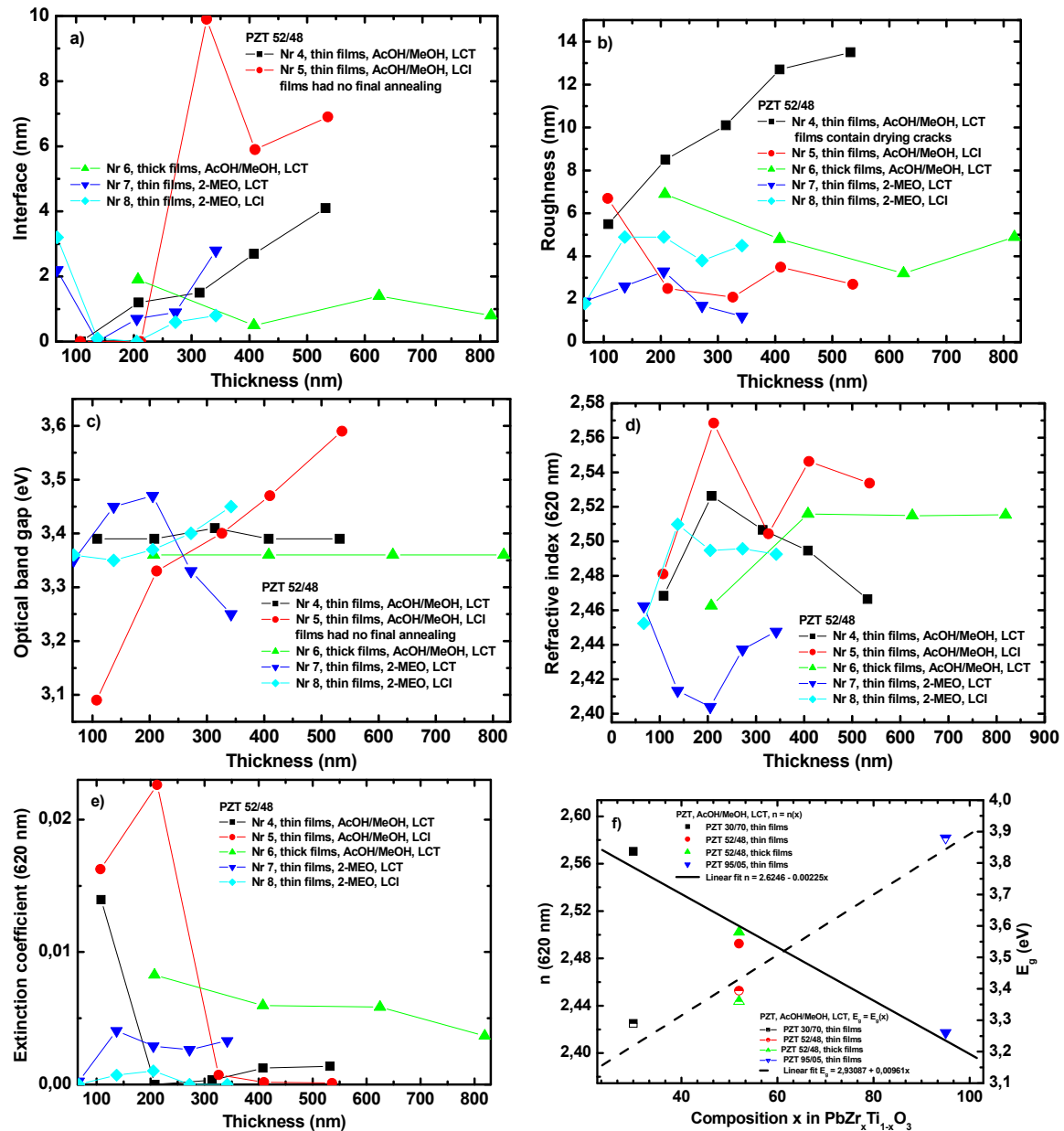


Fig. 6.2.6. Thickness dependence of a) interface, b) roughness, c) optical band gap E_g , d) refractive index n at 620 nm and e) extinction coefficient k at 620 nm for five groups of samples Nr 4, 5, 6, 7 and 8 (see Tab. 5.2). Composition x in $\text{PbZr}_x\text{Ti}_{1-x}\text{O}_3$ dependence of f) $n(620 \text{ nm})$ and E_g for PZT samples made at the same conditions with the same sol.

Why there is difference of n between the same group of samples, but with varies amount of layers? It is well known, and it was also found from the optical results in this work, that the thicker the films, the better the quality. There were many investigations, experimental and theoretical, on the thickness dependence of film properties. The thickness dependence mainly is attributed to the substrates influence on the films properties due to the lattice mismatch. Decrease of film thickness leads to an increase in leakage current due to defects (unless thicknesses approaching tunneling distances are used). But, the thicker films, the higher voltages for operation require. So, it is important to determinate the optimum film thickness for optimal device performance. But, in order

to increase the memory storage density in integrated circuits, the single element size should be as small as possible. Where the fundamental size limit at which ferroelectricity still exists, considering that ferroelectricity represents a cooperative phenomenon? According to this there is some experimental and theoretical research already [30, 31, 120, 170–174]. The thickness of perovskite oxide thin films significantly affects a wide range of film properties [18, 175–182]. The grain size was found to strongly affect the film properties, too [19, 183, 184].

Films with grain sizes of ~ 60 - 150 nm were obtained by annealing the as-grown PZT samples on Pt/Ti/SiO₂/Si at different temperatures [184]. It was found that PZT films with smaller grain size, exhibited better fatigue properties [184], and it was accounted that a smaller fraction of the grains touches the Pt electrodes since it is believed that one of the reasons for fatigue is the pinning of domain walls by space charge or charged point defects near the Pt electrodes [184]. Similar fatigue dependence on grain size was observed also in [183]. But one moment have to be taken in mind: the permittivity decreased with decrease of grain size, what is attributed to lower mobility of domain walls in films with smaller grain sizes. There were considerable debates already on the critical thickness of the ferroelectric films, below which ferroelectricity disappears.

First-principles calculations on a ferroelectric-electrode interface showed that BaTiO₃ thin films between two metallic SrRuO₃ (SRO) electrodes in short circuit lose their ferroelectric properties below a critical thickness of about ~ 2.4 nm (six unit cells), which suggests the existence of a lower thickness limit for ferroelectricity [174]. In this work it was found that the thickness of the interface layer differs from film to film with different amount of layers and depends on the way, how films was crystallized. The interface between Pt and the film was found to increase from 0 to 4 nm with increase of amount of layers from 1 to 5 for samples of group Nr 4 (Fig. 6.2.6a). Much smaller thickness (just ~ 0.5 - 2 nm) of the interface was found for samples of group Nr 6 (thick films) in comparison with group Nr 4, although the crystallization of the films was similar. The highest values of the interface thickness (~ 6 – 10 nm) were found for the samples with 3 - 5 layers of grope Nr 5, which had no finale annealing. All other films showed interface not greater than 3 nm. The reason for the disappearance of the ferroelectric instability and appearance of the interface can be explained by the depolarizing electrostatic field caused by dipoles at the ferroelectric-metal interfaces [174].

On the other hand, synchrotron x-ray study of atomically smooth PbTiO₃, grown on SrTiO₃, as a function of temperature and film thickness, showed that the room temperature ferroelectric phase is stable for thicknesses down ~ 1.2 nm (3 unit cells) [170]. These results imply that no thickness limit is imposed on practical devices by an intrinsic ferroelectric size effect since in thinner films the constituent elements are reconstructed at the surface or constrained *b* chemical bonds formed with the SrTiO₃ substrate.

According to the thickness dependence, it was found for the PLD PZT thin films with metallic electrodes: an increase of E_c was observed with decreasing thickness. The charge injection model was used to explain the observed increase of E_c with decreasing ferroelectric layer thickness [172]. But when the oxide electrode La_{0.5}Sr_{0.5}CoO₃ (LSCO) was used, no thickness dependence of E_c and a good endurance (up to 10¹¹ ferroelectric cycles) was observed for both epitaxial and textured capacitors [172].

Epitaxial PMN-PT thin films, prepared by PLD on (100) LaAlO₃ substrates, showed a systematic decrease in the phase transition temperature (from around 250°C to around 60°C) as the film thickness increased from 100 to 400 nm. The relative dielectric constant (ϵ_r), measured at room temperature and at 10 kHz, increased from 300 to 2000,

and the piezoelectric coefficient d_{33} increased by almost an order of magnitude [175] with increase of the film thickness. This behavior may be closely related to the decrease in defect concentration resulting from grain growth as the film thickness is increased [183].

The effect of thickness on the microstructure and domain formation of ferroelectric $\text{PbZr}_{0.2}\text{Ti}_{0.8}\text{O}_3$ (PZT20) films with nominal thickness of 60 to 400 nm, grown PLD on (001) LaAlO_3 substrates with LSCO electrodes, was studied by Nagarajan [175]. X-ray diffraction measurements showed a strong dependence of the film domain structure on the film thickness. It was found that the films relaxed via the formation of a -domains, the fraction of which increased with the film thickness. The c -axis lattice constant of PZT20, deduced from the (002) reflection, decreased with an increase of film thickness due to relaxation of internal stresses by polydomain formation and approached the bulk value of ~ 0.413 nm for films thicker than 300 nm. TEM images of cross-section revealed that the a -domain fraction and period increased with the film thickness. The relaxation of misfit strain in the films was accompanied by systematic changes in the polarization properties as well as the switching fields, quantified by the coercive field and the activation field. Nagarajan [175] observed the effect of thickness scaling in (001) epitaxial PZT20/SRO heterostructures. The 15, 50, and 160 nm thick PZT20 films investigated showed well saturated polarization loops down to 15 nm with remanent polarization (P_r) of about $75 \mu\text{C}/\text{cm}^2$ and the coercive field increased with decreasing thickness. It was suggested that the nature of the electrostatics at the film-electrode interface plays a significant role in determining the behavior.

Piezoelectric properties of different submicron size capacitors with PZT50 and PZT20 grown on SrTiO_3/Si and SrTiO_3 substrates, respectively, were calculated taking into account the intrinsic strain (strain induced by substrate constraint, substrate local deformation, and electrode deformation) by Li [185]. It was found that the local deformation of the substrate can significantly reduce the effective piezoelectric coefficient d_{33} .

Stolichnov [186] proposed a model providing a qualitative description of the influence of film thickness on the polarization hysteresis loop, where the depolarization phenomena and local charge injection at thin film-electrode interface (interface charge injection model) were suggested to be a key for the dependence of the ferroelectric behavior on the film thickness. Based on the model, a possibility to influence the polarization switching properties by modifying the conductive properties of thin film-electrode interface was suggested. Experimentally, Stolichnov [186] introduced a thin oxide layer (RuO_2) to dope the film-electrode interfacial region in Pt/PZT/Pt capacitors (to cause the modulation of the conductivity in the nearby electrode layer), and observed a significant decrease of the coercive field (E_c).

In this work it was observed that, with increase of the thickness from $\sim 60 - 400$ nm, the interface layer increase and there is slight difference in optical properties of the films. It means that just the depolarization phenomena at the interface can not be responsible for the whole difference in optical properties because the influence of the interface is separated during calculation of the n and k of the film. As the result, the one would expect that n and k is not changing with the thickness afterwards, but observation is opposite. During polarization hysteresis loop measurements, the influence of interface is very difficult to separate with proper experiment and model calculations. And the differences in loops (and other SE properties) are explained by the possible interface, what influences the electrical measurements. It is more likely that difference in n and k with the thickness in these sol-gel PZT films is due to the different structure of the film, what causes film stresses and strains, and not interfaces.

The discussion made above can explain the thickness dependence of optical properties, but it can not explain the n profile in the films with layers annealed individually. There are theoretical works, which show that the polarization profiles have a strong dependence on a film thickness: polarization is homogeneous in the greatest part of thick film besides the small regions in vicinity of the film boundaries, while it is completely inhomogeneous in thin enough films. The degree of polarization inhomogeneity increases with thickness decrease [120]. As the result, in the case of the graded samples (with layers annealed individually), there can be several explanations: individual annealing of the layers caused 1) stresses in the films, which caused polarization inhomogeneity, and/or 2) chemical element diffusion in the film during crystallization process.

The manuscript is now under preparation [38a] to publish these scientifically and technologically interesting and important results.

7. Summary

Spectral ellipsometry (SE) was successfully applied for optical and thermo-optical studies of the PLD NaNbO_3 and sol-gel $\text{PbZr}_x\text{Ti}_{1-x}\text{O}_3$ ($x = 30, 52$ and 95) thin film deposited on $\text{Si/SiO}_2/\text{Ti/Pt/SrRuO}_3$, Si/SrRuO_3 and $\text{Si/SiO}_2/\text{Ti/Pt}$ substrates.

The complex refractive index of the host material and depth profile of the real part of refractive index of the NN films was established. Refractive index of the host material as the function of the thickness was found to be almost constant from 150 till 250 nm, and increase from ~ 250 -300 nm. More deep gradient calculations revealed also refractive index decrease near the substrate what can be explained by the stresses in the films.

Behavior of the refractive index n and extinction coefficient k at fixed wavelength 300 nm, and optical band gap E_g in the wide temperature range (5-820 K) of NN thin films were investigated by the SE. Totally five anomalies in the $n(T)$, $k(T)$ and $E_g(T)$ dependencies were found. The corresponding temperatures of the increase/decrease of the $n(T)$ and $k(T)$ and jumps of the $E_g(T)$ were observed at the 225, 643 (645), 723 (723), 750, and 794 (788) K temperatures. Established anomalies agrees well with the phase transition (PT) temperatures of the $N \rightarrow P$, $P \rightarrow R$ and $R \rightarrow S$, $S \rightarrow T1$ transitions of the NN single crystals and ceramics studied by X-ray, DTA and other techniques. Different PT temperature of $N \rightarrow P$ and unusual PT at 718 (723) K were found and related to various defects and possible coexistence of different phases in the films. The inhomogeneity of the film is founded with the evaluated optical depth profile of the films, as well as with a shifting and broadening of some Raman modes.

The SE studies of sol-gel PZT thin films showed that n increases and E_g decreases with decrease of Zr/Ti ratio. Higher values of n and lower values of k were established for the PZT films made by AcOH/MeOH solvent. No change of n and E_g with the thickness was found for films thicker then 300 nm. The higher values of the interface between bottom electrode and the film were found for the samples, which had no final annealing. With increase of amount of the layers, and crystallizing layers together, contribute to the forming of the homogenous film with no optical gradient and no variation of refractive index between films with different thicknesses.

Depth profile of the refractive index was established for PZT 52/48 thin films with layers crystallized individually irrespective to the chemical solvent, PZT 52/48 and PZT 30/70 with layers annealed individually at the different temperatures, and composition graded PZT thin film, where first two layers are PZT 30/70, then PZT 52/48 and the last two are PZT 95/05. The individual crystallization of the layers contributes of interface forming between layers in the case of films, which had no final annealing. SE investigations evaluated that the chemical synthesis routes are not responsible for the gradient appearance: it appears from the crystallization process.

These investigations showed that SE is effective technique for the PT detection in thin films. SE showed its efficiency in nondestructive and noncontact mode optically evaluates thin films inhomogeneity.

8. Conclusion

As a conclusion the following main aspects of this work can be summarized:

1. NaNbO_3 :

- 1) Polycrystalline NN thin films with orthorhombic structure were successfully made by PLD;
- 2) For the first time, of the author's knowledge five anomalies at the $n(T)$ and $E_g(T)$, corresponding to the five phase transitions, were observed in NN thin films by SE, from which three phase transition temperatures very well agree with those reported for the NN single crystals; these investigations showed that SE is effective technique for the phase transition detection in thin films;
- 3) For the first time, of the author's knowledge, the thermo-optical coefficients of the NN thin films of all five phases were evaluated;
- 4) For the first time, of the author's knowledge, the refractive index and extinction coefficient at the broad spectral range (250-1000 nm) of the bottom electrode SrRuO_3 and NN thin films were evaluated;
- 5) The slight shift of other phase transition temperatures are connected with the inhomogeneity of the film;
- 6) By SE it was found, that NN thin films has the (i) thickness dependence of the optical properties of the host material and (ii) depth profile of the refractive index;
- 7) Refractive index exponentially increases from the bottom to the surface of the the film; such behavior can be explained by the stress and strain distribution in this gradient structure.

The studies made on NN thin films have a practical importance for the further applications of the NN as a lead-free piezoelectric materials, for potential application in surface acoustic wave, optical wave guiding, and frequency doubling devices, working at the extreme conditions such as high temperatures

2. $\text{Pb}(\text{Zr},\text{Ti})\text{O}_3$:

- 1) Epitaxial $\text{PbZr}_x\text{Ti}_{1-x}\text{O}_3$ (PZT) thin films ($x = 30, 52, \text{ and } 95\%$) were successfully made by sol-gel with different thicknesses, using AsOH/MeOH and 2-MEO solvents, and two ways of crystallization – all layers together and each layer separately;
- 2) For the first time, of the author's knowledge, the optical gradient and thickness dependence of complex refractive index, interface, roughness, optical band gap were studied for sol-gel PZT thin films by SE;
- 3) It was found that the thickness of the interface and optical band gap energy dramatically increases with increase of the PZT 52/48 film thickness for the samples

made by AsOH/MeOH sol and which layers were crystallized separately (with no final annealing);

- 4) The thick film samples made by AsOH/MeOH sol and with layers annealed together had no change of the complex refractive index, optical band gap and thickness of the interface with the film thickness;
- 5) The thicker films and crystallizing all layers together contribute of the homogenous film forming;
- 6) Higher values of refractive index was evaluated for the films made by AsOH/MeOH sol in comparison with the films made by 2-MEO sol;
- 7) Optical gradient were established only for the PZT 52/48 thin films, which layers where crystallized individually, as well for the films which layers where annealed at different temperatures;
- 8) The chemical synthesis routes are not responsible for the gradient appearance: it appears from the crystallization process, what causes (i) stresses in the films and/or (ii) chemical elements diffusion in the films; SE showed its efficiency in nondestructive and noncontact mode optically evaluates thin films inhomogeneity.

Due to the broad technical applications of sol-gel PZT thin films, for example, actuated micromirror, nonvolatile and dynamic random access memories, tunable capacitors for high-frequency microwave applications, electro-optic modulators, infrared detectors, and microelectromechanical systems, the understanding of the chemical composition and physical properties resulting from different processing methods is crucial. The variation of chemical composition with film thickness mirrors in the variation of physical properties such as optical of the film. Thus, the knowledge of the optical gradient within the film allows identification and further optimization of the thin film processing and applications.

Investigation of optical properties of NN and PZT thin films provides important information of not only scientific but also technological nature. In this work ellipsometry and some Raman spectroscopy investigations were presented. Spectroscopic ellipsometry provided dielectric function spectra from near infrared to deep ultraviolet, and thereby gave information on electronic and phonon band structure. Raman spectroscopy provided phonon spectra, which gave information on crystal structures. The studies made on NN and PZT thin films have a practical importance for the further applications of the NN and PZT.

Defendant thesis

1. For the first time optical properties of the PLD NaNbO_3 thin films were evaluated not only as a function of the wavelength, but also as a function of the film thickness.
2. During thermo-optical investigations in the temperature range 5-830 K, five phase transitions and thermo-optical coefficients were established for the NaNbO_3 thin films.
3. Substantial change of refractive index within the film was detected for the NaNbO_3 thin films.
4. The shift and broadening of some of the Raman modes, lower temperature of the phase transition $R \rightarrow S$ can be explained with pronounced optical gradient in NN films, what can be caused by the stresses in the films.
5. It was established, that the determinant technological factor of the forming of optical gradient n in the sol-gel PZT thin films is crystallization process and not a chemical synthesis solvent as it was widely considered until now.
6. Higher quality of the optical properties was detected for the PZT thin films made by AcOH/MeOH solvent.
7. For the first time, the thickness dependence of the complex refractive index, interface, roughness and optical band gap as well as optical gradient were studied for the sol-gel PZT thin films. Homogeneous films without thickness depended of complex refractive index, interface and optical band gap can be evaluated by making thick films, and annealing all layers together.

List of scientific publications related to this work

Publications

Published:

1. I. Aulika, A. Deyneka, V. Zauls and K. Kundzins, "Thermo-optical studies of NaNbO_3 thin films", *Journal of Physics, Conference Edition*, V 93, 012016 (2007)
2. I. Aulika, J. Petzelt, J. Pokorny, A. Deyneka, V. Zauls, K. Kundzins, "Structural and Optical Studies of NaNbO_3 Thin Films Grown by PLD on SrRuO_3 Bottom Electrode", *Review of Advanced Material Science*, V 15, 158 (2007)
3. I. Aulika, V. Zauls, K. Kundzins, M. Kundzins, S. Katholy, "Study of transparent ferroelectric thin films by optical reflectometry and ellipsometry", *Journal of Optoelectronics and Advanced Materials*, Vol. 5, No. 3, p. 755–761 (2003)

Accepted for publication:

4. I. Aulika, A. Dejneka, V. Zauls, K. Kundzins, "Optical gradient of the trapezium-shaped NaNbO_3 thin films studied by spectroscopic ellipsometry", *Journal of Electrochemical Society*, Volume 155, Number 10, ... (2008)

Submitted; currently at the reviewer

5. I. Aulika, A. Dejneka, A. Kovalova, V. Zauls, M. Kundzins, "Temperature dependent spectral ellipsometry applied to phase transition study of NaNbO_3 thin films", *Applied Physics A*, (May, 2008)

Currently under preparation

6. I. Aulika, S. Korkovis, A. Dejneka, V. Zauls, Q. Zhang, "Optical depth profile investigation in sol-gel PZT thin films, under preparation (2008)

Conference thesis

International conferences

1. Aulika, Alexandr Dejneka, Vismants Zauls, and Karlis Kundzins, "Spectroscopic ellipsometry studies of BST/PZT superlattices", Abstracts of the "Electroceramics XI", Manchester (United Kingdom), August 1 – September 4, 2008
2. Ilze Aulika, Alexandr Dejneka, Vismants Zauls, and Karlis Kundzins, "Optical properties of BST/PZT nanocomposite superlattices studied by spectroscopic Ellipsometry", Abstracts of the "RCBJSF - 8", Vilnius (Lithuania), June 15 – 19, 2008
3. I. Aulika, A. Dejneka, A. Kovalova, V. Zauls, K. Kundzins, A. Fuith, "Optical studies of NaNbO_3 thin films in the wide temperature range of 5– 820 K", Abstracts of the FM&NT 2008, p. 68, Riga (Latvia), 1 – 4 April (2008)

4. I. Aulika, V. Zauls, K. Kundzins A. Deyneka, „Thermo-optics of NaNbO₃ thin films“, Abstracts of the 11th European Meeting of Ferroelectrics, p. 46, Bled (Slovenia) 3 – 7 September (2007)
5. I. Aulika, V. Zauls, K. Kundzins A. Deyneka, A. Fuith, “Temperature dependence of optical properties for NaNbO₃ thin films”, Abstracts of the ICMAT 2007, p. 72, Singapore, 1- 6 July (2007)
6. I. Aulika, V. Zauls, K. Kundzins, A. Deyneka, “Temperature dependence of refractive coefficient of NaNbO₃ thin films”, Abstracts of the FM&NT 2007, p. 99, Riga (Latvia), 2 – 4 April (2007)
7. I. Aulika, A. Deyneka, V. Zauls, K. Kundzins, J. Pokorny, J. Petzelt, “Characterization of structural and optical properties of nanopatterned polar thin films”, Abstract for the E-MRS 2006 conference, September 4th– 8th, Warsaw, Poland (2006)
8. I. Aulika, V. Zauls, K. Kundzins, M. Kundzins, S. Katholy, Determination of thickness and refractive index of thin films by optical reflectometry and ellipsometry, Abstract book of the fourth intonation edition of Romanian conference on advanced materials: ROCAM 2003, September 15-18th, Constanta, Romania, p. 139 (2003)
9. I. Aulika, “Study of transparent ferroelectrics thin films by optical reflectometry and ellipsometry”, Abstracts of the 17th International Conference for Physics Students ICPS2002, August 21 – 27, Budapest, p.53 (2002)
10. I. Aulika, “Study of transparent ferroelectrics thin films by optical reflectometry and ellipsometry”, Abstracts of the 12th General Conference of the European Physics Society EPS12: Trends in Physics, August 26 – 30, Budapest, p. 133 (2002)

Local conferences

1. I. Aulika, A. Deyneka, V. Zauls, K. Kundzins, „Optical properties of ferroelectric thin films in the temperature range of 4 – 820 K”, Abstracts of the 24th SCISSO, UL, p. 21, Riga (Latvia), 20 – 22 February (2008)
2. I. Aulika, V. Zauls, K. Kundzins, A. Deyneka, „Optical properties of PLD NaNbO₃ thin films”, Abstracts of the 22nd SCISSO, UL, p. 39, Riga (Latvia), 29 – 30 March (2007)
3. Aulika, K. Kundzins, V. Zauls, M. Tunina “Study of transparent thin ferroelectrics films by spectral reflectivity”, Institute of Solid State Physics University of Latvia, Abstracts of the 18th Scientific Conference, February 11 – 13, Riga, p.33 (2002)

List of scientific publications not related to this work

Publications

1. I. Aulika, J. Pokorny, V. Zauls, K. Kundzins, M. Rutkis, J. Petzelt, „Structural and optical characterization of $Ba_{0.8}Sr_{0.2}TiO_3$ films deposited by PLD on various substrates using micro-Raman and spectral ellipsometry methods”, *Optical Materials*, 30, 1017 (2008)
2. I. Aulika, V. Zauls, K. Kundzins, ”Direct atomic force microscopy analysis of surface nanoscale roughness effects on optical properties of PMN thin ferroelectric film multilayers”, *Journal of Latvian physics and technical science*, ISSN 0868 – 8257, 2 (II), p. 83-101 (2006)
3. M. Knite, A. Hill, V. Bovtun, V. Teteris, A. Solovjovs, G. Shakale, J. Zavisckis, I. Aulika etc., “Polymer-nanostructured carbon composites as multifunctional sensor materials: design, processing, and properties”, *Journal of Latvian physics and technical science*, ISSN 0868 – 8257, 2 (I), p. 15-29 (2006)
4. M. Knite, V. Teteris, I. Aulika, H. Kabelka, A. Fuith, “Alternating-current properties of elastomer-carbon nanocomposites”, *Advanced Engineering Materials*, 6, No. 9, p.746-749 (2004)
5. A. Sternberg, K. Kundzins, V. Zauls, I. Aulika, L. Cakare, R. Bittner, H. Weber, K. Humer, D. Lesnyh, D. Kulikov and Y. Trushin, “Antiferroelectric $PbZrO_3$ thin films: structure, properties and irradiation effects”, *Journal of the European Ceramic Society* 24, p. 1653-1657 (2004)
6. I. Aulika, E. Klotins, “Effect of thermal fluctuation on ferroelectric response: dynamic hysteresis”, *Journal of Optoelectronics and Advanced Materials*, Vol. 5, No. 3, p. 747–753 (2003)
7. A. Sternberg, A. Krumins, K. Kundzins, V. Zauls, I. Aulika, L. Cakare, R. Bittner, H. Weber, K. Humer, D. Lesnyh, D. Kulikov and Y. Trushin, “Irradiation effects in lead zirconate thin films”, *Proc. of SPIE* 5122, 341 (2003)
8. H. Schmitt, C. Ziebert, A. Sternberg, V. Zauls, M. Kundzins, K. Kundzins, I. Aulika, K. H. Ehses, J. K. Kruger “Nanocrystalline ferroelectric/relaxor multilayers”, *Ferroelectrics*, Vol.268, p.193-198 (2002)
9. E. Klotins, I. Aulika “High signal thickness mode oscillations of a piezoelectric plate: the role of higher order elastic compliance”, *Materials Science*, Vol.8, No. 3, p. 225-229 (2002)

Conference thesis

International conferences

1. Aulika, V. Zauls, K. Kundzins, M. Rutkis, J. Pokorny, J. Petzelt, "Structural and optical characterization of Ba_{0.8}Sr_{0.2}TiO₃ films deposited by PLD on various substrates using micro-Raman and spectral reflectometry methods", Abstract for the ICOM 2006 conference, August 31th – September 2nd, Herceg Novi, Montenegro (2006)
2. I. Aulika, V. Zauls, K. Kundzins and M. Granats, "Optical properties and surface morphology of PLD deposited BaTiO₃, Ba_{0.8}Sr_{0.2}TiO₃ and SrBi₂Ta₂O₉ thin films", Advanced materials and technologies (The 6-th International Conference-School), Palanga (Lithuania) August 27-31 (2004)
3. A. Sternberg, K. Kundzins, V. Zauls, I. Aulika, L. Čakare, R. Bittner, H. Weber, K. Humer, D. Lesnyh, D. Kulikov and Y. Trushin, "Irradiation effects in lead zirconate thin films", Proc. Abstract book of SPIE 5122, p. 341 (2003)
4. E. Klotins, I. Aulika, Semiadiabatic high field polarization response in ferroelectrics: dynamic hysteresis, nonlinear susceptibility and size effects, Abstract book of the fourth intonation edition of Romanian conference on advanced materials: ROCAM 2003, September 15-18th, Constanta, Romania, p. 140 (2003)
5. A. Sternberg, K. Kundzins, V. Zauls, I. Aulika, L. Čakare, R. Bittner, H. Weber, K. Humer, D. Lesnyh, D. Kulikov, and Y. Trushin, Antiferroelectric PbZrO₃ thin films: structure, properties and irradiation effects, August 25-28, Rome (2002)
6. M. Knite, V. Teteris, A. Vitinsh, I. Aulika "Peculiarities of percolation transition in polyisoprene-carbon black nanocomposites-prospective deformation sensormaterials", European materials research society E – MRS, Book of abstract, Strasbourg, June 18-21, (2002)

Local conferences

1. I. Aulika, J. Levoska, M. Tyunina, K. Kundzins, V. Zauls, "Direct atomic force microscopy analysis of surface nanoscale roughness effects on optical properties of PMN thin ferroelectric film multilayers", Abstracts of the 2nd Latvian conference on function materials and nanotechnologies, March 27 – 28, p. 6 (2006)
2. M. Knite, A. Hill, V. Bovtun, V. Teteris, A. Solovjovs, V. Tupureina, G. Shakale, J. Zavickis, I. Aulika, B. Polakovs, S. J. Pas, S. Veljko, I. Klemenoks, J. Zicans, D. Erts, J. Petzelt, A. Fuith "Polymer-nanostructured carbon composite as multifunctional sensor materials – design, processing and properties", Abstracts of the 2nd Latvian conference on function materials and nanotechnologies, March 27 – 28, p.32 (2006)
3. I. Aulika, J. Levoska, M. Tyunina, K. Kundzins, V. Zauls, "Optical properties of PMN thin films deposited by PLD on MgO/LSCO substrates", Institute of Solid State Physics University of Latvia, Abstracts of the 22nd Scientific Conference, March 29 – 30, Riga, p.20 (2006)

4. V. Zauls, K. Kundzins, I. Aulika, M. Kundzins, A. Sternbergs, "Ferroelectric thin films for future thermonuclear reactor diagnostics applications", Institute of Solid State Physics University of Latvia, Abstracts of the 22nd Scientific Conference, March 29 – 30, Riga, p.35 (2006)
5. I. Aulika, V. Zauls, K. Kundzins, M. Kundzins, M. Granats, "Optical properties and surface morphology of PLD deposited BaTiO₃, Ba_{0.8}Sr_{0.2}TiO₃ and SrBi₂Ta₂O₉ thin films", Abstracts of the International student conference on "Developments in optics and photonics" 31.04 – 1.05.2005, Riga, p.50 (2005)
6. Aulika, V. Zauls, K. Kundzins and M. Granats, "Studies of optical properties and surface morphology of laser deposited BaTiO₃, Ba_{0.8}Sr_{0.2}TiO₃ and SrBi₂Ta₂O₉ thin films", Institute of Solid State Physics University of Latvia, Abstracts of the 21st Scientific Conference, February 7 – 9, Riga, p.25 (2005)
7. Aulika, V. Zauls, K. Kundzins, M. Kundzins, "Thickness effects on optical properties of BaTiO₃ thin films", Institute of Solid State Physics University of Latvia, Abstracts of the 20th Scientific Conference, February 16 – 18, Riga, p.52 (2004)
8. E. Birks, I. Aulika, A. Spule, M. Antonova, A. Sternbergs, A. Fuith, H. Kabelka, "Physical properties and phase diagrams of PLZT x/85/15 solid solutions", Institute of Solid State Physics University of Latvia, Abstracts of the 20th Scientific Conference, February 16 – 18, Riga, p.53 (2004)
9. I. Aulika, E. Klotins, "Semiadiabatic high field polarization response in ferroelectrics: dynamic hysteresis", Institute of Solid State Physics University of Latvia, Abstracts of the 20th Scientific Conference, February 16 – 18, Riga, p.49 (2004)
10. I. Aulika, E. Klotins "Effect of thermal fluctuations on ferroelectric response: nonlinear susceptibility", Institute of Solid State Physics University of Latvia, Abstracts of the 20th Scientific Conference, February 16 – 18, Riga, p.50 (2004)
11. A. Sternbergs, I. Aulika, V. Zauls, K. Kundzins, M. Kundzins, R. Bittner, H. W. Weber, "Intensive neutron irradiation effects on sol – gel PbZrO₃ and PbZr_{1-x}Ti_xO₃ thin films", Institute of Solid State Physics University of Latvia, Abstracts of the 20th Scientific Conference, February 16 – 18, Riga, p.34 (2004)
12. A. Sternbergs, I. Aulika, V. Zauls, K. Kundzins, M. Kundzins, R. Bittner, H. W. Weber, E. Hodgson, "Physical properties of ferroelectric and antiferroelectric thin films after electron irradiation", Institute of Solid State Physics University of Latvia, Abstracts of the 20th Scientific Conference, February 16 – 18, Riga, p.33 (2004)
13. A. Sternberg, I. Aulika, K. Kundzins, V. Zauls, R. Bittner, H. Weber, D. Lesnihs, D. Kulikovs, J. Trusins "Intensity neutron irradiation effects of the ferroelectric and antiferroelectric thin films structure and properties", Institute of Solid State Physics University of Latvia, Abstracts of the 19th Scientific Conference, February 10 – 13, Riga, p.19 (2003)

14. I. Aulika, V. Zauls, K. Kundzins, M. Kundzins, S. Katholy, "Determination of thickness and refractive index of thin films by optical reflectometry and ellipsometry" Institute of Solid State Physics University of Latvia, Abstracts of the 19th Scientific Conference, February 10 –34, Riga, p. 13 (2003)
15. A. Sternberg, A. Krumins, K. Kundzins, V. Zauls, I. Aulika, L. Čakare, R. Bittner, H. Weber, K. Humer, D. Lesnyh, D. Kulikov, and Y. Trushin, Irradiation effects in lead zirconate thin films, Proc.AOMD-3, August 19-22, Riga (2002)
16. I. Aulika, K. Kundzins, V. Zauls, L. Cakare "The measurement method of the dielectric hysteresis loops in ferroelectric films with increased conductivity", Institute of Solid State Physics University of Latvia, Abstracts of the 18th Scientific Conference, February 11 – 13, Riga, p.32 (2002)
17. A. Sternberg, I. Aulika, K. Kundzins, V. Zauls, L. Cakare, R. Bittner, H. Weber "Antiferroelectric PtZrO₃ thin films: Structure, properties and irradiation effects", Institute of Solid State Physics University of Latvia, Abstracts of the 18th Scientific Conference, February 11 – 13, Riga, p.34 (2002)
18. M. Knite, V. Teteris, A. Vitins, I. Aulika "Features of percolation transition in polyisoprene-carbon black nanocomposites-prospective deformation sensormaterials", Institute of Solid State Physics University of Latvia, Abstracts of the 18th Scientific Conference, February 11 – 13, Riga, p.72 (2002)

Scientific seminars and conferences, where work have been discussed

Seminars

1. Preliminary defense of the doctoral thesis at the Institute of Solid State Physics, Riga, Latvia, 03.07.2008

Optical depth profile and phase transitions investigation of NaNbO_3 and $\text{Pb}(\text{Zr,Ti})\text{O}_3$ thin films

2. Jozefa Stefana Institute, Ljubljana, Slovenia, 20.06.2008

Optical gradient of PZT sol-gel thin films

<p><i>Ellipsometric investigations of optical properties of inhomogeneous and ultra-thin ferroelectric thin films: some results in framework of MIND project</i></p>
--

3. Institute of Solid State Physics, Riga, Latvia, 14.04.2008

4. LUSI, Blois, France, 22.01.2008

Lead-free FE thin films

Ellipsometry analysis of ultra-thin PT films

Optical properties and phase transition of PZT thin film

5. Instituto de Ciencia de Materiales de Madrid, Madrid, Spain, 03.10.2007

Spectral & Null Ellipsometry – Powerful Technique for Thin Film Studies

International conferences

1. “Electroceramics XI”, Manchester (UK), August 1 – September 4, 2008
2. “The 8th Russia/CIS/Baltic/Japan Symposium on Ferroelectricity (RCBJSF – 8)”, Vilnius (Lithuania), June 15 – 19, 2008
3. „Functional Materials & Nano-Technologies 2008 (FM&NT2008)”, Riga (Latvia), 1 – 4 April, 2008
4. „11th European Meeting of Ferroelectrics”, Bled (Slovenia), 3 – 7 September, 2007
5. „International conference on Materials on Advanced Technologies (ICMAT 2007)”, Singapore, 1- 6 July, 2007
6. „ Functional Materials & Nano-Technologies 2007 (FM&NT 2007)”, Riga (Latvia), 2 – 4 April, 2007
7. “The European Materials Research Society (E-MRS 2006)”, Warsaw (Poland), September 4 – 8, 2006.
8. “Functional Materials & Nano-Technologies 2006 (FM&NT 2006)”, Riga (Latvia), March 27 – 28, 2006.

Local conferences

1. “24th Conference of Institute of Solid State Physics University of Latvia (SCISSO, UL)”, Riga (Latvia), 20 – 22 February, 2008
2. “23rd (SCISSO, UL)”, Riga (Latvia), 29 – 30 March, 2007

3. “22nd SCISSO, UL”, Riga (Latvia), 29 – 30 March, 2006

The author’s education and scientific experience

The author of this work started her studies of physics at the University of Latvia, at the Department of Physics and Mathematics on 1998’s. The bachelor’s degree in natural sciences, physics, was received on 2002’s. Studies were continued, and on 2004’s the master’s degree in natural sciences, physics, was received. Afterwards the studies were continued by concluding at the doctoral program, at the University of Latvia, Department of Physics and Mathematics. During this period of time scientific experience was obtained and extended by working at the Institute of Solid State Physics (Riga) on dielectric and optical properties of ferroelectric thin films.

The scientific experience was also periodically extended in many institutes abroad, such as Atomic Institute of the Austrian Universities, Vienna, Austria (2003/3004), Laboratory of microelectronics, University of Oulu, Oulu, Finland (2005), Institute of Experimental Physics, University of Vienna, Vienna, Austria (2002 - 2006), Institute of Physics, Academy of Sciences of the Czech Republic, Prague (2005, 2007, 2008).

During this period of time, the author of this work got an experience and knowledge of the experimental planning and performing, complex data analysis, interpretation of the results and scientific paper writing.

The research of this thesis was done at the Institute of Solid State Physics in Riga and Institute of Physics in Prague. Dielectric, reflectometric, and null-ellipsometric measurements, as well as data analysis, interpretation and paper writing were performed in Riga on 2004 – 2008. Spectroscopic ellipsometry and Raman spectroscopy were done periodically in Prague on 2005, 2007 and 2008. This thesis contains the results of the research carried along this period of time, working in Riga and in Prague from 2004 – 2008.

The work was made in co-operation with

- **Cranfield University (United Kingdom) and Institute of Physics,**



From this University the sol-gel PZT samples were received. Samples made Dr. phys. Silvana Corcovic in the framework of MIND project.

- **Institute of Physics, Academy of Sciences of the Czech Republic, Prague.**



The author of this work made all thermo-optical and room temperature optical investigations at the Institute of Physics. During the collaboration between Institute of Solid State Physics and Institute of Physics in Prague the cooperation agreement was concluded.

- **Solid States and Material Research in Dresden (Germany),**

In this institute the M.Sc. project was made the PLD NN thin films.



Leibniz Institute
for Solid State and
Materials Research
Dresden

This thesis was made in the framework of two projects:

- **Sixth Framework Programme of the Multifunctional & Integrated Piezoelectric Devices (MIND)**



- **European Social Founds.**



The work have been supported by the scholarships

- **Scholarship of Kristaps Morbergs, University of Latvia (2004)**



- **European Social Founds (2004 - 2008)**



- **UNESCO LÓREAL stipendium for woman in science (2008/2009)**



Acknowledgments

I would like to express my deepest gratitude to my supervisor Dr. Vismants Zauls and director Dr Andris Sternbergs for their guidance, support, encouragement and invaluable advices throughout these years in all aspects of the work. Without them this work was not possible. My more sincere thanks for both.

I am grateful to Dr. Jan Petzelt and Dr. Alexander Dejneka for kindness that made possible my stay at the Institute of Physics (Prague) and all help during several months that I was there and until the defense of this thesis. A. Dejneka and J. Petzelt experience and knowledge of the ellipsometric techniques and Raman spectroscopy have permitted to realize a really interesting work. Many thanks for suggestions, discussions, and help with the Raman and ellipsometric measurements. And also for the very valuable hints and guidance in physics aspects that were essential for the development of all this work.

Many thanks are also given to the Dr. Qi Zhang and Dr. Silvaan Corcovic from the Cranfield University for their support with the sol-gel PZT samples.

I would like to thank to all my doctoral companions for being such excellent colleagues. Especially to Maris Kundzins, Karlis Kundzins, Eriks Klotins, Eriks Birks, Karlis Bormanis for all they help and support.

Many thanks to M.Sc.phys Karlis Kundzins for help and guidance with the AFM equipment, and PLD NN sample preparation at the Solid States and Material Research in Dresden (Germany).

My deepest love to my friends Janis Garancs, Armin Fuith, Jelena Butikova, Ulrika Plivca, and family – mother Inara Ratniece, futher Ugis Auliks, grandmothers Velta Kodola and Brigita Aulika, sisters Patricija Ratniece and Iveta Ratniece and cosine Girts Brokans for all their support, help and great patience.

I am grateful to DJ Armin Van Buuren for his absolutely great remixes on “State Of Trance”, what supported my work during calculations and thesis writing.

I would like to acknowledge the University of Latvia for the doctoral fellowships – K. Morberg scholarship and European Social Found - that made it possible to conduct the doctoral work.

I am grateful to the Ministry of the Education and Science for the partisanship at the Sixth Framework Program of the *Multifunctional & Integrated Piezoelectric Devices* (MIND) in framework of what this thesis was realized.

References

- [1] Yasuyoshi Saito, Hisaaki Takao, Toshihiko Tani, Tatsuhiko Nonoyama, Kazumasa Takatori, Takahiko Homma, Toshiatsu Nagaya & Masaya Nakamura, Lead-free piezoceramics, *Nature* **432** (2004) 84
- [2] Takahiro Wada, Kenji Tsuji, Takehisa Saito and Yoshihiro Matsuo, Ferroelectric NaNbO_3 Ceramics Fabricated by Spark Plasma Sintering, *Jpn. J. Appl. Phys.* **42** (2003) 6110
- [3] Sh. Zhang et al., *J. Electrocer.* **19** (2007) 251
- [4] L. A. Reznitchenko, A. V. Turik, E. M. Kuznetsova and V. P. Sakhnenko, Piezoelectricity in NaNbO_3 ceramics, *J. Phys.: Condens. Matter* **17** (2001) 3875
- [5] R.W. Whatmore, Q. Zhang, Z. Huang, R.A. Dorey, Ferroelectric thin and thick films for microsystems, *Mater. Sci. Semicond. Process.* **5** (2003) 65.
- [6] P. Muralt, Ferroelectric thin films for micro-sensors and actuators: a review, *J. Micromech. Microeng.* **10** (2000) 136
- [7] Youngjoo Yee, Hyo-Jin Nam, See-Hyung Lee, Jong Uk Bu, Joong-Won Lee, PZT actuated micromirror for fine-tracking mechanism of high-density optical data storage, *Sensors and Actuators A* **89** (2001) 166
- [8] B.G. Bovard, Rugate filter design: the modified Fourier transform technique, *Appl. Opt.* **29** (1990) 24
- [9] M. F. Oulette, R. V. Lang, K. L. Yan, R. W. Bertram, R. S. Owle, D. Vincent, *J. Vac. Sci. Technol. A* **9** (1991) 1188
- [10] H. D. Megaw, The seven phases of sodium niobate, *Ferroelectrics* **7** (1974) 87
- [11] Landolt-Bornstein, Volume **16**, *Ferroelectric and Related Substances*, New York, (1981) 45
- [12] C.N.W. Darlington, K.S. Knight, On the lattice parameters of sodium niobate at room temperature and above, *Physica B* **266** (1999) 368
- [13] C. N. W. Darlington, H. D. Megaw, The Low-Temperature Phase Transition of Sodium Niobate and the Structure of the Low-Temperature Phase, *Acta Crystallogr.* **B29** (1973) 2171
- [14] I. Lefkowitz, K. Lukaszewicz and H. D. Megaw, The High-Temperature Phases of Sodium Niobate and the Nature of Transitions in Pseudosymmetrical Structures, *Acta Cryst.* **20** (1966) 670
- [15] F. Denoyer, R. Comes and M. Lambert, X-ray Diffuse Scattering from NaNbO_3 as a Function of Temperature, *Acta Cryst.* **A27** (1971) 414
- [16] A. M. Glazer and H. D. Megaw, Studies of the Lattice Parameters and Domains in the Phase Transitions of NaNbO_3 , *Acta Cryst.* **A29** (1973) 489
- [17] Tae Song Kim, Myung Hwan Oh and Chong Hee Kim, Influences of Indium Tin Oxide Layer on the Properties of RF Magnetron-Sputtered $(\text{BaSr})\text{TiO}_3$ Thin Films on Indium Tin Oxide-Coated Glass Substrate, *Jpn. J. Appl. Phys.* **32** (1993) 2837
- [18] K. Sumi, H. Qiu, H. Kamei, S. Moriya, M. Murai, M. Shimada, T. Nishiwaki, K. Takei, S. Miyashita, M. Hashimoto, Thickness dependence of structural and ferroelectric properties of sol-gel $\text{Pb}(\text{Zr}_{0.56}\text{Ti}_{0.44})_{0.90}(\text{Mg}_{1/3}\text{Nb}_{2/3})_{0.10}\text{O}_3$ films, *Thin Solid Films*, **330** (1998) 183
- [19] Hu-Yong Tian, Wei-Gen Luo, Ai-Li Ding, Jongwan Choi, Changho Lee, Kwangsoo No, Influences of annealing temperature on the optical and structural properties of $(\text{Ba,Sr})\text{TiO}_3$ thin films derived from sol-gel technique, *Thin Solid Films*, **408** (2002) 200

- [20] Nicolas Ledermann, Paul Muralt, Jacek Baborowski, Sandrine Gentil, Kapil Mukati, Marco Cantoni, Andreas Seifert, Nava Setter, {1 0 0}-Textured, piezoelectric $\text{Pb}(\text{Zr}_x\text{Ti}_{1-x})\text{O}_3$ thin films for MEMS: integration, deposition and properties, *Sensors and Actuators A* **105** (2003) 162
- [21] Paul G. Snyder, Yi-Ming Xiong, John A. Woollam, Ghanim A. Al-Jumaily, and F. J. Gagliardi, Graded refractive index silicon oxynitride thin film characterized by spectroscopic ellipsometry, *J. Vac. Sci. Technol. A* **10** (1992) 1462
- [22] V. Nguyen Van, A. Brunet-Bruneau, S. Fisson, J. M. Frigerio, G. Vuye, Y. Wang, F. Abelvs, J. Rivory, M. Berger, and P. Chaton, Determination of refractive-index profiles by a combination of visible and infrared ellipsometry measurements, *Appl. Opt.* **35** (1996) 5540
- [23] J. Rivory, Characterization of inhomogeneous dielectric films by spectroscopic ellipsometry, *Thin Solid Films* **313-314** (1998) 333
- [24] S. Callard, A. Gagnaire, J. Joseph, Characterization of graded refractive index silicon oxynitride thin films by spectroscopic ellipsometry, *Thin Solid Films* **313-314** (1998) 384
- [25] S. Trolier-McKinstry, J. Koh, Composition profiling of graded dielectric function materials by spectroscopic ellipsometry, *Thin Solid Films* **313-314** (1998) 389
- [26] H. Nishizawa, Y. Tateyama, T. Saitoh, Ellipsometry characterization of oxidized copper layers for chemical mechanical polishing process, *Thin Solid Films* **455-456** (2004) 491
- [27] M. Guenther, G. Gerlach, G. Suchaneck, K. Sahre, K.-J. Eichhorn, B. Wolf, A. Deineka, L. Jastrabik, Ion-beam induced chemical and structural modification in polymers, *Surface and Coatings Technology* **158-159** (2002) 108
- [28] Maria Losurdo, Relationships among surface processing at the nanometer scale, nanostructure and optical properties of thin oxide films, *Thin Solid Films* **455-456** (2004) 301
- [29] Dale E. Morton, Blaine Johs and Jeff Hale, *Soc. of Vac. Coat.* 505/856-7188, 45th Ann. Techn. Conf. Proc. ISSN 0737-5921 (2002) 1
- [30] A. Deineka; M. D. Glinchuk, L. Jastrabik, G. Suchaneck, G. Gerlach, Nondestructive Investigations of the Depth Profile of PZT Ferroelectric Films, *Ferroelectrics* **264** (2001) 151
- [31] G. Suchaneck, W. -M. Lin, R. Koehler, T. Sandner, G. Gerlach, R. Krawietz, W. Pompe, A. Deineka, L. Jastrabik, Characterization of RF-sputtered self-polarized PZT thin films for IR sensor arrays, *Vacuum* **66** (2002) 473
- [32] Pierre Boher, Jean Louis Stehle, Jean Philippe Piel, M. Fried, T. Lohner, O. Polgar, N. Q. Khanh, I. Barsony, Spectroscopic ellipsometry applied to the determination of an ion implantation depth profile, *Nuclear Inst. And Meth. In Phys. Res. B* **112** (1996) 160
- [33] M. Fried, P. Petrik, T. Lohner, N.Q. Khanh, O. Polgar, J. Gyulai, Dose-dependence of ion implantation-caused damage in silicon measured by ellipsometry and backscattering spectrometry, *Thin Solid Films* **455-456** (2004) 404
- [34] B.J. Gibbons, S. Trolier-McKinstry, The sensitivity limits of spectroscopic ellipsometry to oxygen content in $\text{YBa}_2\text{Cu}_3\text{O}_{7\pm\delta}$ thin films, *Thin Solid Films* **352** (1999) 205
- [35] I. Aulika, A. Deyneka, V Zauls and K Kundzins, Thermo-optical studies of NaNbO_3 thin films, *J. Phys., Conf. Ser.* **V 93** (2007) 012016

- [36] I. Aulika, A. Dejneka, A. Kovalova, V. Zauls, M. Kundzins, Temperature dependent spectral ellipsometry applied to phase transition study of NaNbO_3 thin films, submitted to *Applied Physics A*, (May, 2008)
- [37] I. Aulika, J. Petzelt, J. Pokorny, A. Deyneka, V. Zauls, K. Kundzins, Structural and Optical Studies of NaNbO_3 Thin Films Grown by PLD on SrRuO_3 Bottom Electrode, *Rev. Adv. Mater. Sc.* **V 15** (2007) 158
- [38] I. Aulika, A. Dejneka, V. Zauls, K. Kundzins, Optical gradient of the trapezium-shaped NaNbO_3 thin films studied by spectroscopic Ellipsometry, *J. Electrochem. Soc.*, will be published on Volume 155, Number 10, ... (2008)
- [38a] I. Aulika, S. Korkovis, A. Dejneka, V. Zauls, Q. Zhang, Optical depth profile investigation in sol-gel PZT thin films, under preparation (2008)
- [38b] I. Aulika, bachelor's work "Evaluation of the thickness and refractive index of thin films by optiskal reflektometrija and ellipsometrija", University of Latvia, Riga, 2002.
- [38c] I. Aulika, master's work "Study of the ferroelectric heterostructure's optical properties by ellipsometry and spectral reflectometry", University of Latvia, Riga, 2004
- [39d] I. Aulika, V. Zauls, K. Kundzins, M. Kundzins, S. Katholy, "Study of transparent ferroelectric thin films by optical reflectometry and ellipsometry", *Journal of Optoelectronics and Advanced Materials*, Vol. 5 (2003) 755
- [39] M. Dawber, K. M. Rabe, and J. F. Scott, Physics of thin-film ferroelectric oxides, *Rev. Mod. Phys.* **77** (2005) 1083
- [40] G. Shirane, R. Newnham, and R. Pepinsky, Dielectric properties and phase transitions of NaNbO_3 and $(\text{Na}, \text{K})\text{NbO}_3$, *Phys. Rev.* **96**, 3 (1954) 581
- [41] P. Vousden, The Structure of Ferroelectric Sodium Niobate at Room Temperature, *Acta Cryst.* **4** (1951) 545
- [42] E. A. Wood, Polymorphism in Potassium Niobate, Sodium Niobate, and other ABO_3 Compounds, *Acta Cryst.* **4** (1951) 353
- [43] M. H. Francombe, High-Temperature Structure Transitions in Sodium Niobate, *Acta Cryst.* **9** (1956) 256
- [44] H. D. Megaw and M. Wells, The Space Group of NaNbO_3 and $(\text{Na}_{0.995}\text{K}_{0.005})\text{NbO}_3$, *Acta Cryst.* **11** (1958) 858
- [45] H. D. Megaw, The Thermal Expansion of Interatomic Bonds, Illustrated by Experimental Evidence from Certain Niobates, *Acta Cryst.* **A24** (1968) 589
- [46] A. C. Sakowski-Cowley, K. Lukaszewicz and Helen D. Megaw, The Structure of Sodium Niobate at Room Temperature, and the Problem of Reliability in Pseudosymmetrie Structures, *Acta Cryst.* **B25** (1969) 851
- [47] E. A. Wood, R. C. Miller and J. P. Remeika, The Field-Induced Ferroelectric Phase of Sodium Niobate, *Acta Cryst.* **15** (1962) 1273
- [48] B. T. Matthias and J. P. Remeika, dielectric properties of sodium and potassium niobates, *Phys. Rev.* **82**, 5 (1951) 727
- [49] R. C. Miller, E. A. Wood, J. P. Remeika, and A. Savage, $\text{Na}(\text{Nb}_{1-x}\text{V}_x)\text{O}_3$ System and "Ferroelectricity", *J. of Appl. Phys.* **33**, 5 (1962) 1623
- [50] K. Konieczny, Pyroelectric and dielectric study of NaNbO_3 single crystals, *Mat. Sc. and Engin.* **B60** (1999) 124
- [51] F. Jona, G. Shirane, and R. Pepinsky, Optical Study of PbZrO_3 and NaNbO_3 Single Crystals, *Phys. Rev.* **97**, 6 (1954) 1584
- [52] L.E. Cross and B.J. Nicholson, *Phil. Mag.* **46** (1955) 453

- [53] A. Reisman, F. Holtzberg and E. Banks, Reactions of the Group VB Pentoxides with Alkali Oxides and Carbonates. VII. Heterogeneous Equilibria in the System Na_2O or $\text{Na}_2\text{CO}_3\text{-Nb}_2\text{O}_5$, *J. Amer. Chem. Soc.* **80** (1958) 37
- [54] A. Avogadro, G. Bonera, F. Borsa, and A. Rigamoti, Static and dynamic properties of the structural phase transitions in NaNbO_3 , *Phys. Rev.* **9**, 9 (1974) 3905
- [55] M. Drulis, K. Konieczny, Low-temperature heat capacity of NaNbO_3 compound, *Mat. Sc. Eng.* **B72** (2000) 19
- [56] F. Gervais, J.L. Servoin, J.F. Baumard and F. Denoyer, Zone-center soft mode behavior in the cubic phase of NaNbO_3 , *Solid State Commun.* **41** (1982) 345
- [57] A. Molak, The Influence of Reduction in Valency of Nb Ions on the Antiferroelectric Phase Transition in NaNbO_3 , *Sol. St. Commun.*, **62**, 6, (1987) 413
- [58] M. Kruczek, E. Talik, A. Kania, Electronic structure of AgNbO_3 and NaNbO_3 studied by X-ray photoelectron spectroscopy, *Solid State Communications* **137** (2006) 469
- [59] H. Muthurajan, H.H. Kumar, V. Samuel, U.N. Gupta, V. Ravi, Novel hydroxide precursors to prepare NaNbO_3 and KNbO_3 , *Ceramics International* **34** (2008) 671
- [60] F. Denoyer, M. Lambert, R. Comes, R. Currat, Inelastic neutron scattering study in cubic NaNbO_3 , *Sol. Stat. Comun.* **18** (1976) 441
- [61] LEAF project, G5RD-CT-2001-00431, EC 5th Framework Programme, GROWTH, 2001–2004.
- [62] P. Gonnard and L. Simon-Seveyrat, Environmentally Conscious Electroceramics. In *Processing of Electroceramics, Conference Notes*, ed. M. Kosec, D. Kuscer, and B. Malic (POLECER Symposium, Jozef Stefan Institute, Ljubljana (2003) p. 331
- [63] T. Takenaka, K. Maruyama, and K. Sakata, $(\text{Bi}_{1/2}\text{Na}_{1/2})\text{TiO}_3\text{-BaTiO}_3$ system for lead-free piezoelectric ceramics. *Jpn. J. Appl. Phys.* **30** (1991) 2236
- [64] T. Takenaka, T. Okuda, N. Kondo, and K. Sakata. Low-lead-content Piezoelectric Ceramics Based on $(\text{Bi}_{1/2}\text{Na}_{1/2})\text{TiO}_3 - \text{NaNbO}_3 - \text{PbTiO}_3$. In *ISAF '96—Proceedings of the 10th IEEE International Symposium on Applications of Ferroelectrics*, ed. B. M. Kulwicki, A. Amin, and A. Safari. IEEE (1996) 619
- [65] M. A. L. Nobre, E. Longo, E. R. Leite, J. A. Varela, Synthesis and sintering of ultra fine NaNbO_3 , powder by use of polymeric precursors, *Materials Letters* **28** (1996) 215
- [66] T. Hungria, L. Pardo, A. Moure, A. Castro, Effect of mechanochemical activation on the synthesis of NaNbO_3 and processing of environmentally friendly piezoceramics, *Journal of Alloys and Compounds* **395** (2005) 166
- [67] Z. Cheng, K. Ozawa, M. Osada, A. Miyazaki, and H. Kimura, Low-Temperature Synthesis of NaNbO_3 Nanopowders and their Thin Films from a Novel Carbon-Free Precursor, *J. Amer. Cer. Soc.*, **89** (2006) 1188
- [68] T. Rojac, O. Masson, R. Guinebretiere, M. Kosec, B. Malic, J. Holc, A study of the mechanochemical synthesis of NaNbO_3 , *J. of Europ. Cer. Soc.* **27** (2007) 2265
- [69] H. Muthurajan, H.H. Kumar, V. Samuel, U.N. Gupta, V. Ravi, Novel hydroxide precursors to prepare NaNbO_3 and KNbO_3 , *Ceramics International* **34** (2008) 671
- [70] C. N. W. Darlington, K. S. Knight, High-temperature phases of NaNbO_3 and NaTaO_3 , *Acta Cryst.* **B55** (1999) 24

- [71] X. B. Wang, Z.X. Shen, Z.P. Hu, L. Qin, S.H. Tang, M.H. Kuok, High temperature Raman study of phase transitions in antiferroelectric NaNbO_3 , *J. Mol. Str.* **385** (1996) 1
- [72] Z. X. Shen, X. B. Wang, M. H. Kuok and S. H. Tang, Raman Scattering Investigations of them Antiferroelectric–Ferroelectric Phase Transition of NaNbO_3 , *J. of Raman spectr.* **29** (1998) 379
- [73] Y. Shiratori, A. Magrez, JuIrgen Dornseiffer, Franz-Hubert Haege, Christian Pithan, and Rainer Waser, Polymorphism in Micro-, Submicro-, and Nanocrystalline NaNbO_3 , *J. Phys. Chem. B* **109** (2005) 2012
- [74] S. Lanfredi, L. Dessemond, A.C. Martins Rodrigues, Dense ceramics of NaNbO_3 produced from powders prepared by a new chemical route, *J. Europ. Cer. Soc.* **20** (2000) 983
- [75] Yu-Jen Hsiao, Yen-Hwei Chang, Yee-Shin Chang, Te-Hua Fang, Yin-Lai Chai, Guo-Ju Chen, Tzu-Wei Huang, Growth and characterization of NaNbO_3 synthesized using reaction-sintering method, *Materials Science and Engineering B* **136** (2007) 129–133
- [76] M. H. Lentea, J. de Los S. Guerraa, J.A. Eirasa, S. Lanfredi, Investigation of microwave dielectric relaxation process in the antiferroelectric phase of NaNbO_3 ceramics, *Sol. St. Com.* **131** (2004) 279
- [77] L. Pardo, P. Duran-Martin, P. Mercurio, L. Nibou And B. Jimfinez, Temperature behaviour of structural, dielectric and piezoelectric properties of sol-gel processed ceramics of the system LiNbO_3 - NaNbO_3 , *J. Phw. Chem Solids* **58**, 9 (1997) 1335
- [78] L. A. Reznitchenko, A. V. Turik, E M Kuznetsova and V P Sakhnenko, Piezoelectricity in NaNbO_3 ceramics , *J. Phys.: Condens. Matter* **13** (2001) 3875
- [79] R. J. C. Lima, P. T. C. Freire, J. M. Sasaki, A. P. Ayala, F. E. A. Melo, J. Mendes Filho, K. C. Serra, S. Lanfredi, M. H. Lente and J. A. Eiras, Temperature-dependent Raman scattering studies in NaNbO_3 ceramics, *J. Raman Spectrosc* **33** (2002) 669
- [80] B. Jaffe, W. R. Cook, and H. Jaffe, *Piezoelectric Ceramics*, Academic Press (1971), p. 185
- [81] Erling Ringgaard, Thom Wurlitzer, Wanda W. Wolny, Properties of Lead-Free Piezoceramics Based on Alkali Niobates, *Ferroelectrics* **319** (2005) 97
- [82] B. Noheda, Structure and high-piezoelectricity in lead oxide solid solutions, *Curr. Opinion in Solid State and Mater. Sci.* **6** (2002) 27
- [83] G. O. Karapetyan, V. V. Loboda, D. K. Tagantsev, Glass scrySTALLIZATION by ion exchabge: formation of NaNbO_3 in thick films at the glass surfase, *J of Non-Cryst. Sol.* **282** (2001) 114
- [84] T. Saito, H. Adachi, T. Wada and H. Adachi, Pulsed-Laser Deposition of Ferroelectric NaNbO_3 Thin Films, *Jpn. J. Appl. Phys.* **44** (2005) 6969
- [85] Harland G. Tompkins, Eugene A. Irene, *Handbook of ellipsometry* (NY 2005).
- [86] R. K. Galkiewicz and J. Tauc, Photoelastic properties of amorphous As_2S_3 , *Solid State Commun.* **10** (1972) 1261
- [87] W. F. Koehler, F. K. Odencrantz, and W. C. White, *J. Opt. Soc Am.* **49** (1959) 109
- [88] J. Stuke, Review of optical and electrical properties of amorphous semiconductors, *J. Non-Cryst. Solids* **4** (1970) 1
- [89] R. C. Chittick, Properties of glow-discharge deposited amorphous germanium and silicon, *J. Non-Cryst. Solids* **3** (1970) 255

- [90] S. H. Wemple, Refractive index behavior of amorphous semiconductors and glasses, *Phys. Rev. B* **7** (1973) 3767
- [91] H. R. Philipp, Optical properties of non-crystalline Si, SiO, SiO_x and SiO₂, *J. Phys. Chem. Solids* **32** (1971) 1935
- [92] S Tskahashi, S Shibata, Thermal variation of attenuation for optical fibers, *J Non-Cryst Solids* **30** (1979) 359
- [93] R. Hofmann, S. H. Wemple, and H. Granicher, Dielectric Dispersion of NaOH-Doped Ice at Low Temperatures, *J. Phys. Soc. Jpn.* **28** (1970) 265
- [94] J. Fousek and J. Petzelt, Changes of Refractive Indices of Crystals Induced by Structural Phase Transitions, *Phys. Stat. Sol* **55** (1979) 11
- [95] G. Burns and F. H. Dacol, Polarization in the cubic phase of BaTiO₃, *Solid State Commun.* **42** (1982) 9
- [96] W. Kleemann, F. J. Schafer and M. D. Fontain, Crystal optical studies of spontaneous and precursor polarization in KNbO₃, *Phys. Rev. B* **30** (1984) 1148; W. W. Kleemann, F. J. Schaefer, Soft-Mode Contribution to the Refractive Index of SrTiO₃ and KTaO₃, *Jpn. J. Appl. Phys.* **24** (1985) 260
- [97] N. Izyumskaya, Y.-I. Alivov, S.-J. Cho, and H. Morko c, H. Lee, Y.-S. Kang, Processing, Structure, Properties, and Applications of PZT Thin Films, *Critical Reviews in Solid State and Materials Sciences* **32** (2007) 111
- [98] B. S. Kwak, A. Erbil, J. D. Budai, M. F. Chisholm, L. A. Boatner, and B. J. Wilkents, Domain formation and strain relaxation in epitaxial ferroelectric heterostructures, *Phys. Rev. B* **49** (1994) 14865
- [99] L. B.Kong, J. Ma,W. Zhu, and O. K. Tan, Preparation and characterization of lead zirconate ceramics from high-energy ball milled powder, *Mat. Lett.* **49** (2001) 96
- [100] C. M. Foster, G.-R. Bai, R. Csencsits, J. Vetrone, R. Jammy,L. A. Wills, E. Carr, and J. Amano, Single-crystal Pb(Zr_xTi_{1-x})O₃ thin films prepared by metal-organic chemical vapor deposition: Systematic compositional variation of electronic and optical properties, *J. Appl. Phys.* **81** (1997)2349
- [101] G. Shirane and K. Suzuki, Crystal structure of Pb(Zr,Ti)O₃, *J. Phys. Soc. Japan* **7** (1952) 333,
- [102] B. Noheda, D. E. Cox, G. Shirane, J. A. Gonzalo, L. E. Cross, and S.-E. Park, A monoclinic ferroelectric phase in the Pb(Zr_{1-x}Ti_x)O₃ solid solution, *Appl. Phys. Lett.* **74** (1999)2059
- [103] B. Noheda, D. E. Cox, G. Shirane, R. Guo, B. Jones, and L. E. Cross, Stability of the monoclinic phase in the ferroelectric perovskite PbZr_{1-x}Ti_xO₃, *Phys. Rev. B.* **63** (2001) 014103
- [104] D. I.Woodward, J. Knudsen, and I. M. Reaney, Review of crystal and domain structures in the PbZr_xTi_{1-x}O₃ solid solution, *Phys. Rev. B.* **72** (2005) 104110
- [105] B. Noheda, and D. E. Cox, Bridging phases at the morphotropic boundaries of lead oxide solid solutions, *Phase Transitions* **79** (2006) 5
- [106] C. H. Peng, J.-F. Chang, and S. B. Desu, Optical properties of PZT, PLZT, and PNZT thin films, *Mater. Res. Soc. Proceed.* **243** (1992) 21
- [107] S. Yang, D. Mo, and X. Tang, Determination of the optical properties of sol-gel-derived Pb(Zr_xTi_(1-x))O₃ thin films by spectroscopic ellipsometry, *Ferroelectrics* **287** (2003) 35
- [108] Z. G. Hu, F. W. Shi, T. Lin, Z. M. Huang, G. S. Wang, Y. N. Wu, and J. H. Chu, Infrared spectroscopic ellipsometry of (Pb, La)(Zr, Ti)O₃ thin films on platinized silicon, *Appl. Phys. Lett.* **320** (2004) 478

- [109] B. G. Potter, Jr., M. B. Sinclair, D. Dimos, B. A. Tuttle, and R.W.Schwartz, Electro-optical and optical evaluation of $\text{Pb}(\text{Zr}, \text{Ti})\text{O}_3$ thin films using waveguide refractometry, *J. Non-Cryst. Solids*, **178** (1994) 69
- [110] H. Lee, Y. S. Kang, S.-J. Cho, B. Xiao, H. Morko c, and T. D. Kang, Visible ultraviolet spectroscopic ellipsometry of lead zirconate titanate thin films, *Appl. Phys. Lett.* **86** (2005) 262902
- [111] Z. Hwang, X. Meng, P. Yang, Z. Zhang, and J. Chu, Optical properties of $\text{PbZr}_x\text{Ti}_{1-x}\text{O}_3$ on platinized silicon by infrared spectroscopic ellipsometry, *Appl. Phys. Lett.* **76** (2000) 3980
- [112] H. Lee, Y. S. Kang, S.-J. Cho, H. Morko c, T. D. Kang, G. S. Lee, J. Lee, S.-H. Wei, P. G. Snyder, and J. T. Evans, Dielectric functions and electronic band structure of lead zirconate titanate thin films, *J. Appl. Phys.* **98** (2005) 094108
- [113] P. D. Thacher, Refractive index and surface layers of ceramic $(\text{Pb}, \text{La})(\text{Zr}, \text{Ti})\text{O}_3$ compounds, *Appl. Optics* **16** (1977) 3210
- [114] C.-K. Kao, N. P. Kuraganti, C.-H. Tsai, I.-N. Lin, R. K. Pandey, and K.-J. Ma, Preparation of textured growth $\text{Pb}(\text{Zr}, \text{Ti})\text{O}_3$ thin films on Si substrate using SrTiO_3 as buffer layers, *Integr. Ferroelectr.* **57** (2003) 1257
- [115] B. Vilquin, R. Bouregba, G. Poullain, H. Murray, E. Dogheche, and D. Remiens, Crystallographic and optical properties of epitaxial $\text{Pb}(\text{Zr}_{0.6}, \text{Ti}_{0.4})\text{O}_3$ thin films grown on LaAlO_3 substrates, *J. Appl. Phys.* **94** (2003) 5167
- [116] M. P. Moret, M. A. C. Devillers, K. Worhoff, and P. K. Larsen, Optical properties of PbTiO_3 , $\text{PbZr}_x\text{Ti}_{1-x}\text{O}_3$, and PbZrO_3 films deposited by metalorganic chemical vapor on SrTiO_3 , *J. Appl. Phys.* **92** (2002) 468
- [117] A. Okada, Some electrical and optical properties of ferroelectric lead-zirconate–lead-titanate thin films, *J. Appl. Phys.* **48** (1977) 2905; A. Okada, Electrical properties of lead-zirconate–lead-titanate ferroelectric thin films and their composition analysis by Auger electron spectroscopy, *J. Appl. Phys.* **49** (1978) 4495
- [118] V. I. Zametin, Absorption edge anomalies in polar semiconductors and dielectrics at phase transitions, *Phys. Stat. Sol. (b)* **124** (1984) 625
- [119] P. D. Thacher, Refractive index and surface layers of ceramic $(\text{Pb}, \text{La})(\text{Zr}, \text{Ti})\text{O}_3$ compounds, *Appl. Optics* **16** (1977) 3210
- [120] M. D. Glinchuk, E.A. Eliseev, V.A. Stephanovich, The depolarization field effect on the thin ferroelectric films properties, *Physica B*, **322** (2002) 356
- [121] M. Campoy-Quiles, P.G. Etchegoin, D.D.C. Bradley, Exploring the potential of ellipsometry for the characterisation of electronic, optical, morphologic and thermodynamic properties of polyfluorene thin films, *Synthetic Metals* **155** (2005) 279
- [122] Mathias Schubert, Wayne Dollase, Generalized ellipsometry for biaxial absorbing materials: determination of crystal orientation and optical constants of Sb_2S_3 , *Opt. Lett.* **27** (2002) 2073
- [123] A. Michaelis, J.W. Schultze, Anisotropy micro-ellipsometry for in-situ determination of optical and crystallographic properties of anisotropic solids and layers with Ti/TiO_2 as an example, *Thin Solid Films* **274** (1996) 82-94
- [124] A. Michaelis, M. Schweinsberg, An anisotropy microellipsometry (AME) study of anodic film formation on Ti and Zr single grains, *Thin Solid Films* **313-314** (1998) 756
- [125] M. Born, E. Wolf, *Principles of optics*, 7th (expanded) edition, Cambridge University press (1999)

- [126] H. G. Tompkins, Williams A. McGahan, *Spectroscopic ellipsometry and reflectometry, A User's Guide*, a Wiley-Interscience publication (1999)
- [127] H. G. Tompkins, *A users's guide to ellipsometry*, Academic Press, New York (1993)
- [128] R. M. A. Azzam and N. M. Bashara, *Ellipsometry and polarized light*, North Holland, Amsterdam (1977)
- [129] Alexei Pimenov, PhD thesis „*Ellipsometry study of the c-axis pseudogap in high temperatur esuperconductors with Zn and Ni impurities*”, Max-Plank-Institut Für Festkorperforschungstuttgart (2005)
- [130] G. E. Jellison, Jr. and J. W. McCamy, Sample depolarization effects from thin films of ZnS on GaAs as measured by spectroscopic ellipsometry, *Appl. Phys. Lett.* **61** (1992) 12
- [131] G. E. Jellison, Jr. and D. H. Lowndes, Time-resolved ellipsometry, *Appl. Opt.* **24** (1985) 2948
- [132] R.A. Synowicki, Thomas E. Tiwald, Optical properties of bulk c-ZrO₂, c-MgO and a-As₂S₃ determined by variable angle spectroscopic ellipsometry, *Thin Solid Film* **455 – 456** (2004) 248
- [133] C. Bungay, T. E. Tiwald, Infrared spectroscopic ellipsometry study of molecular orientation induced anisotropy in polymer substrates, *Thin Solid Film* **455 – 456** (2004) 272; G. E. Jellison, Jr., F. A. Modine, and L. A. Boatner, Measurement of the optical functions of uniaxial materials by two-modulator generalized ellipsometry: rutile (TiO₂), *Optics Letters* **22** (1997) 1808
- [134] A. Synowicki, Spectroscopic ellipsometry characterization of indium tin oxide film microstructure and optical constants, *Thin Solid Film* **313 – 314** (1998) 394
- [135] D. A. Brevnov, C. Bungay, Diameter-Dependent Optical Constants of Gold Mesoparticles Electrodeposited on Aluminum Films Containing Copper, *J. Phys. Chem. B* **109** (2005) 14529
- [136] J. Lappalainen, Jussi Hiltunen, Vilho Lantto, Characterization of optical properties of nanocrystalline doped PZT thin films, *J. Europ. Cer. Soc.* **25** (2005) 2273
- [137] G. E. Jellison, Jr. and F. A. Modine, Parameterization of the optical functions of amorphous materials in the interband region, *Appl. Phys. Lett.* **69** (1996) 371
- [138] Bosch S., Ferre-Borrull J., Sancho-Parraamon, *J. Sol. St. Elec.* **45** (2001) 703
- [139] M. Sparks, Optical Distortion by Heated Windows in High-Power Laser Systems, *J. Appl. Phys.* **42** (1983) 5029
- [140] Y. F. Tsay, B. Bendow, S. S. Mitra, Theory of the Temperature Derivative of the Refractive Index in Transparent Crystals, *Phys. Rev. B* **8** (1973) 2688
- [141] T. Izuminati, H. Toratani, Temperature coefficient of electronic polarizability in optical glasses, *J. Non. Cryst. Sol.* **40** (1980) 611
- [142] F. A. Molly, *Opt. Soc. Am.* **39** (1949) 600
- [143] F. Reimyer, *Glastech. Ber.* **37** (1961) 122
- [144] Sh. Zhu, Y-Li Chen, J-X Fang, Thermal effects of the refractive index caused by the electron-phonon interaction, *Phys. Rev. B* **35** (1987) 2980
- [145] H.Y. Fan, Temperature Dependence of the Energy Gap in Semiconductors, *Phys. Rev.* **82** (1951) 900
- [146] V. P. Varshni, Temperature dependence of the energy gap in semiconductors, *Physica* **34** (1967) 149
- [147] L. Tichy, H. Ticha, The temperature dependence of the optical gap of glassy GeSe₂, *Mater. Lett.* **15** (1992) 198

- [148] M. Dambekalne, M. Antonova, M. Livinsh, B. Garbarz-Glos, W. Smiga, A. Sternberg, PLZT - Synthesis, sintering and ceramics microstructure, *J. Europ. Cer. Soc.* **26** (2006) 2963
- [149] Q. Gan, R.A. Rao, C.B. Eom, J.L. Garrett, M. Lee, Direct measurement of strain effects on magnetic and electrical properties of epitaxial SrRuO₃ thin films, *Appl. Phys. Lett.* **72** (1998) 978
- [150] C. B. Eom, R. B. Van Dover, Julia M. Phillips, D. J. Werder, J. H. Marshall, C. H. Chen, R. J. Cava, and R. M. Fleming, D. K. Fork, Fabrication and properties of epitaxial ferroelectric heterostructures with (SrRuO₃) isotropic metallic oxide electrodes, *Appl. Phys. Lett.* **63** (1993) 2570
- [151] Q. X. Jia, X.D. Wu, S.R. Foltyn, P. Tiwari, Structural and electrical properties of Ba_{0.5}Sr_{0.5}TiO₃ thin films with conductive SrRuO₃ bottom electrodes, *Appl. Phys. Lett.* **66** (1995) 2197
- [152] A. Namiki, T. Kawai, K. Ichige, Angle-resolved time-of-flight spectra of neutral particles desorbed from laser irradiated CdS, *Surf. Sci.* **166** (1986) 129
- [153] R. K. Singh and D. Kumar, Pulsed laser deposition and characteriza, *SPIE* **2045** (1987) 10
- [154] M. Hanabusa, *Mater. Res. Soc. Symp. Proc.* **285** (1993) 447
- [155] T. J. Goodwin, V. J. Leppert, S. H. Risbud, I. M. Kennedy, and H. W. H. Lee, Synthesis of gallium nitride quantum dots through reactive laser ablation, *Appl. Phys. Lett.* **70** (1997) 3122
- [156] S. Metev, K. Meteva, Nucleation and growth of laser-plasma deposited thin films, *Appl. Surf. Sci.* **43** (1989) 402
- [157] Q. Zhang, S. Corcovic, C. P. Shaw, Z. Huang, R. W. Whatmore, Effect of porosity on the ferroelectric properties of sol-gel prepared lead zirconate titanate thin films, *Thin Solid Films* **488** (2005) 258
- [158] L.L.Hench, J.K.West, The Sol-Gel Process, *Chem. Rev.* **90** (1990) 33
- [159] Yu. I. Yuzyuk, P. Simon¹, E. Gagarina et.c., Modulated phases in NaNbO₃: Raman scattering, synchrotron x-ray diffraction, and dielectric investigations, *J. Phys.: Condens. Matter* **17** (2005) 4977
- [160] E. Bouziane, M. D. Fontana and M. Ayadi, Study of the low-frequency Raman scattering in NaNbO₃ crystal, *J. Phys.: Condens. Matter* **15** (2003) 1387
- [161] E. D. Palik, *Handbook of optical constants of solids* (Academic press 1985).
- [162] J. Petzelt, T Ostapchuk, I Gregora, P Kuzel, J Liu and Z Shen, Infrared and Raman studies of the dead grain-boundary layers in SrTiO₃ fine-grain ceramics, *J. Phys.: Condens. Matter*, **19** (2007) 196222
- [163] T. Chraska, A. H. King, C. C. Berndt, On the size-dependent phase transformation in nanoparticulate zirconia, *Mater. Sci. Eng. A* **286** (2000) 169
- [164] M. Ya. Gamarnik, Tensile and Compressive Effect of Intracrystalline Pressure in Small Particles, *Phys. Stat. Sol. B* **164** (1991) 107
- [165] Bergman, D.J., and Stroud D., Physical properties of macroscopically inhomogeneous media. In *Sol. State Phys.* 46 (eds. H. Ehrenreich and D. Turnbull) Academic Press, Boston (1992)
- [166] Bruggeman, D.A.G., *Ann. Phys.* **24** (1935) 636
- [167] M. V. Raymond, D. M. Smyth, Defects and charge transport in perovskite ferroelectrics, *J. Phys. and Chem. Sol.* **57** (1996) 1507
- [168] A.M. Bratkovsky and A.P. Levanyuk, Abrupt appearance of the domain pattern and fatigue of thin ferroelectric films, cond-mat/ 9908181v3 (2000) 1
- [169] L. Tichy, H. Ticha, The temperature dependence of the optical gap of glassy GeSe₂, *Mater. Lett.* **15** (1992) 198

- [170] D. Fong, G. B. Stephenson, S. K. Streifer, J. A. Eastman, O. Auciello, P. H. Fuos, and C. Thompson, Ferroelectricity in ultrathin perovskite films, *Science* **304** (2004) 1650
- [171] T. Tybel, C. H. Ahn, and J.-M. Triscone, Ferroelectricity in thin perovskite films, *Appl. Phys. Lett.* **75** (1999) 856
- [172] J. F. M. Cillessen, M. W. J. Prins, and R. M. Wolf, Thickness dependence of the switching voltage in all-oxide ferroelectric thinfilm capacitors prepared by pulsed laser deposition, *J. Appl. Phys.* **81** (1997) 2777
- [173] C. Lichtensteiger, J.-M. Triscone, J. Junquera, and P. Ghosez, Ferroelectricity and tetragonality in ultrathin PbTiO_3 films, *Phys. Rev. Lett.* **94** (2005) 047603
- [174] J. Junquera and Ph. Ghosez, Critical thickness for ferroelectricity in perovskite ultrathin films, *Nature* **422** (2003) 506
- [175] V. Nagarajan, I. G. Jenkins, S. P. Alpay, H. Li, S. Aggarwal, L. Salamanca-Riba, A. L. Roytburd, and R. Ramesh, Thickness dependence of structural and electrical properties in epitaxial lead zirconate titanate films, *J. Appl. Phys.* **86** (1999) 595; V. Nagarajan, C. S. Ganpule, B. Nagaraj, S. Aggarwal, S. P. Alpay, A. L. Roytburd, E. D. Williams, and R. Ramesh, Effect of mechanical constraint on the dielectric and piezoelectric behavior of epitaxial $\text{Pb}(\text{Mg}_{1/3}\text{Nb}_{2/3})\text{O}_3(90\%)-\text{PbTiO}_3(10\%)$ relaxor thin films, *Appl. Phys. Lett.* **75** (1999) 4183
- [176] Yang, Jing, and Luo, Jianbin, Processing and thickness effects on the microstructure and electrical properties of sol-gel deposited $\text{Pb}(\text{Zr,Ti})\text{O}_3$ films, *Sensors and Actuators A* **121** (2005) 103
- [177] K. R. Udayakumar, P. J. Schuele, J. Chen, S. B. Krupanidhi, and L. E. Cross, Thickness-dependent electrical characteristics of lead zirconate titanate thin films, *J. Appl. Phys.* **77** (1995) 3981
- [178] M.-C. Kim, J.-W. Choi, S.-J. Yoon, K. H. Yoon, and H.-J. Kim, Thickness dependence of $\text{Pb}(\text{Zr}_{0.52}\text{Ti}_{0.48})\text{O}_3$ films prepared by pulsed laser deposition, *Jpn. J. Appl. Phys. Part 1* **41** (2002) 3817
- [179] T. K. Kundu and J. Y. Lee, Thickness-dependent electrical properties of $\text{Pb}(\text{Zr,Ti})\text{O}_3$ thin film capacitors for memory device applications, *J. Electrochem. Soc.* **147** (2000) 326
- [180] D. M. Kim, C. B. Eom, V. Nagarajan, J. Ouyang, R. Ramesh, V. Vaithyanathan, and D. G. Schlom, Thickness dependence of structural and piezoelectric properties of epitaxial $\text{Pb}(\text{Zr}_{0.52}\text{Ti}_{0.48})\text{O}_3$ films on Si and SrTiO_3 substrates, *Appl. Phys. Lett.* **88** (2006) 142904
- [181] Y. C. Zhou, Z. Y. Yang, and X. J. Zheng, Residual stress in PZT films prepared by pulsed laser deposition, *Surface and Coatings Technol.* **162** (2003) 202
- [182] S. Yokoyama, Y. Honda, H. Morioka, S. Okamoto, H. Funakubo, T. Iijima, H. Matsuda, K. Saito, T. Yamamoto, H. Okino, O. Sakata, and S. Kimura, Dependence of electrical properties of epitaxial $\text{Pb}(\text{Zr,Ti})\text{O}_3$ thick films on crystal orientation and $\text{Zr}/(\text{Zr}+\text{Ti})$ ratio, *J. Appl. Phys.* **98** (2005) 094106
- [183] F. Yan, P. Bao, H. L.W. Chan, C. L. Choy, and Y. Wang, The grain size effect of $\text{Pb}(\text{Zr}_{0.3}\text{Ti}_{0.7})\text{O}_3$ thin films, *Thin Solid Films* **406** (2002) 282
- [184] K. Yang, W. S. Kim, and H. H. Park, Effect of grain size of $\text{Pb}(\text{Zr}_{0.4}\text{Ti}_{0.6})\text{O}_3$ sol-gel derived thin films on the ferroelectric properties, *Appl. Surf. Films* **169** (2001) 544
- [185] J.-H. Li, L. Chen, V. Nagarajan, R. Ramesh, and A. L. Roytburd, Finite element modeling of piezoresponse in nanostructured ferroelectric films, *Appl. Phys. Lett.* **84** (2004) 2626

- [186] I. Stolichnov, in *Nanoscale Phenomena in Ferroelectric Thin Films*, edited by Seungbum Hong, Ch. II., Springer, New York (2004)